NORTHWESTERN UNIVERSITY

Electron Microscopy Studies of Real and Model Oxide Supported Au Catalysts

A DISSERTATION

SUBMITTED TO THE GRADUATE SCHOOL

IN PARTIAL FULFILLMENT OF THE REQUIREMENTS

for the degree

DOCTOR OF PHILOSOPHY

Field of Materials Science and Engineering

By

Yingmin Wang

EVANSTON, ILLINOIS

June 2006

© Copyright by Yingmin Wang 2006

All Rights Reserved

ABSTRACT

Electron Microscopy Studies of Real and Model Oxide Supported Au Catalysts

Yingmin Wang

Oxide supported Au catalysts have been the center of intensive research since being discovered as the most active catalysts for low temperature CO oxidation. However, the origin of the high activity of these catalysts remains unknown. The complexity of this catalytic system prevents a clear identification and characterization of the factors truly affecting its properties. In this thesis research, the attention was focused on certain areas that are truly crucial for the understanding of the Au catalysts, including the preparation and activation of Au catalysts, the properties of the TiO_2 surface and the interaction between TiO_2 and gold nanoparticles. Electron microscopy was used throughout this research along with other techniques and has been proved to be a powerful and irreplaceable tool and provide an insight into this catalytic system with a unique angle.

Among all of the findings of this research, the examination of Au catalysts identified the role of chlorine in accelerating the agglomeration of gold particles and poisoning the active sites. Studies on the activation of Au/Al_2O_3 and Au/TiO_2 catalysts demonstrated the oxidation state and the size of the gold particles were two competing factors during

activation and both were very important. The difference in the mobility of gold species on oxide surfaces affects them.

The study of the TiO_2 surface described the reoxidation process of the TiO_2 surface and a new surface reconstruction, c(2x2), on this surface was reported. Its atomic structure was solved by applying Direct Methods and Density Functional Theory calculations.

The study of Au/TiO_2 model catalysts revealed no preferred orientation between gold nanoparticles and TiO_2 supports with various crystallographic orientations and surface conditions, and this fact was explained by the influence of surface adsorbates. Model catalyst studies also characterized surface induced sintering, and estimated the temperature of local heating during surface induced sintering. Finally, the attempt to measure the catalytic properties of the Au model catalyst was presented and the initial results was described.

Approved by

Professor Laurence D. Marks

Department of Materials Science and Engineering

Northwestern University, Evanston, IL 60201, USA

Acknowledgements

I would like to thank my advisers, Professor Laurence D. Marks, for his guidance and patience, and for giving me the opportunity to work with him, and Professor Harold H. Kung, for his enthusiasm and encouragement, and for showing me the way of doing science. Without their support, I could not possibly finish this Ph.D. study.

I would like to thank the members of the Marks group - Arun, Edy, Chris, Ann, Courtney, Arno, Brian, Jim and Robin, for being my coworkers and my fiends during my five years of wonderful life at Northwestern.

I would also like to thank Professor Mayfair Kung and the members of the Kung group - Colline, Jeff and Juan, for all the help and input during my research. Their wonderful work on catalysis is the corner stone of this study.

I would like to formally credit the following contributions to this work: The refining part of Direct Methods in Chapter 4 was carried out by Dr. A.K. Subramanian. The DFT calculations in Chapter 3 were performed by Dr. O. Warschkow, Prof. L.D. Marks and Prof. M. Asta. The catalytic property data in Chapter 3 were provided by Dr. C.K. Costello and J.H. Yang. The atomic resolution STEM images in Chapter 3 were taken by Dr. A. Lupin at ORNL. I am also truly indebted to J. D. Henao for carrying out FTIR and MassSpec study on the model catalysts.

And finally, I would like to thank my family - my parents, for their guidance; my wife, for her patience and support during those long thesis writing nights; and my unborn

daughter, for motivating me to complete this thesis.

Table of Contents

ABSTRACT 3

Acknowledgements 5

List of Tables 10

List of Figures 11

Chapter 1. Introduction 18

1.1. Heterogeneous Catalysis and Model Catalysts 18

1.2. Au Catalysis 21

1.3. Factors Affecting Catalytic Activity 23

1.4. Objective 26

Chapter 2. Experimental Techniques 28

2.1. Transmission Electron Microscopes 31

2.2. TEM Sample Preparation 32

2.3. Data Acquisition and Processing 34

2.4. Direct Methods 38

2.5. Other Experimental Techniques 40

Chapter 3. Studies on Oxide Supported Au Catalysts 43

3.1. Catalysts Preparation And Catalytic Properties 43

3.2. Effects of Chlorine on Supported Au Catalysts 45

3.3. Activation of Au/γ-Al_2O_3 Catalysts for CO Oxidation 57

3.4. Activation of Au/TiO_2 Catalysts for CO Oxidation 66

3.5. Conclusions 71

Chapter 4. Studies on TiO_2 (100) surface 75

4.1. Introduction 75

4.2. Sample Preparation and Characterization 78

4.3. Surface Morphology 80

4.4. C(2x2) Surface Reconstruction 93

Chapter 5. Studies on Au/TiO_2 Model Catalysts 104

5.1. Sample preparation 104

5.2. Growing of Au on TiO_2 surface 105

5.3. Sintering of Au on TiO_2 (100) surface 114

5.4. Catalysis of Au on TiO_2 surface 119

Chapter 6. Conclusions and Future Work 123

6.1. Conclusions 123

6.2. Future work 125

References 127

Appendix A. Calculation of the TiO_2 Phase Diagram 141

A.1. Introduction 141

A.2. Thermodynamic Models for the Calculation 142

A.3. Results and discussion 148

A.4. Conclusion 149

List of Tables

3.1	Physical characteristics and SCO activities of Au/Al_2O_3	56
3.2	Activation of Au/Al_2O_3 for CO oxidation	59
4.1	Parameters used in annealing experiments	79
5.1	Parameters used in reaction induced sintering experiments	116
A.1	Thermodynamic properties of the system Ti-O I	150
A.2	Thermodynamic properties of the system Ti-O II	151

List of Figures

2.1 Applications of transmission electron microscopy (TEM): (a) High resolution TEM (HRTEM) image of polycrystalline TiC film on single crystal Si substrate (b) Scanning TEM (STEM) images of mineral Hematite with TiO_2 precipitates, (c) HRTEM image of CeO+CuO catalyst, (d) STEM image and EDS analysis of tungsten sustained siloxane nano-network 30

2.2 Picture of Hitachi UHV 9000 microscope with attached UHV sample preparation and characterization system (SPEAR) 33

2.3 Two adjacent gold particles in gold catalysts coalesce under the electron beam of TEM, several seconds between each frame was taken 38

3.1 TEM images of catalysts prepared with $HAuCl_4$, with the addition of Mg citrate (a) before calcination, (b) after calcination, (c) with no Mg citrate addition. 48

3.2 Size distribution of Au particles on Au/Al_2O_3 catalysts prepared with $HAuCl_4$, with the addition of Mg citrate (a) before calcination, (b) after calcination, (c) with no Mg citrate addition. 49

3.3 TEM images of Au/Al_2O_3 prepared from Au acetate precursor: (a) as calcined; (b) additional 4 hours calcinations at 350℃; (c1) and (c2)

catalyst with 0.3 wt.% Cl added (Cl/Au=0.15) and then calcined at 350℃ for 4 hours. 51

3.4 Size distribution of Au particles on Au/Al_2O_3 prepared from Au acetate precursor: (a) as calcined; (b) additional 4 hours calcinations at 350℃; (c) catalyst a with 0.3wt% Cl added (Cl/Au=0.15) and then calcined at 350℃ for 4 hours. 52

3.5 TEM images of Au/Al_2O_3 prepared by hydrolyzing $HAuCl_4$ at pH7 and 70℃: (a) as calcined; (b) catalyst with 0.3 wt% Cl added (Cl/Au=0.15) and then heated at 100℃ for 1 hour; (c) catalyst with 0.3 wt% Cl added (Cl/Au=0.15) and then heated at 350 ℃ for 4 hours. 53

3.6 Size distribution of Au particles on Au/Al_2O_3 prepared from $HAuCl_4$ at pH7 and 70℃: (a) as calcined; (b)catalyst with 0.3 wt% Cl added (Cl/Au=0.15) and then heated at 100℃ for 1 hour; (c) catalyst with 0.3 wt% Cl added (Cl/Au=0.15) and then heated at 350 ℃ for 4 hours. 54

3.7 TEM images of Au/Al_2O_3 after various treatments: (a) uncalcined (as prepared); (b) calcined at 350℃ for 4 hours; (c) activated by H_2+H_2O at 100℃ for 1 hour; (d) deactivated by He at 100℃ for 1 hour, (e) regenerated by H_2O at room temperature for 30 minutes. 61

3.8 Au/Al_2O_3 catalyst after H_2 30min, then H_2+H_2O 30min at 100℃ activation: (a) isolated gold atoms; (b) gold clusters. 62

3.9 AXANES spectra of Au coumpounds : (a) Au^{3+} acetate, (b) as-prepared Au/γ-Al2O3 catalyst, (c) Au^{+}Cl, (d) Au foil. 64

3.10 XANES characterizing 1.3wt% Au/γ-Al_2O_3(DP): (a) as prepared uncalcined, (b) after 30 min in H_2 at 100℃, (c) after subsequent treatment in H_2O and H_2 at 100℃ for 30 min, (d) after an additional 30 min in H_2 and H_2O at 100℃. (e) another sample after treatment in H_2O and H_2 at 100℃ for 2 h. 64

3.11 TEM images of Au/TiO_2 after various treatments: (a) uncalcined (as prepared); (b) reduced by H_2 at room temperature; (c) calcined in air at 350℃ for 4 hours. 67

3.12 TiO_2 catalyst after CO activation at room temperature: (a) gold atom clusters; (b) well faceted gold nanoparticles. 69

3.13 Magnitude of the Fourier transformed $k^2$2-χfunction in R-space of Au/TiO_2 after selected H_2 pulse. The arrows indicate positions of Au-O and Au-Au scattering at 1.6 and 2.3 Å in R space. 69

3.14 Au (4f) binding energy of Au/TiO_2 catalyst: (a) as-prepared sample; (b) sample fully reduced by H_2 pulses; (c) sample 50% reduced by H_2 pulses; and (d) reference Au/TiO_2 catalyst (calcined) distributed by WGC. 70

3.15 Activity and gold particle size change with time on stream. Temperature: -68℃; reaction gases: CO 1%, O_2: 2.5%, balanced by He at 1atm; ananlyzed and graphed by J.H. Yang 72

3.16 Activity and gold particle size change with time on stream. Temperature: -68℃; reaction gases: CO 1%, O_2: 2.5%, balanced by He at 1atm; ananlyzed and graphed by J.H. Yang 72

4.1 Ball and stick model of rutile TiO_2 (100) surface. Ti: filled sphere O: open sphere 77

4.2 XPS spectrum of TiO_2 (100) TEM sample after anneals 79

4.3 XPS spectrum of TiO_2 (100) TEM sample before and after ion-milling: (a) Ti $3p_{3/2}$ peak; (b) LMV Auger peak 81

4.4 Rutile TiO_2 (100) surface evolution with temperature. After ion milling sample, bright field image with DP. 82

4.5 Rutile TiO_2 (100) surface evolution with temperature. 750℃ 1 hour in O_2, dark field image with DP. 83

4.6 Rutile TiO_2 (100) surface evolution with temperature. 800℃ 1 hour in O_2, dark field image with DP. 84

4.7 Rutile TiO_2 (100) surface evolution with temperature. 900℃ 1 hour in O_2, dark field image with DP. 85

4.8 Effects of time and annealing environment on rutile TiO_2 (100) surface. 750℃ 2 hours in O_2, dark field image with DP. 87

4.9 Effects of time and annealing environment on rutile TiO_2 (100) surface. 830℃ 6 hours in O_2, bright field image with DP. 88

4.10 Effects of time and annealing environment on rutile TiO_2 (100) surface. 800℃ 1 hour in Ar, dark filed image with DP 89

4.11 "Healing effects" of O_2 on rutile TiO_2 (100) surface: (a) 800℃ 1 hour in O_2; (b) 830℃ 6 hours in O_2 image. 91

4.12 Magnelli phases formed on TiO_2 surface after annealed in either O_2 or Ar: (a) High resolution TEM of Magnelli phases; (b) Electron diffraction pattern for Magnelli phase. 96

4.13 Direct Method scattering map for TiO_2 c(2x2) surface. Inset: atoms arrangements obtained directly from the map. Filled sphere Ti; open sphere O 98

4.14 Top and side view of TiO_2 (100) surface: (a) (1x1) stoichiometric surface; (b) (2x2) stoichiometric surface; (c) (2x2) vacancy surface. Surface Titanium atoms are red, bulk Titanium atoms are yellow, Oxygen atoms are blue 99

4.15 DFT calculation of c(2x2) energy on reduced TiO_2 with calculated phase diagram for the Ti-O system in the composition range between Ti_4O_7 and rutile: Magnelli phase is shown as equilibrium line between adjacent phases; c(2x2) is calculated by using Ti_4O_7 as reference 102

5.1 TEM images of Au/TiO_2 model catalyst sample prepared by deposition-precipitation: (a) low loading of gold on the surface; (b) gold particles with abnormally large size. 107

5.2 Au/TiO_2 model catalyst sample prepared by PVD: (a) TEM image at lower magnification; (b) High resolution TEM image. 108

5.3 TEM images of Au/TiO_2 model catalyst sample prepared by PVD with: (a) 10 times more than desired deposition ; (b) 50 times more than desired deposition. 110

5.4 Diffraction pattern of Au/TiO_2 model catalyst sample prepared by PVD: (a) on Magnelli surface; (b) on c(2x2) surface. 110

5.5 TiO_2 (110) TEM sample after annealing in oxygen at 900℃ for 1 hour (a) TEM image; (b) (1x1) diffraction pattern. 112

5.6 Au/TiO_2 system (a) TEM image of Au/TiO_2 (110); (b) STEM image of Au/TiO_2 (110); (c) TEM image of Au/TiO_2 (001); (d) STEM image of Au/TiO_2 (001). 113

5.7 STEM Z-contrast image of Au/TiO_2 model catalyst sample: (a) as prepared; (b) annealed in air for 1 hour at 100℃; (c) annealed in air for 1 hour at 200℃; (d) annealed in air for 1 hour at 300℃. 117

5.8 STEM Z-contrast image of Au/TiO_2 model catalyst sample after 1 hour CO oxidation reaction gas treatment at room temperature: (a) at high magnification; (b) at low magnification. 118

5.9 Size distribution of gold particles for as prepared sample, sample annealed in air for 1 hour at 100℃ and sample treated by reaction gas for 1 hour at room temperature, respectively. 118

5.10 Size distribution of gold particles for samples annealed in air for 1 hour at 200℃ and 300℃ respectively. 119

5.11 FTIR experiment on the activity of Au/TiO_2 model catalyst: the changes of CO and CO_2 concentration in the trapped reaction gas 122

A.1 Calculated phase diagram for the Ti-O system in the composition range between Ti_4O_7 and rutile 149

A.2 Comparison between equilibrium between Ti_4O_7 and Ti_5O_9 calculated and that from the paper and experimental data 152

CHAPTER 1

Introduction

1.1. Heterogeneous Catalysis and Model Catalysts

The concept of catalysis was introduced in 1835 by Berzelius. Nowadays catalysis, particularly heterogeneous catalysis, has become a crucial part of many industrial activities, including oil refining, organic synthesis, pollution control and many other fields. Modern catalysts are generally composed of several elements in precise proportions. They are optimized in order to give the highest reaction rate and also, equally important, to have the best selectivity. After decades of research, systematic information on the catalytic properties of many catalysts has been established and accumulated. However, further optimization is mainly based on the empirical method of trial and error. Even if the general features of a heterogeneous catalysis are known, it is usually impossible to describe the details of the reaction mechanisms taking place during a practical catalytic reaction. This is partly due to the complexity of the catalysts and also due to their lack of characterization. For example, many real catalysts are composed of small (in the nanometer range) metal particles dispersed on a porous material. The uncertainty and nonuniformity of the materials involved, preparation methods, surface conditions, particle-support interaction and more make real catalysts intrinsically difficult to characterize. Even electron microscopy, one of the best techniques for catalysis study, has its limitations on these samples. Information on size distribution, particle morphology, surface and interface

structure is manageable to obtain, but relating this information to catalytic properties with confidence is still a challenge. In order to overcome this difficulty, basic studies in heterogeneous catalysis are undertaken on model catalysts.

Model catalysts were introduced in the late 1960s with the development of UHV technology. They were basically well-ordered extended surfaces of catalytic metals prepared under UHV conditions. These surfaces are relatively simple and remain clean in a UHV environment, and furthermore, they can be fully characterized by the numerous surface science techniques available. Since the introduction of model catalysts, the atomic structure and electronic properties of many metal surfaces have been studied (Somorjai 1994). Their chemical properties were investigated for the first time by studying the chemisorption properties of these surfaces (Somorjai 1994). As a result, the mechanism of some catalytic reactions has been elucidated from UHV experiments, including the oxidation of CO (T. Engel 1978) and the synthesis of ammonia (Ertl 1983) and methanol (Askgaard et al. 1995).

Now, the remaining question is: does the mechanisms in UHV conditions extend to practical catalysis conditions? Indeed most catalytic reactions are operated at atmospheric or even higher pressure. This "pressure gap" is overcome by using high pressure cells, where model catalytic reactions take place at high pressure, and a coupled UHV chamber is used for characterization of the catalyst before and after the reaction (Rodriguez and Goodman 1995). One can argue that the surface structure of the catalyst can be modified during the reaction itself. To invalidate this argument, the atomic structure of a model catalyst has been investigated during a reaction by infrared spectroscopy (Vesecky et al. 1995). Scanning tunneling microscopy (STM) is also a very promising tool,

permitting one to follow a catalytic reaction, *in situ*, on the atomic scale at low pressure (Crew and Madix 1994) and possibly at atmospheric pressure (Schfoder et al. 1995).

However, metal single crystals cannot account for two important characteristics of practical catalysts, namely the finite size of the metal particles and the presence of the support material. It is well documented that both the reactivity and the selectivity of a catalyst can depend on the particle size (Che and Bennett 1989). Additionally, the catalyst support is not necessarily a simple mechanical support for the metal particles since the support can modify the electronic properties (therefore the reactivity) of the particles (Kao et al. 1980; Ogawa and Ichikawa 1995; Pacchioni and Rrsch 1994). In some cases, the support material can even migrate over the particles, as in the case of the strong metal support interaction (SMSI) (R. Persaud 1997). These new limitations, sometimes named the "material gap" (Goodman 1995a), have been recently overcome by the introduction of a new type of model catalyst: the supported model catalyst. The supported model catalyst is composed of small metal particles supported on planar surfaces. The planar support surfaces allow for a precise characterization similar to the case of extended metal surfaces. Furthermore, the small metal particles are prepared on the support either by physical deposition in UHV, or by chemical deposition, mimicking the preparation of industrial catalysts, as in the case of decomposition of metal-organic precursors (Purnell et al. 1994) or wet impregnation (Valden et al. 1994). The similarities in preparation allow for more information to be gained about real catalysts by characterizing the nucleation and growth of metal clusters on the model support (Poppa 1993; Lad 1995; Campbell 1997). At the same time, related deposition methods and characterization techniques in a non-UHV preparation environment are also well developed (Gunter et al. 1997; Raupp

et al. 1986). Although the surface science approach to supported model catalysts is still in its infancy, it is a rapidly growing field. Moreover, the introduction of new techniques with atomic spatial resolution opens the way to a real time atomic scale investigation of supported model catalysts closely related to real catalysts.

1.2. Au Catalysis

Gold has long been known to be far more inert than other transition metals. Consequently, its catalytic properties have remained unexplored. Little research has been done to study the chemisorption of reactant gases on bulk gold surfaces. Of the studies done, it has been shown that bulk gold adsorbs CO at temperatures below -123℃ or at ambient temperatures if the CO partial pressure is sufficiently high. The adsorption properties of certain crystallographic surfaces of gold, including Au(110) (Yates 1969) and Au(332) (Ruggiero and Hollins 1996) have also been investigated. In particular, the work on the Au(332) surface (Ruggiero and Hollins 1996) nicely demonstrates the importance of low coordination number (CN) atoms in enabling the chemisorption of carbon monoxide on gold, since it has steps on terraces of the (111) structure. As to its activity, bulk gold is not a good catalytic candidate since the oxidation of CO can occur only when oxygen is provided in dissociated form. Only at temperatures less than 400℃ can the completed d shell of gold allow for a weak coupling with adsorbed species, thus creating a high energy barrier for dissociative adsorption (Schubert et al. 2001) and a slow reaction rate.

In the 1970's, Bond and Sermon found that, when dispersed as small, nanosize particles on a SiO_2 or Al_2O_3 support, Au could catalyze the hydrogenation of linear alkenes at moderate temperatures (Bond et al. 1973; Sermon et al. 1979). Also in the 1970's

Parravano and coworkers prepared Au nanoparticles dispersed on MgO and Al_2O_3 that were active for oxygen and hydrogen transfer reactions (Cha and Parravano 1979; Galvano and Parravano 1978). Ozin and et al. also discovered that single Au atoms, when co-condensed with an equilmolar mixture of CO and O_2 at 10K, could liberate CO_2 when the temperature was increased to 30-40K (Huber et al. 1977).

However, because the catalytic activity of early supported Au catalysts was inferior to other noble metals for hydrogenation and oxidation reactions, Au was never at the forefront of catalytic research. It was only when Haruta demonstrated that metal oxide supported nanoparticles gold are in fact the most active catalyst for low temperature CO oxidation, and that the reaction can be carried out at temperatures as low as -70℃ (Haruta et al. 1987), that interest was rekindled. Since then, unusual activity and selectivity of supported gold nanoparticle catalysts for various reactions have been reported, including the water gas shift reaction (Sakurai et al. 1997), methanol synthesis from CO_2 (Sakurai and Haruta 1996), NO reduction by H_2, CO, or propene (Kung et al. 1996), and propene epoxidation (Hayashi et al. 1998). But, despite the efforts of many research groups, the origin of the remarkable catalytic properties of supported gold catalysts remains unknown.

The majority of published work in this field focuses on elucidating the nature of the active sites and reaction mechanism for low temperature CO oxidation. Few definitive answers have emerged, and much confusion remains regarding the properties of the catalytic active sites for this oxidation reaction. A greater understanding of the nature of the active sites, as well as the corresponding reaction mechanism, will provide s means to design more active or selective catalysts and regulate the entire surface reaction at the catalyst surface.

Research at Northwestern University has focused on various types of oxide supported Au catalysts for the oxidation of CO, including Au/Zeolite, Au/TiO_2 and Au/Al_2O_3. The effects of preparation methods on catalytic properties, the role of certain key treatments, in particular H_2O, in the activation and regeneration process, and the changes in chemical states and structure of nanosize gold particles during reaction have been thoroughly investigated. Consequently, an active site consisting of a ensemble of metallic Au atoms and Au^+-OH^-, along with a CO oxidation reaction mechanism involving the formation and decomposition of a bicarbonate intermediate, has been proposed (Costello et al. 2002, 2003, 2004; Yang et al. 2005; Kung et al. 2003).

1.3. Factors Affecting Catalytic Activity

It is helpful to have a picture of what really happens during gold catalysis at the atomic level. In particular, an understanding of the status of the supported gold nanoparticles and the condition of the support surface needs to be established, because it is these fine details, such as the structure, epitaxy and morphology of gold nanoparticles under various preparation conditions and treatments, that decide the mechanism of the reaction.

The dependence of catalytic efficiency on the size of gold nanopartilces has attracted attention both in experiments and theoretical studies. The previous attempts to interpret experimental observations for other generally active metals of Groups 8-10 have been clouded by factors including the difficulty of preparing mono-dispersed particles and isolating the influence of adsorbates and the support. These factors apply to gold also, and this is one of the reasons why various theories have been proposed, including electronic effects (Valden et al. 1998) and the increase in step and edge sites with decreasing particle

size (Mavrikakis et al. 2000; Gupta and Tripathi 2001), etc.. Sometimes, however, these theories contradict each other. All we know for sure is that as long as the rate is not limited by mass-transport, the reaction rate per unit area of gold surface is dependent on particle size. Although there is no apparent optimal particle size for the reaction, it can be concluded that gold in nanoparticle form is one necessary requirement for activity.

Various gold crystallographic surfaces, steps and edges have different properties for chemsorption of reaction gases (Yates 1969; Ruggiero and Hollins 1996; Mills et al. 2003; Hagen et al. 2002). The structure and morphology of gold nanoparticles therefore control the chemical properties of the nanoparticle. Gold nanoparticles can form various types of FCC structured particles with different symmetries or even multiple twinned particles (MPTs). Some of the particles share similar stabilities, and rapid fluctuation between different structures can be observed directly by TEM (Marks et al. 1988, 1986). The interaction between gold nanoparticles and oxide supports sometimes forces certain epitaxial relationships or dampens the fluctuation between different forms of particles (Smith and Marks 1985). Furthermore, as the facets of a small gold particle are different with respect to structure and energy, its equilibrium shape can be changed in the presence of an adsorbate (Shi 1987), since the energy of a surface changes upon foreign molecules adsorption and this effect of adsorbates introduces more complexity to understanding the morphology and structure of nanoparticls, especially nanoparticles prepared by wet chemistry method.

Clearly, the catalytic activity of gold nanoparticles depends on the metal oxide support, since unsupported gold nanoparticles are not as active as supported ones (Iizuka

et al. 1999). However, the degree of this effect is much less certain. Many studies reporting that the activity does depend on the choice of support, suggest that gold supported on insulating , covalently bonded metal oxides like Al_2O_3 and SiO_2 are much less active than those supported on TiO_2, Fe_2O_3, Co_3O_4 and NiO (Schubert et al. 2001). However, other results (Okumura et al. 1998) showed that Au/TiO_2, Au/Al_2O_3 and Au/SiO_2 catalysts prepared by chemical vapor deposition (CVD) exhibit essentially the same catalytic activity. The contradictory results imply that it is not the support itself that is important, but rather it is the creation of a strong interaction at the gold-support interface, dependent on the method of preparation, that is critical.

The roles the oxide supports play can be divided into two categories. Firstly, as proposed by many groups (Schubert et al. 2001; Liu et al. 1999), the oxide support provides the activated oxygen species for the CO oxidation reaction. Unsupported Au is incapable of activating O_2. Although some experimental research groups (Valden et al. 1998) and density functional theory (DFT) calculations (Mavrikakis et al. 2000) proposed the direct adsorption of oxygen on gold, there is no direct experimental evidence that supported Au nanoparticles can dissociate O_2. It has been suggested that the O_2 adsorbs on the support at the support-particle interface in the form of a superoxide.

On the other hand, oxide supports provide a surface where gold particles nucleate, grow and propagate. Besides the atomic structure of the support, for an oxide with a large flat surface in UHV, surface defects, which are often oxygen vacancies (Moorhead and Poppa 1979), have the biggest influence on nucleation. Outside of UHV environment, oxide surfaces are contaminated by hydroxyls (Coluccia et al. 1979) and carbonates (Onishi et al. 1987) after being exposed to air, even for a short time. These contaminants act

as the nucleation centers for gold nanoparticles, in particular when wet chemistry is the method for sample preparation. After sample preparation, the interaction between the oxide support and gold nanoparticles reduces sintering, despite the fact that nanoparticles are unstable with respect to the bulk and there is a driving force for coalescence. It is during calcination or reaction that the elevated temperature increases the mobility of gold atoms, thereby introducing structure and morphology changes, further affecting the chemical properties of gold catalysts.

1.4. Objective

As illustrated in the above review of the literature, many unresolved issues remain in the field of gold catalysis. Although a fair number of studies have been done in attempt to understand the nature of the chemical reactions of real catalysts, the results from these studies vary from one to another, sometimes even contradicting each other. The large number of variables involved in each study might be the reason why not many definite conclusions have been made. On the other hand, model gold catalysts have been extensively investigated. But most of the systems are oversimplified compared to the real catalyst system. The existence of the so-called "pressure gap" and "material gap" between real and model catalysts makes these results informative but less relevant to real catalytic systems.

This presented work targets improving the understanding of the many factors affecting catalytic properties of oxide supported gold catalysts, in order to explain the existing observations and provide clear and relevant characterizations of this catalytic system. This objective was accomplished by studying the surface of oxide supports and oxide

supported Au catalytic systems, representing both real and model catalysts, using electron microscopy and other surface science techniques. In this study, the Au/TiO_2 system was chosen as the target of interest because it exhibits an excellent catalytic ability for CO oxidation at room temperature. This study has not attempted to be exhaustive, but rather had focused on some specific issues, which are crucial for the understanding this system: the structure and morphology of gold nanoparticles in real catalysts, the characterization of the TiO_2 surface, and the effects of the state of the support surface and subsequent treatments on gold nanoparticles.

The general experimental techniques, including a description of electron microscopy, sample preparation, procedures for data acquisition and processing, and a description of other experimental techniques employed in this study, are presented in Chapter 2. Chapter 3 describes a study of real catalysts using electron microscopy and other techniques. The surface evolution of the TiO_2 (100) surface during annealing is presented in Chapter 4. Chapter 4 describes the atomic structure of a surface reconstruction on the TiO_2 (100) surface and its implication. The characterization of the model catalyst on various TiO_2 surfaces is given in Chapter 5. Conclusions from this study and suggestions for future work are presented in Chapter 6.

CHAPTER 2

Experimental Techniques

As described in Chapter 1, an atomic level understanding of the structure and electronic properties is required in order to gain an accurate, fundamental view of Au catalysis. Ideally, these properties can be related to the observed catalytic properties (activity, selectivity and durability) in real catalyst. For this purpose, transmission electron microscopy (TEM) has been used as a major experimental tool in this study.

TEM studies the interaction between condensed materials and an accelerated electron beam, by analyzing after-interaction electron intensity and other signals generated during this process, to obtain crystallographic and chemical information about the sample under study.

The most common application of TEM is imaging. Compared to other microscopic techniques, TEM is able to form 2-D projection of 3-D structure over a wide scale range, from micrometer to sub-nanometer. Various techniques (including Bright Field (BF), Dark Field (DF) and High Resolution TEM (HRTEM) etc.) have been developed to obtain an informative image under different conditions.

Electron diffraction is another indispensable part of TEM, containing information on the crystal structure, lattice repeat distance, specimen shape and even crystallographic symmetry. At the same time, the diffraction pattern can always be related to the image of the area of the specimen from which it came. It is also possible to obtain diffraction

patterns for a large area (several μm^2) down to few nm^2, allowing the determination of the structure of a single metal particle when a field emission gun is used.

Electron radiation from TEM produces a wide range of secondary signals from the specimen, most of which are used in analytical electron microscopy, giving us chemical information and other details about the sample. For example, X-ray energy dispersive spectrometry (XEDS) and electron energy loss spectrometry (EELS) can be used to identify elemental changes associated with inhomogeneous micro-structures and the chemical state of certain elements. Figure 2.1 shows the applications of various TEM techniques employed in this study.

All of the above advantages of the TEM bring accompanying drawbacks. First of all, the price to pay for any high-resolution imaging technique is that only a small portion of specimen is examined at any time. It is especially important when studying the size distribution of nano-sized Au particles of Au catalysts. Large scale sampling is necessary in this case. Secondly, TEM requires the specimen to be thin enough for electron transmission and operation to be carried out under high vacuum conditions. These requirements limit the types of samples that can be studied by TEM and, under certain circumstances, exclude the possibilities of *in situ* experiments. Finally, as mentioned above, TEM presents 2-D images of 3-D specimens, which makes the acquired information difficult to interpret. Furthermore, the TEM information generally is averaged through the thickness of the specimen. In this study, no depth sensitivity means profile information, including the height and faceting, of nano-sized Au particles is not simple to obtain.

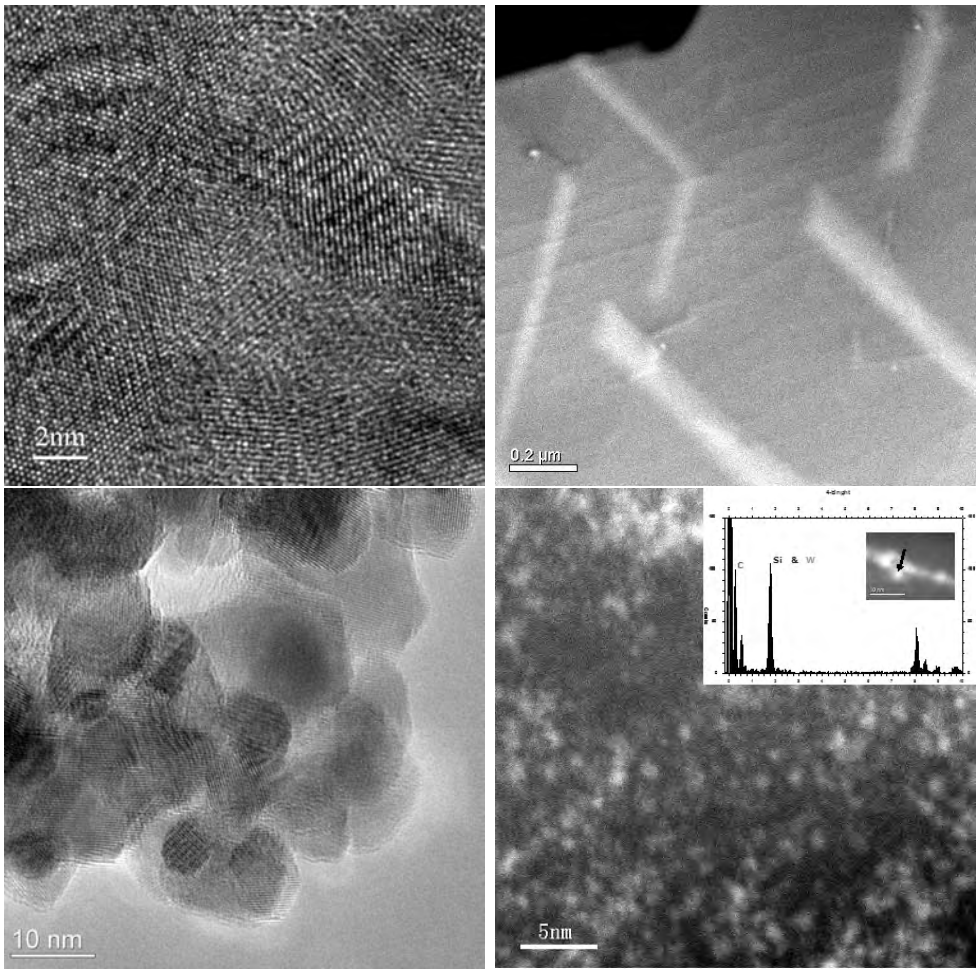

Figure 2.1. Applications of transmission electron microscopy (TEM): (a) High resolution TEM (HRTEM) image of polycrystalline TiC film on single crystal Si substrate (b) Scanning TEM (STEM) images of mineral Hematite with TiO_2 precipitates, (c) HRTEM image of CeO+CuO catalyst, (d) STEM image and EDS analysis of tungsten sustained siloxane nano-network

In this chapter, several issues related to the advantages and drawbacks of TEM will be discussed, including the selection of proper microscopes and techniques, sample preparation, data acquisition and processing. The last section is devoted to other complementary

experimental techniques used in this study in order to achieve full characterization of Au catalysts.

2.1. Transmission Electron Microscopes

Various types of microscopes were used in this study. The selection was dependent on the samples under study and each instrument's unique features.

The Hitachi 8100 (operated at 200kV with a W hairpin filament) was used to perform general examination of samples at low magnification, including bright field and dark field imaging and Selected Area Diffraction (SAD). Due to the microscope's low requirement for vacuum, samples can be exchanged within a much shorter time compared to other microscopes. Another advantage of using this microscope is that it has a large specimen tilt ($\pm 45°$) pole piece, which makes it possible to carry out crystallographic characterization.

The Hitachi HF2000 (operated at 200kV with a cold cathode Field Emission Gun (cFEG)) is a fully equipped atomic resolution analytical electron microscope, capable of Gatan Image Filtering (GIF), high resolution Electron Energy Loss Spectroscopy (EELS) and Energy Filtering TEM (EFTEM), so local chemical information about the specimen and high contrast/resolution images can be obtained. Its BF/ADF STEM detector with simultaneous Emispec PC acquisition system for STEM, EDS and EELS can be used for automated line scans, mapping and spatially resolved analytical studies with nanoscale resolution.

The UHV Hitachi 9000 (operated at 300kV with a LaB_6 filament) is another microscope used in this study. It was redesigned based upon the Hitachi H9000 to be fully UHV compatible and bakeable to 200℃ (Marks et al. 1988). In addition to standard

electron microscopy, the instrument is equipped with a Gatan Parallel Electron Energy Loss Spectrometer which can be used for elemental analysis and to determinie the sample thicknesses. A 1024×1024 slow-scan CCD camera was retrofitted to the microscope, thus enabling real time digital imaging. Most importantly, a UHV system called SPEAR (Fig 2.2)(Collazo-Davila et al. 1995), is attached to this microscope, which makes it possible to perform *in situ* sample preparation and characterization. Magnetron sputtering, PVD, SEM, Ion gun, E-gun, XPS and gas/heat treatment can be readily employed if necessary. This system has been used for studying a variety of materials (Grozea et al. 2000; Widjaja and Marks 2003; Bengu and Marks 2001; Erdman et al. 2002). In this study, parts of model catalyst sample preparation and HRTEM were done by using this microscope.

The JEOL JEM 2100F fast TEM (operated at 200kV with a high brightness Schottky emitter) is the center piece of STEM work in this study. As an Analytical Scanning Transmission Atomic Resolution (A STAR) electron microscope, it is equipped with STEM, GIF, EDS and a 2kx2k CCD camera. A probe size of less than 2Å can be formed in the STEM mode, which enables sub-nanometer imaging and chemical analysis.

A VG Microscopes HB603U STEM with a Nion aberration corrector in Oak Ridge National Lab (ORNL) was used as part of a collaboration. After aberration correction, a 0.6Å beam size was obtained to produce single Au Z-contrast images.

2.2. TEM Sample Preparation

A wide variety of specimens were studied using TEM. Besides real Au catalysts supported by different oxides (Al_2O_3, zeolite and rutile TiO_2), model catalysts with single

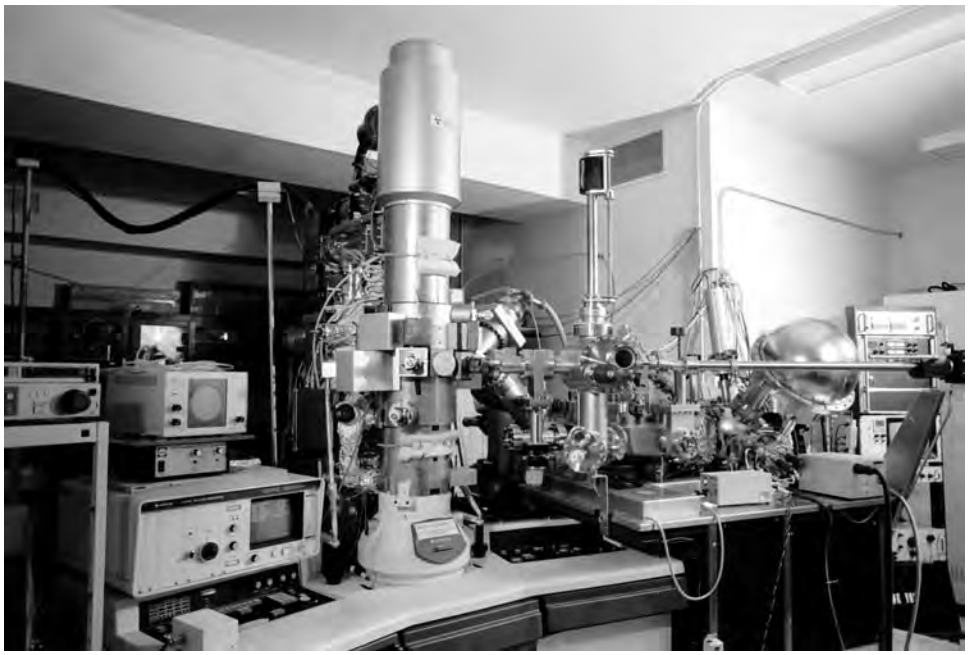

Figure 2.2. Picture of Hitachi UHV 9000 microscope with attached UHV sample preparation and characterization system (SPEAR)

crystal rutile TiO_2 supports were used. In order to meet the requirements necessary for TEM study, sometimes special treatments were needed.

Au catalyst specimens were prepared by a wet chemistry method (see Chapter 6). Nano-sized Au particles were deposited onto a powder oxide support in solution, and then were dried in a desiccator or calcined in a furnace. Since the size of powder oxides was less than 100nm, it was ready to be used in the TEM study without pulverization. The sample can be directly dispersed onto lacey carbon grid (Ted Pella) after grinding, but special attention needs to be paid to the water left in the as-prepared specimens and contamination introduced during preparation and treatment, as they might deteriorate the high vacuum and produce artifacts interfering with the interpretion of experimental results.

For the model catalyst study, the sample preparation process can be separated into two parts: first is making single crystal TEM samples, then depositing nano-sized Au particles to form the model catalyst. Single crystal rutile TiO_2 samples were made by conventional TEM sample preparation techniques. Highly pure oriented single crystal plates (purity 99.98%, miscut <0.5°)were obtained commercially (MTI Crystal Inc.) and cut into 3mm discs using an ultrasonic cutter. These disks were subsquently mechanically polished to a thickness of about 100 microns and dimpled. After this, samples were thinned down by ion-milling (GATAN, PIPS) using 5 kev Ar^+ ions until perforation. The process of ion-milling affected the samples' stoichiometry and created defects and an amorphous region on the surface. Tube furnaces were then employed to carry out the requisite high temperature anneals to recover surface stoichiometry and crystallinity (the experimental parameters used will be described in detail in Chapter 4). Nano-sized Au particles were then deposited either by a wet chemistry method (see Chapter 6) or physcial vapor deposition (see Chapter 5).

2.3. Data Acquisition and Processing

Since almost all the results in this study were obtained by acquiring data using TEM, a discussion of different TEM data acquisition methods is justified. Either traditional film or a CCD camera has been used to record images or electron diffraction patterns, each method with its own advantages and disadvantages. Traditional film is available on most TEMs and has relatively high resolution compared to CCD. At the same time, the inefficiency of traditional film in responding to light (2%) turns out to be a good thing for recording electron diffraction patterns because the high intensity of the transmitted

and diffracted electron beams would easily burn out the CCD, which has light sensing efficiency of about 70%. On the other hand, the CCD has advantages in sensitivity, linearity, superior dynamic range, real-time feedback and image distortion. The digital pictures obtained can be transfered and processed conviniently. In this study, the majority of all images were recorded electronically. Fig 2.1 (a and c) show some examples of images captered by a CCD camera.

Transmission electron diffraction (TED) take advantage of the interaction between electron beams and the periodic arrangement of atoms. For decades, it has been the standard technique for the examination of crystal structures of 3-D bulk materials. Naturally, it has been extended to the surfaces and used for the determination of surface structure. The major advantages of TED include the isolation of a small region of interest, as a small probe can be formed to obtain information from an area with a size of several nanometers; the ease of data acquisition, since negatives or a CCD camera can be readily used in diffraction mode of any TEM to record a pattern; and the sensitivity to surface features, because in-plane periodicity of surface structures can be captured easily by TED, even if the thickness is no more than few layers of atoms. Since an electron has a significantly higher scattering probability than an X-ray, a dynamical treatment is required to interpret the data. Although data interpretation models for TEM have been established, it is still more complicated and less accurate than those for X-ray. In this study, a kinematical theory of diffraction can be used to approximate the more rigorous dynamical case for very thin crystals and far off-zone conditions (Marks et al. 1991).

Diffraction information from a small volume of material can be obtained by two different approaches: 1) illuminate a large region of the sample and use a selected area aperture

to limit the region contributing to the diffraction pattern, or 2) use a small probe (microdiffraction mode, use a smaller condenser aperture and spot size), thereby limiting the illuminated region. In the SA mode, regions outside the aperture may contribute to the diffraction pattern due to microscope imperfections (spherical aberration of the objective lens) or user error (incorrect focusing of objective lens) (Hirsch et al. 1977). The effect is made worse by the fact that different sections of the diffraction pattern are from different regions of the sample. All the diffraction patterns used in this study were obtained by the second approach, namely microdiffraction.

In the case of employing direct methods to solve surface structure, extreme care is needed in order to record the exact diffraction intensity on the film. Diffraction patterns were digitized using an Optronics P-1000 microdensitometer. The microsdensitometer was calibrated to be linear over the entire range of exposure series. The relative intensities of various surface diffracted beams were then measured using a cross-correlation technique developed and implemented using the SEMPER image procession language (Xu et al. 1994). The measurements from multiple negatives were then reduced to yield one measurement and an associated error for every measured reflection following standard statistical methods (Collazo-Davila 1999). These were then symmetry averaged to yield the final data set of symmetry independent beams.

As with any experiment, one has to take care that the sample is not altered by the probing radiation, and this is particularly important when dealing with a high energy electron beam. The effect of electron irradiation on oxides is a discipline that is well studied (Buckett 1991). For the TiO_2 system, beam damage is a serious setback only when high fluxes are used in TEM. In this study, besides TiO_2, nano-sized gold particles ($\leq$5nm)

were the central subject of the TEM research. It is known that nano-sized gold particles are easily affected by electron beams. Atomic rearrangements can be observed in real time by TEM, either in the form of change of crystal shape and orientation (Wallenberg and Bovin 1984; Bovin and Smith 1985) for small gold particles ($\leq$5nm), or by localized column hopping (Wallenberg et al. 1985) for bigger particles. Figure 2.3 provides an example of two adjacent gold particles coalescing under the beam. In this study, various precautions were taken to check for and minimize irradiation damage: low emission current and a spread beam were used whenever possible; region of interest of a sample was never exposed to electron beam if not necessary; snapshots were always taken before and after each study to insure the sample was not changed during observation. In most of the cases, the radiation damage was minimal.

Z-contrast imaging was used to detect extremely small gold particles. With this method, which is available in the JEOL HF2100F and VG Microscopes HB603U instruments, a fine electron probe is scanned over the region of interest while an annular dark-field detector records the electrons that are scattered into high angles by thermal diffuse scattering. Since the thermal diffuse scattering of atoms mainly depends on the atomic number, heavy atoms appear brighter in the image than light atoms, which enables distinguishing between very heavy elements and light elements. With aberration correction, single atom resolution can be reached (see Chapter 3). In general, sub-nanometer features can be detected due to the high contrast between gold and TiO_2 support. Figure 2.1(b,c and d) demonstrate some applications of Z-contrast imaging.

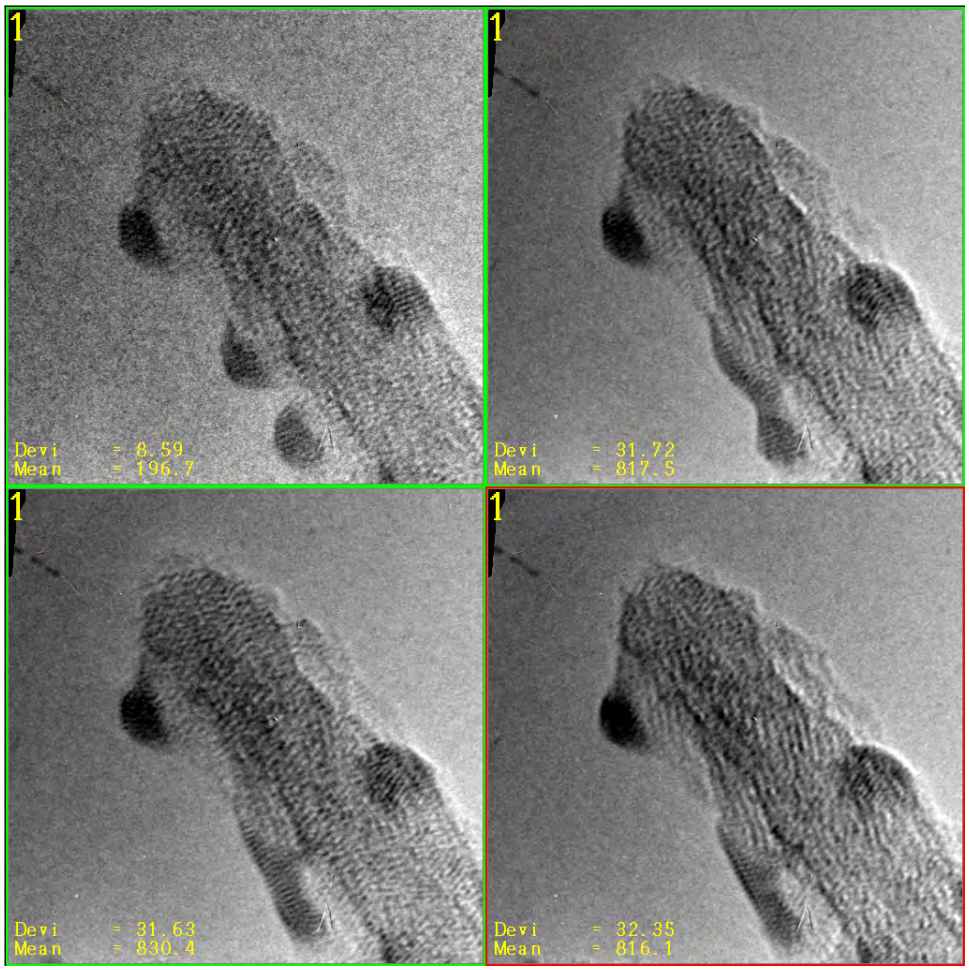

Figure 2.3. Two adjacent gold particles in gold catalysts coalesce under the electron beam of TEM, several seconds between each frame was taken

2.4. Direct Methods

Despite their ability to provide direct structural information at the atomic scale, imaging techniques are seldom sufficient to solve a surface structure due to limitations in the resolution from the weak signals. The resolution obtainable in a diffraction experiment is far superior, and the process of data collection is parallel and fast, without the complications of radiation damage. Unfortunately, direct fourier inversion of the acquired

intensities is impossible since the phases of the scattered beams are lost in the diffraction experiment. However, the intensities can be used with various structure determining techniques, collectively known as Direct Methods (Landree et al. 1997, 1998; Marks 1999; Marks et al. 2001), to yield a reasonable estimate of the true surface structure. Crystallographic Direct Methods have become popular for surfaces over the last decade and have been successfully used to solve various structures. In simple terms, Direct Methods exploit *a priori* information to constrain the phases of measured reflections. The common constraints used are:

(1) Atomicity : Scattering originates from atoms and hence the solution should have atomic features i.e. regions of large charge densities separated by charge-free regions.

(2) Positivity : Charge density in a real crystal is always positive

(3) Localisation : The region of space with significant atomic displacements (from bulk positions) is limited to the near-surface region.

The phases of the measured reflections cannot be totally random - i.e. they have to obey the above constraints and this can be used to gauge the 'figure of merit' (FOM) of a given set of phases. These constraints are iteratively imposed in a Gerchberg-Saxton fashion (Gerchberg and Saxton 1972) using a projection onto convex sets algorithm (Combettes 1996) to refine the phases of the measured reflections. The solution space is spanned effectively by multi-solution search technique, namely a genetic algorithm (Landree et al. 1997; Goldberg 1997). A detailed review of the theory behind Direct Methods for surfaces and the various details of the current implementation is published elsewhere (Marks 1999; Marks et al. 2001). The top solutions obtained from Direct Methods can be used

to generate scattering potential (electron) or charge density (x-ray) maps. These maps with atoms assigned to regions of high intensity, provide models that can then be used as the starting point for further refinements. Most often, only a part of the structure can be identified from these maps owing to unmeasured reflections and experimental errors. The various techniques employed for structure completion include fourier-difference methods, projection-based methods (Cowley 1986) and heavy atom holography (Dorset 1997). The structure so determined can be further refined by using the conventional R-factor or χ^2-type analysis against simulated data.

2.5. Other Experimental Techniques

To understand a catalyst, it is important to characterize its catalytic properties. Various techniques, including gas chromatography (GC), temperature programed reduction (TPR), Fourier transform infrared (FTIR) spectroscopy, Raman and etc. were employed to examine every catalysis process, from sample preparation, activation, deactivation to reactivation; to explore all the factors influencing its activities; and to build up a model to explain the reaction mechanism. If not being indicated otherwise, all the catalytic prosperities referenced in this study are from such work.

X-ray photoelectron spectroscopy (XPS) is a surface sensitive analytic tool to study the surface composition and electronic state of a sample. Although the X-rays penetrate a substantial distance into the sample ($\sim$mm) and excite electrons (photoelectrons), only a small fraction of these electrons from about the top 5 nm make it outside the sample and are detected. The XPS used in this study is attached to the UHV sample preparation and characterization system (SPEAR) and is composed of a FEI x-ray source and a PHI

electronics spherical electron energy analyzer. It was used on various occasions, including detecting the chemical state of TiO_2 support and gold particles in real catalysts and model catalysts, examining the cleanliness of the surface before and after treatment to exclude the possibility of contamination, and measuring the gold coverage on catalyst sample after preparation. Since XPS analyzes surface exit electrons with relatively low energy, special care needs to be taken to insure trustworthy results. One precaution is to maintain the UHV environment of the chamber, which is difficult for real catalyst samples. Real catalyst samples contain moisture introduced at the stage of sample preparation which can not be removed without permanently changing the catalyst. Extra long pumping and dry ice cold trapping were found to be a good method for reducing water out-gasing. Charging was inevitable in some cases due to the nature of the sample (powdered and semi-conductive), accordingly the carbon 1s peak with a binding energy of 284.7ev was used as a reference.

X-ray adsorption related techniques (Extended X-ray Absorption Fine Structure, EXAFS and Near Edge X-ray Absorption Fine Structure, XANES) utilize the information produced by the interaction between intense synchrotron irradiation and the target sample. XANES spectroscopy corresponds to the transition from a core-level to an unoccupied orbital or band and mainly reflects the electronic state (chemical state of certain species). In contrast, the oscillatory structure of EXAFS results from the interference effect between an emitted electron from an X-ray absorbing atom and scattered electrons by surrounding atoms and provides information on the local structures around an X-ray absorbing atom (particle size and coordination number). To take advantage of X-ray's non-destructive nature (in most cases), *in situ* experiments had been taken to obtain chemical and catalytic

information of the sample as the same time. Furthermore, the strong signal produced by strong incident beams made time resolution experiments possible (see Chapter 3). In this study, all the synchrotron experiments were carried out at Beamline 5-BMD of the DuPont Northwestern Dow Collaborative Access team at the Advanced Photon Source at Argonne National Laboratory in Argonne, IL. Results were collected as a team and data analysis was carried out by Dr. C.K. Costello and J.H. Yang from the chemical engineering department.

In order to use model catalysts to explain some properties of real catalysts, some connection must be made between these two. In this study, an effort was made to obtain catalytic activities from model catalysts (see Chapter 6). Compared to real catalysts, model catalysts can only provide a very limited amount of surface area, subsequently, the gold loading for model catalysts was much lower (about 10^{-6}) than for real catalyst. Experiments were designed to try to detect trace amount of reaction products. FTIR and mass spectrometry were used for this purpose. In this study, FTIR was used as a GC detector, where its power for identifying compounds was coupled with the remarkable ability of GC to separate the components of complex mixtures. Mass spectrometry works by converting components of a sample into rapidly moving gaseous ions and separating them on the basis of their mass-to-charge rations. Its sensitivity, fast data collecting speed and ability to distinguish compounds composing of two isotopes make it a preffered tool for real time isotope experiments. In this study, the FRIR and mass spectrometry experiments were carried out by Juan D. Henao.

CHAPTER 3

Studies on Oxide Supported Au Catalysts

3.1. Catalysts Preparation And Catalytic Properties

3.1.1. Catalysts preparation

Au/Al_2O_3 and Au/TiO_2 catalysts were the foci of this part of study. They were prepared by the deposition-precipitation method, similar to the procedure of Haruta et al. (Tsubota et al. 1991; Haruta et al. 1993). 40 mL of a 8.4 mM $HAuCl_4$ (Aldrich, 99.999%) solution was heated to 70℃ while stirring. Then the pH was adjusted to 7 with NaOH. Initially, the solution was yellow, with a pH of around 4.5, and it became colorless as the pH was increased. This solution was added rapidly with vigorous stirring to 2.5 g of the support suspended in 60 mL of deionized H_2O at 70℃ and the aged for 1 hour. This procedure was carried out with minimal exposure to light in order to avoid possible light reactions of the Au precursors.

The suspension was then suction filtered, and the solid was resuspended in 50 mL of deionized H_2O at room temperature, stirred for 10 min, and then suction filtered again. This procedure was repeated with another 50 mL H_2O at room temperature, followed by 50 mL of H_2O at 50℃. The resulting solid was dried in air at room temperature overnight. This sample is the "as prepared", or "uncalcined", sample. The calcined sample was prepared by heating up the as-prepared sample at 350℃ for 4 hours in air. All samples were stirred in air in a vial with no exposure to light. The chloride content of

the catalysts was not determined, but, from previous experience, it should be below the detection limit of 0.01 wt%Cl, or a Cl/Au atomic ratio <0.03.

This preparation method consistently yields excellent Au catalysts on various supports with an average gold particle size of less than 5 nm. As prepared, they are mainly ionic gold species on the surface. The detailed characterization will be described later in this chapter.

3.1.2. Catalytic properties of Au catalysts

Catalytic properties of Au catalysts supported on various of oxides were studied here at Northwestern University, especially CO oxidation on Au/Al_2O_3 and Au/TiO_2. The reaction studies were carried out in order to understand the process of activation, deactivation, and regeneration and how the catalytic properties were affected by various factors, including preparation methods, pretreatments, and temperature. The active site and catalytic mechanism were elucidated using various experimental techniques, including Fourier Transform Infrared Spectroscopy (FTIR), temperature programmed reduction (TPR) by H_2, Diffuse Reflectance Fourier Transform Infrared Spectroscopy (DRIFTS), XPS, and synchrotron X-ray Adsorption Spectroscopy (XAS, including XANES and EXAFS).

The major findings from studies on Au/Al_2O_3 catalysts are (Costello et al. 2002, 2003, 2004; Kung et al. 2003; Costello 2003): metallic Au must be present in the $Au/\gamma\text{-}Al_2O_3$ catalysts in order to effect CO oxidation, and H_2O is necessary to activate and regenerate the catalysts, as it enhances the reduction of Au during activation. Consequently, a model of the active site for CO oxidation over supported Au catalysts consisting of metallic

Au atoms and Au^+-OH^- has been proposed, along with a corresponding model for the reaction mechanism.

The studies on Au/TiO_2 catalysts indicate that this catalytic system shares many common characteristics regarding to the active site and the reaction mechanism as Au/Al_2O_3, but with one order of magnitude higher activity for the CO oxidation reaction. Au/TiO_2 catalysts are much easier to activate, compared to Au/Al_2O_3. The activation process was found (Yang et al. 2005) to begin with an induction period when sites for nucleation and reaction, consisting of reduced Au species, are formed; ionic Au species were then further reduced until gold particles with an average diameter of 1 to 1.5 nm are obtained.

During the above studies, TEM and other techniques played an important role in helping to understand oxide supported catalysts by clarifying the effects of various parameters, including preparation methods, treatments, and supports on catalytic properties of a Au catalyst by monitoring changes in the size and structure of gold nanoparticles. These findings usually provide guidance for the subsequent studies and sometimes offered insight into the reaction mechanism for CO oxidation on Au catalysts.

3.2. Effects of Chlorine on Supported Au Catalysts

3.2.1. Objective and experiments

The properties of a supported Au catalyst are highly sensitive to preparation conditions. It is very important to understand and control the variables important in the preparation of these catalysts. Chlorine-containing precursors are commonly used in the preparation of Au catalysts. It is well known that the average gold particle size is large for catalysts with high residual Cl^- contents, but there are few details available on how Cl^- influences

the evolution of the gold particle morphology. It is also not clear whether Cl^- also inhibits catalytic activity. The goal of this research is to provide a clearer understanding of the impact of Cl^- in order to permit a better evaluation of other factors important in the preparation of Au catalysts. Specifically, one objective of this work is to confirm the agglomeration of gold particles by Cl^- and to determine how the growth of gold particles depends on the Cl^- content. The second objective is to establish whether Cl^- has any direct effect on the catalytic activity. These objectives were accomplished by examining the changes in gold particle size and catalytic activity when Cl^- is removed or quantitatively added to a catalyst. As a control, a Au catalyst without chlorine content was also prepared and tested.

Gamma-Al_2O_3 was used as support for Au catalysts, and three types of Au/Al_2O_3 catalysts were prepared. The first was prepared with the $HAuCl_4$ precursor by deposition-precipitation method as described earlier. The only exception was NaOH was not added to increase pH value. In this way, a high concentration of Cl^- was left on the surface of the catalyst. Some of the catalysts were then treated with Mg citrate either before or after calcination, which was carried out at at 350℃ for 4 hours. The second type was prepared with Au acetate by incipient wetness method (not described). The third type was prepared with $HAuCl_4$ precursor by deposition-precipitation method as described earlier.

TEM was used to examine the particles size of Au/Al_2O_3 catalysts before and after various treatments. Size distribution of gold particles were carried out by measuring between 100 to 300 individual particles at various locations of a catalyst sample. The average particle size was then calculated. The analysis of chloride concentration in the

catalysts was done by monitoring HCl during H_2-TPR with FTIR. The catalytic properties of the catalysts were tested by running either selective CO oxidation reaction (1%CO, 0.5%O_2, 48%H_2 and balance He) or CO oxidation reaction (1%CO, 0.5%He and balance He) at 100℃.

3.2.2. Results and discussion

3.2.2.1. Au/Al_2O_3 catalysts prepared with $HAuCl_4$. Figure 3.1 shows the TEM images of calcined Au/Al_2O_3 catalyst prepared from $HAuCl_4$ with no pH adjustment and after the catalysts was treated with Mg citrate either before or after calcination. The size distributions of gold particles for these samples were compared in Figure 3.2. It was found that addition of Mg citrate before calcination (Figure 3.1a) resulted in much smaller gold particles than in the other two cases (Figure 3.1b, c). At the same time, the sample not treated with Mg citrate and that treated with Mg citrate after calcination yielded similar particle size, which indicates that addition of Mg citrate didn't affect the particle size after the catalyst was calcined.

The purpose of adding Mg citrate to the sample was to remove the residual chloride from the surface of the catalysts. The effectiveness of the removal was observed from the changes of residue chlorine level, expressed by molar ratio of chlorine to Au, in these samples. For samples treated with Mg citrate, the residue chlorine level was reduced from 0.98 to 0.03 wt%, whether the treatments happened before or after calcination. Since all the catalysts had similar Au loadings and differed only significantly in their chloride content, it appears that elevated temperature induced the agglomeration of Au in the presence of high residual chloride.

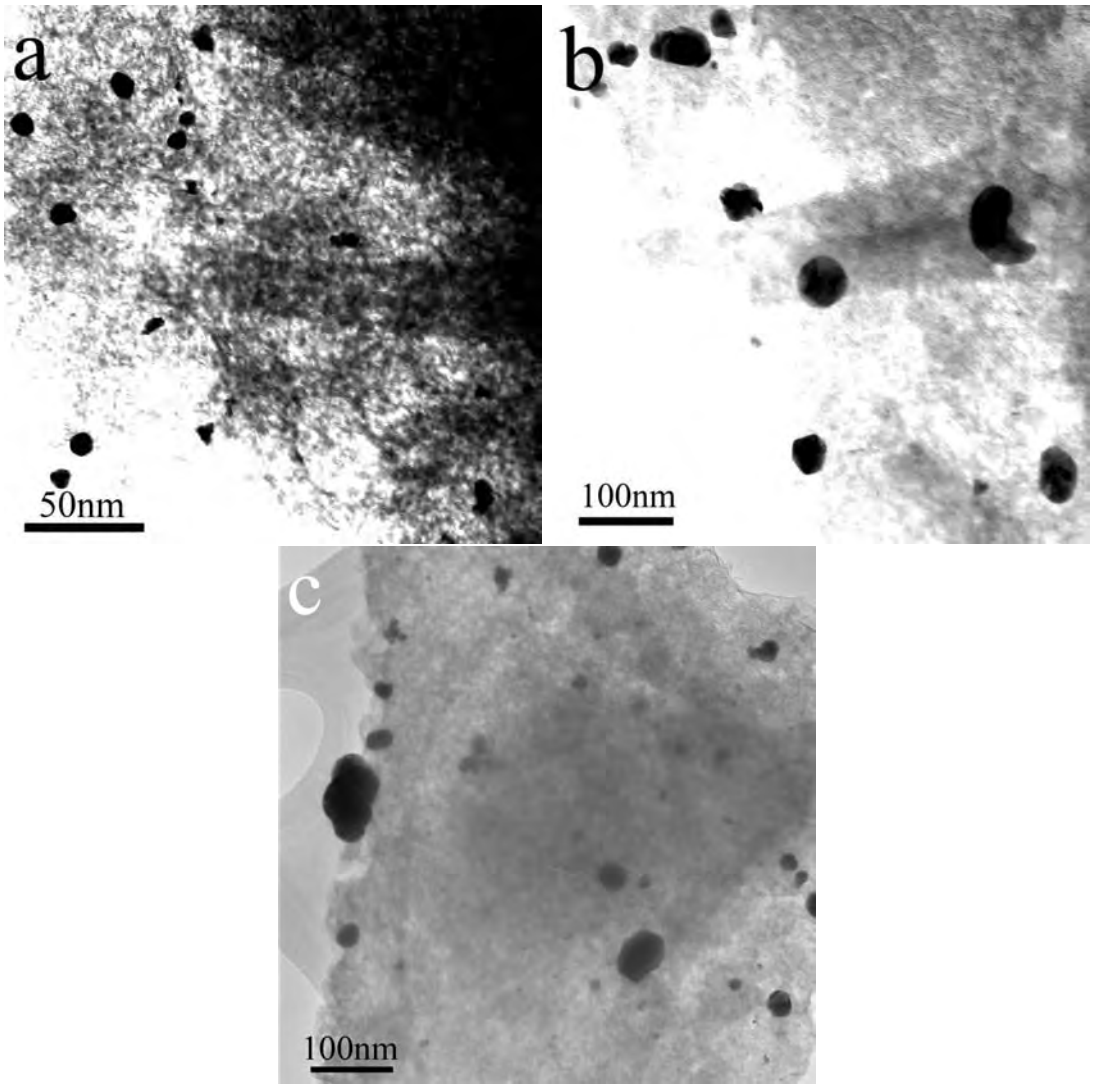

Figure 3.1. TEM images of catalysts prepared with $HAuCl_4$, with the addition of Mg citrate (a) before calcination, (b) after calcination, (c) with no Mg citrate addition.

3.2.2.2. Au/Al_2O_3 catalysts prepared with Au acetate. To examine the effect of chloride on gold particle size, chloride was added as a post-synthesis treatment to calcined catalysts. Two types of catalysts were examined. In the first series of experiments, chloride was added to catalysts prepared with a chloride-free precursor and, in the second,

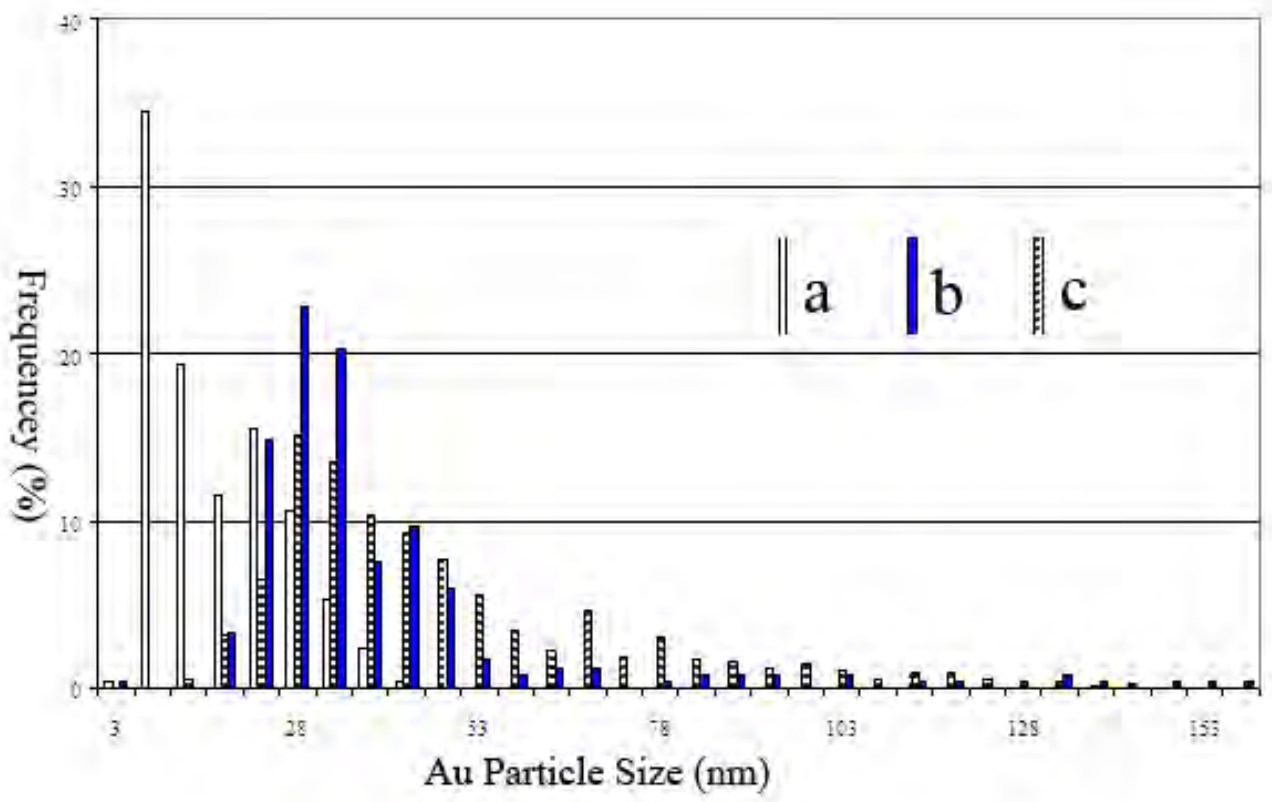

Figure 3.2. Size distribution of Au particles on Au/Al_2O_3 catalysts prepared with $HAuCl_4$, with the addition of Mg citrate (a) before calcination, (b) after calcination, (c) with no Mg citrate addition.

to catalysts prepared under conditions where the residual chloride content should be low. Figure 3.3 shows the TEM images of Au/Al_2O_3 prepared using a gold acetate precursor. The gold particles shown in these pictures were representative of the majority of the particles present. They were small and generally well separated from one another. However, occasionally, there were a few scattered clusters of larger Au particles (not shown). The presence of clusters of larger gold particles was probably due to the fact that Au acetate is only sparingly soluble in water. Thus, some solid particles of Au acetate were introduced onto Al_2O_3 during impregnation. While some of the Au particles looked distinctly nonspherical , they are definitely single crystals with various shapes(e.g. Figure 3.3c2). The average particle size of the as-calcined, further heat treated, and chloride-treated samples were 4.8, 5.8, and 7.9 nm, respectively, and the particles counted to obtain these values ranged from 148 to 223 particles. Figure 3.4 shows the size distribution on these catalysts. The clusters of larger Au particles were not plotted in this graph for clarity, and also because they were very scarce. The average gold particle size of the chloride-treated sample had almost doubled and the population distribution broadened relative to the parent catalyst. Although this sample was heated for 4 hours at 350℃ after the addition of chloride, the agglomeration was primarily the effect of chloride because the increase in gold particle size of the sample subjected to an identical heat treatment of the calcined catalyst was significantly less.

3.2.2.3. Au/Al_2O_3 catalysts prepared with $HAuCl_4$ and NaOH. Similar increases in average gold particle size due to Cl^- addition (Figure 3.5, 3.6) were observed for catalysts prepared with $HAuCl_4$ precursor at pH 7 and 70℃. These synthesis conditions minimized the residual chloride on the catalysts due to replacement of chloride ligands

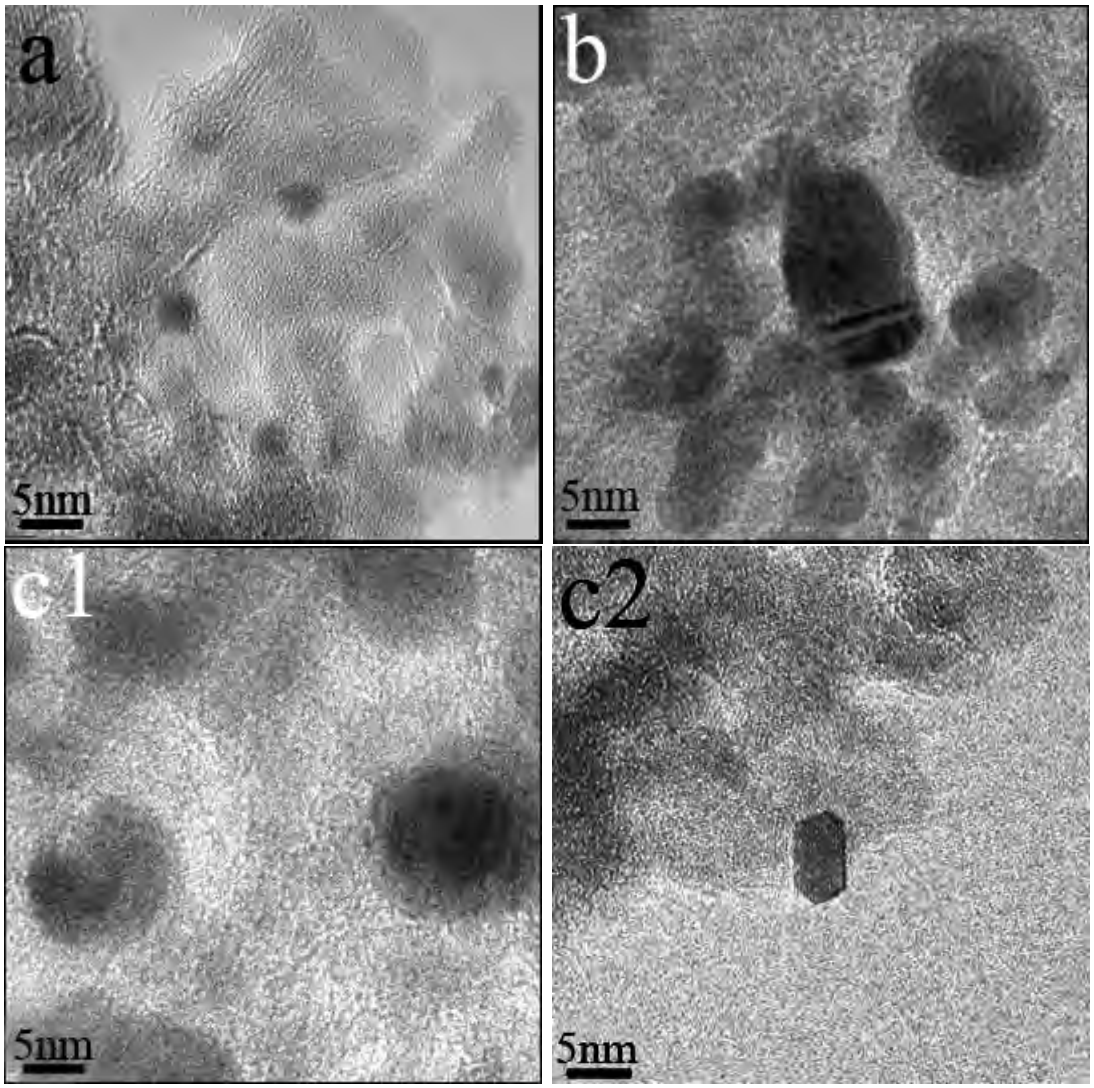

Figure 3.3. TEM images of Au/Al_2O_3 prepared from Au acetate precursor: (a) as calcined; (b) additional 4 hours calcinations at 350℃; (c1) and (c2) catalyst with 0.3 wt.% Cl added (Cl/Au=0.15) and then calcined at 350℃ for 4 hours.

with hydroxide ligands (Kozlov et al. 1999) and suppression of Cl^- adsorption on Al_2O_3. It is interesting that most of the agglomeration of gold induced by the presence of chloride took place at the low temperature of 100℃.

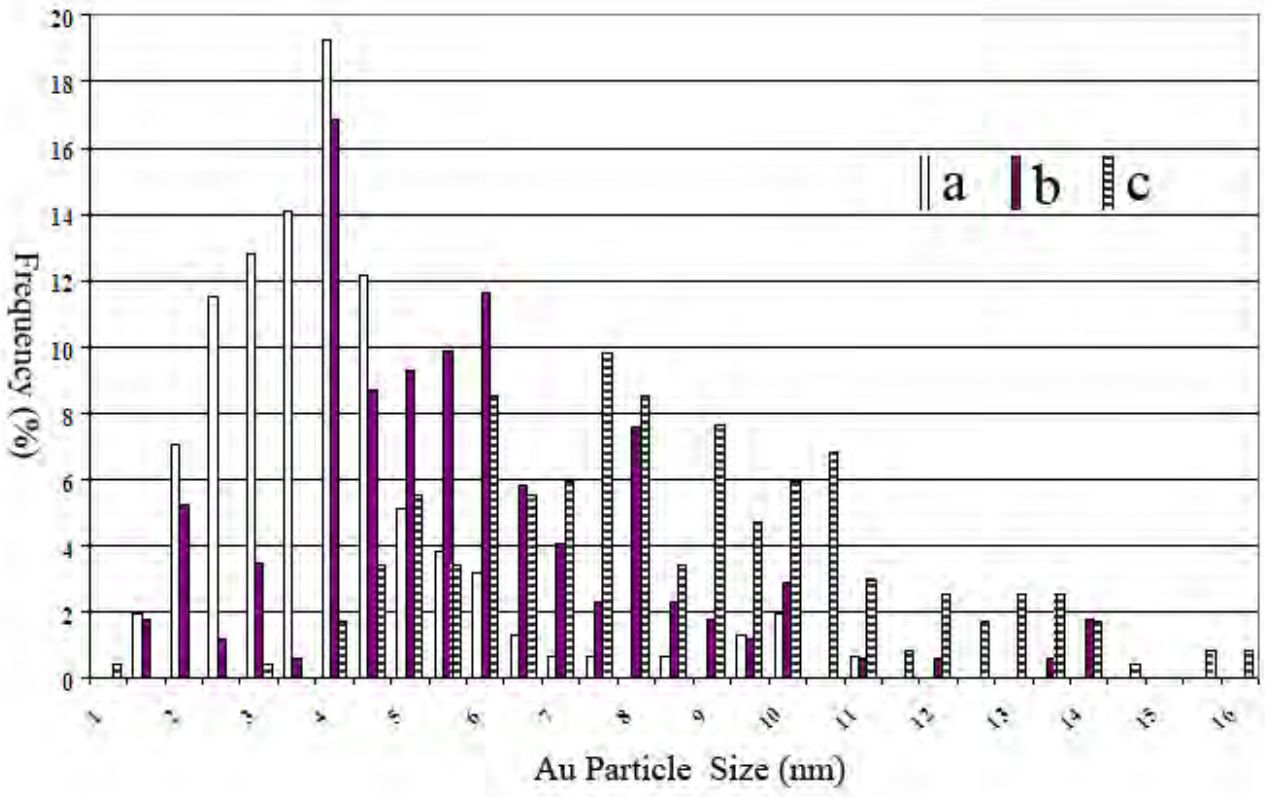

Figure 3.4. Size distribution of Au particles on Au/Al_2O_3 prepared from Au acetate precursor: (a) as calcined; (b) additional 4 hours calcinations at 350°C; (c) catalyst a with 0.3wt% Cl added (Cl/Au=0.15) and then calcined at 350°C for 4 hours.

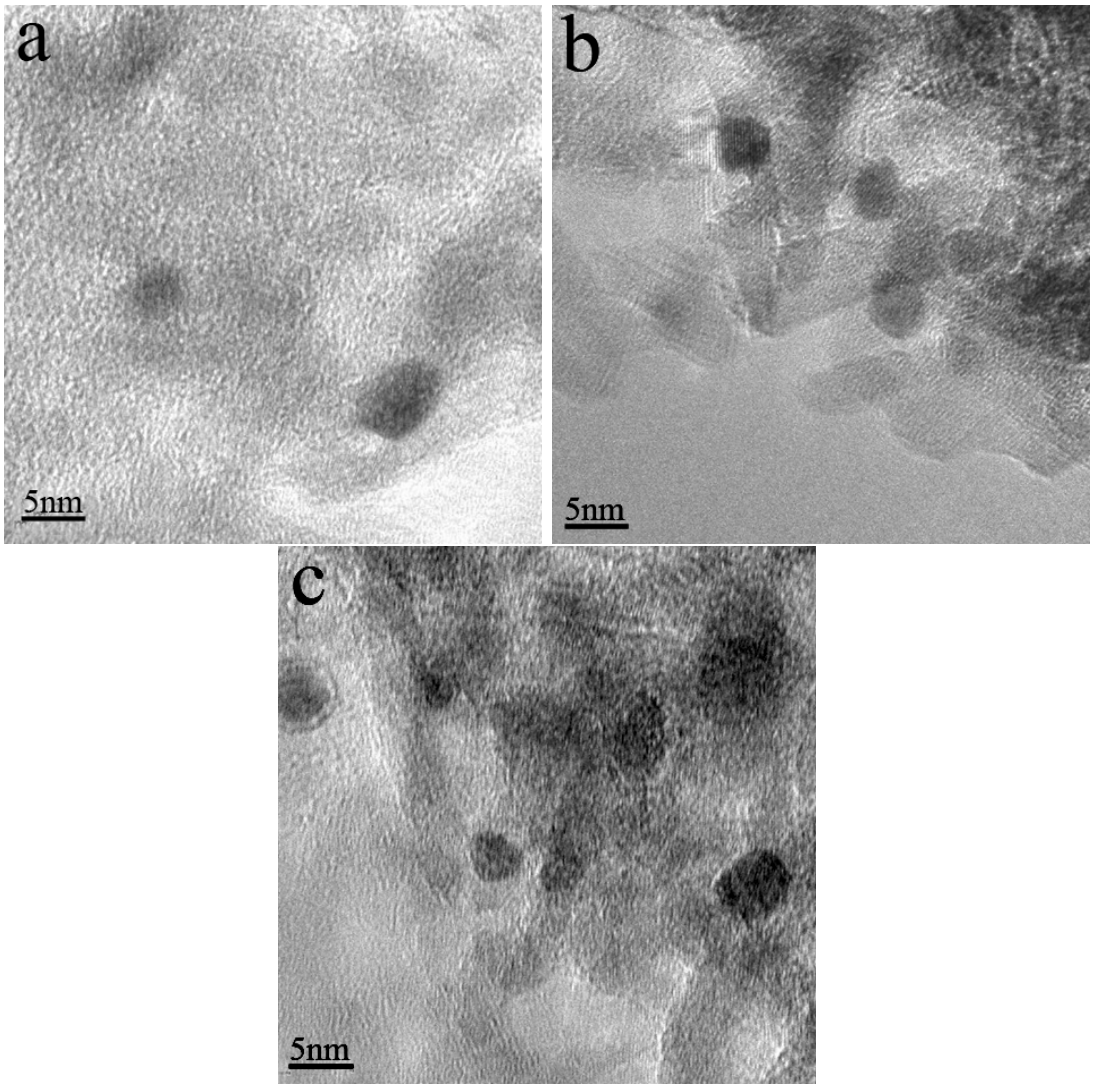

Figure 3.5. TEM images of Au/Al_2O_3 prepared by hydrolyzing $HAuCl_4$ at pH7 and 70℃: (a) as calcined; (b) catalyst with 0.3 wt% Cl added (Cl/Au=0.15) and then heated at 100℃ for 1 hour; (c) catalyst with 0.3 wt% Cl added (Cl/Au=0.15) and then heated at 350 ℃ for 4 hours.

3.2.3. Catalytic properties

The effect of chloride on the activity was examined by observing the changes in the catalytic properties upon removal, addition and calcination with addition of chloride.

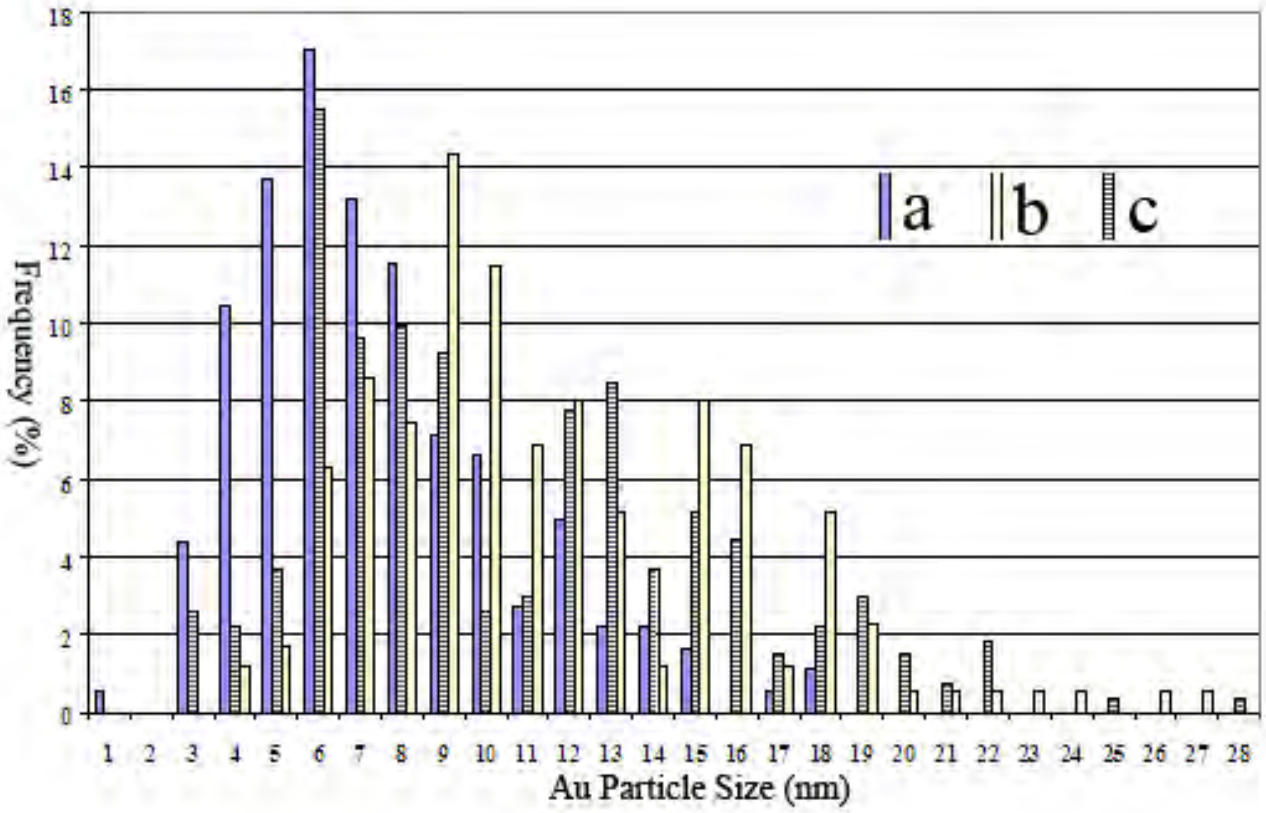

Figure 3.6. Size distribution of Au particles on Au/Al_2O_3 prepared from $HAuCl_4$ at pH7 and 70℃: (a) as calcined; (b)catalyst with 0.3 wt% Cl added (Cl/Au=0.15) and then heated at 100℃ for 1 hour; (c) catalyst with 0.3 wt% Cl added (Cl/Au=0.15) and then heated at 350 ℃ for 4 hours.

Table 3.1 show the catalytic properties of various samples studied. The catalysts prepared with $HAuCl_4$ showed changes in the catalytic property upon removal of residual chloride. The oxidation activities of the catalyst that contained high residual chloride were very poor, but improved greatly after chloride removal with Mg citrate treatment. Mg citrate treatment before calcination resulted in catalysts with the highest oxidation activities.

The impact of chloride addition to catalysts prepared with Au acetate is shown in the table too. The CO oxidation activity of the as prepared catalyst prepared with Au acetate was nearly 30 times better than the as pepared catalyst prepared with $HAuCl_4$ at low pH value. Additional heating and chloride decreased the activity. Similarly, addition of chloride to the catalyst prepared with $HAuCl_4$ at pH 7 and a higher temperature resulted in a decrease in activity. The decrease was less when the sample was heated to only 100℃ after the chloride addition than when the sample was heated to 350℃.

3.2.4. Conclusions

After considering all of the above results, the dual role of Cl^- in suppressing the CO oxidation activity of a Au/Al_2O_3 catalyst can be concluded: accelerating the agglomeration of gold particles and poisoning the active sites. Considering the fact that only a small amount of Cl^- was needed for poisoning, and the amount of residual Cl^- on the catalyst is determined by the pH value during deposition-precipitation and the rinsing afterwards, one can make the conclusion that this certainly is one of the reasons why the activity of a Au catalyst is so sensitive to preparation conditions. In this study, TEM provided quantitative characterization of the change of gold particle size for all of the

Table 3.1. Physical characteristics and SCO activities of Au/Al_2O_3

Precursor	Treatment	Average Au particle size (nm)	molar ration Cl^-/Au (wt%)	CO activity
$HAuCl_4$ w/o NaOH	Mg citrate before calcination	1.8	16.7	1.2±0.1
	Mg citrate after calcination	2.0	49.6	0.96±0.1
	No Mg citrate	2.2	44.6	0.05±0.03
Au acetate	Calcined	4.8	$5.3x10^{-4}$	28±0.2
	+350℃(4h)	5.8	$5.3x10^{-4}$	8.2±0.3
	+Cl+350℃(4h)	7.9	$5.3x10^{-4}$	2.3±0.1
		7.9	0.03	4.1±0.2
$HAuCl_4$ w/ NaOH	Calcined	8	-	42±1
	+Cl+150℃(1h)	11.2	0.15	51±2
	+Cl+350℃(1h)	12.3	0.05	24±1

samples. By comparing the particle size distributions, the effect of Cl^- in accelerating the agglomeration of gold particles was clearly demonstrated.

3.3. Activation of Au/γ-Al_2O_3 Catalysts for CO Oxidation

3.3.1. Objective

After supported Au catalysts were reported to be very active for CO oxidation at low temperature, tremendous efforts have been made to understand the origin of this surprising catalytic property. However, the nature of the active sites and the mechanism of the CO oxidation reaction remain unknown. Nonetheless, it is well established that the activity of supported gold prepared by deposition-precipitation or coprecipitation methods depends strongly on the pretreatment conditions and, more generally, on the history of the sample.

The recent investigations have been focused on the effects of the pretreatments, especially the calcination temperature. Most of the research uses either the oxidation state of gold species or the size of gold particles to explain the experimental results obtained from characterizing catalytic properties of the gold catalysts calcined at different temperature. Sometimes, conflicting conclusions were made on similar findings. For examples, Au/TiO_2 catalysts were found to have a decreasing activities as calcination temperature increased from 100 to 400 ℃. Park et al. (Park and Lee 1999) suggested that the cationic Au species are responsible for the higher catalytic activity because their XANES and XPS results indicated gold was reduced with increasing temperature. However, Wolf et al. (Wolf and Schuth 2002) noted that, after calcination at 400℃, the samples should contain entirely metallic gold, yet they still exhibited respectable activity for CO oxidation. Therefore, they concluded that metallic gold is active and the decrease in catalytic activity with

increasing temperature is associated with the corresponding increase in gold particle size and decreasing surface area. Boccuzzi et al. (Boccuzzi et al. 2001) suggested a similar interpretation, but failed to explain that while the gold particle sizes in the samples calcined at 300 and 400℃ were approximately the same, the former showed higher CO oxidation activity.

The attempts to explain the activation process of Au/Al_2O_3 catalysts encountered the same problems; between oxidation state and the particle size, which factor contributes more to the activation? The smaller and more reduced gold particles seem to be better for catalytic activities. But free (reduced) gold particles always tend to agglomerate. The objective of this study was to provide an insight into this problem by combined knowledge from catalytic properties characterization, and TEM and XANES studies of the Au/Al_2O_3 catalysts.

3.3.2. Results and discussion

3.3.2.1. Catalytic activity for CO oxidation. Much work has been done to study activation of Au/Al_2O_3 catalysts for CO oxidation at low temperature. Table 3.2 summarizes the main experimental results. The best activation condition for Au/Al_2O_3 was found to be 30 min H_2 at 100℃, then 30 min H_2+H_2O at 100℃. Various combination of a reducing gas and H_2O seem to be the key for a successful activation. A better understanding of this activation process can be achieved by studying the size and oxidation state of the gold particles.

3.3.2.2. Electron microscopy study on activation of Au/γ-Al_2O_3. TEM pictures in Figure 3.7 demonstrate the effects of various treatments on gold particle size for

Table 3.2. Activation of Au/Al_2O_3 for CO oxidation

Exp. No.	Pretreatment condition	initial CO conversion (%)	Initial CO oxidation rate mol CO/mod Au-s
1	30min CO O_2 + H_2O at room temperature	0	0
2	Calcined 350℃ for 4 h in air	25	0.12
3	30min Co O_2 + H_2O at 100℃	49.4	0.25
4	30min H_2 O_2 at 100℃	62.3	0.31
5	30min H_2 at 100℃, 20min He at 100℃, 15min O_2 at 100℃	1.5	0.007
6	2h H_2 at 100℃	1.5	0.007
7	1h H_2 +1.5℃ H_2O at 100℃	1.5	0.07
8	1h 1% CO + 1.5% H_2O at 100℃& 23.1	0.12	
9	1h 1.5% H_2 in He at 100℃	1	0.005
10	30min H_2 at 100℃, 30min H_2+ H_2O at 100℃	71	0.35
11	2h H_2 at 100℃, 30min 1.5% H−2O/He at room temperature	59.6	0.3
12	30 min 1%CO at 100℃, 30min 1%CO + H_2O at 100℃	56.9	0.28

Au/Al_2O_3 catalysts. Compared to an uncalcined catalyst (Figure 3.7a), the applied treatments, such as activation (Figure 3.7c, H_2 3 0min, and H_2+H_2O 30 min at 100℃), deactivation (Figure 3.7d, He 1 hour at 100℃) and regeneration (Figure 3.7e, H_2O 30 min at room temperature) made no obvious change to the particle size. It is noteworthy that subtle changes of particle size introduced by treatments might not be detectable due to the limited resolution of the microscope and finite sampling area. On the other hand, after calcination (Figure 3.7b, 350℃ for 4 hours), the catalysts show an obvious increase in particle size.

As discussed earlier, the interference from the support and the limitation of finite sampling area make it difficult to perform quantitative characterization at an atomic level on Au catalysts. There are two ways to overcome this obstacle. One of them is to build up model catalyst system and start with a uniform and low contrast surface, which will be discussed in Chapter 4. The other one is to improve the contrast between gold particles and supports by carrying out Z-contrast imaging using STEM.

The Z-contract imaging of activated Au/Al_2O_3 was obtained through collaboration with the STEM group (S. Pennycook, A. Lupini, et al.) at ORNL. Since STEM can produce a high contrast signal between light and heavy elements, this technique is especially suitable for Au catalyst studies. The HB603U STEM at ORNL is equipped with an Nion aberration correcter and is capable of providing information down to 0.6Å, which enables us to detect single gold atoms and find out the structure of gold species in Au catalysts. By using traditional TEM, gold nanoparticles with sizes down to sub-nanometer can be imaged. However the unpredictability of surface condition in Au catalysts makes isolated atoms and clusters invisible in many cases. Since these isolated atoms and clusters are

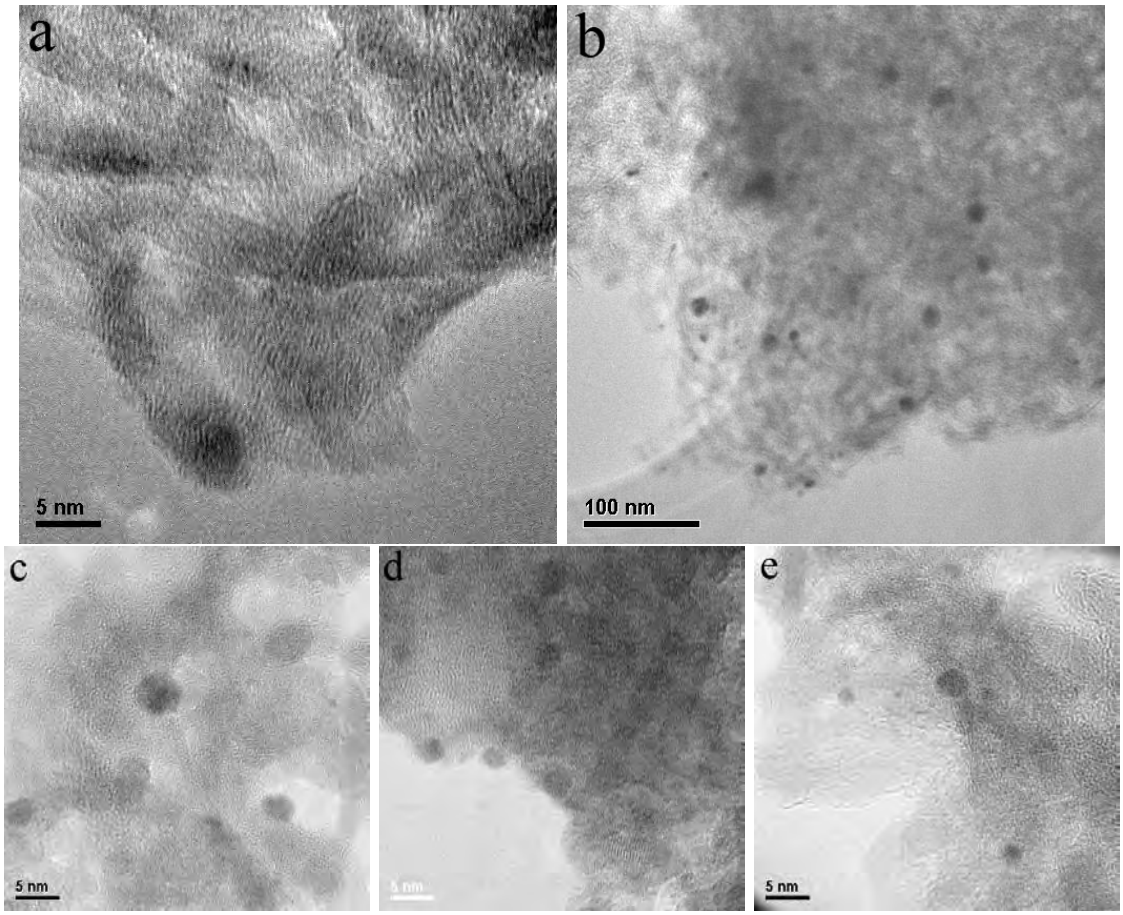

Figure 3.7. TEM images of Au/Al_2O_3 after various treatments: (a) uncalcined (as prepared); (b) calcined at 350℃ for 4 hours; (c) activated by H_2+H_2O at 100℃ for 1 hour; (d) deactivated by He at 100℃ for 1 hour, (e) regenerated by H_2O at room temperature for 30 minutes.

thought to be the most unstable and ionic in nature, they might be the key to understand the activation process of Au catalysts at the atomic level.

Activated Au/Al_2O_3 catalyst was studied using STEM. In these catalysts, there are still a large number of isolated gold atoms (Figure 3.8a). As for the larger particles (Figure 3.8b), they have various irregular shapes and are not well faceted. Even though activation has occurred, these isolated atoms and gold clusters seem to be quite stable. Although

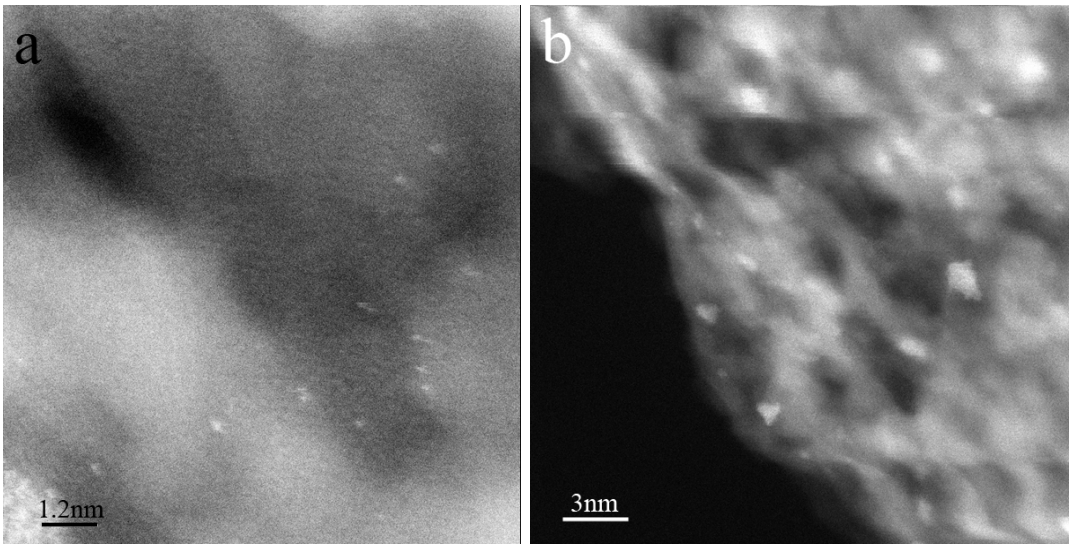

Figure 3.8. Au/Al_2O_3 catalyst after H_2 30min, then H_2+H_2O 30min at 100℃ activation: (a) isolated gold atoms; (b) gold clusters.

no apparent size difference was observed on Au/Al_2O_3 catalysts with various catalytic properties, these atoms and clusters might respond well to the treatments, exhibit certain chemical properties, and represent the catalytic activities of the whole catalyst.

In order to verify this assumption, knowing the chemical state of these gold species is very important. Direct observation of the change of chemical states in gold clusters would help to clarify issues related to the above assumption. Unfortunately, techniques with high spacial resolution, such as EELS, are not suitable for the study of gold. A well controlled model catalyst system is a good way to start, since the knowledge obtained by characterizing a large number of uniformly distributed (in space and composition) gold species is more representative and definitive. Although only an overall averaged chemical state information is attainable from the techniques, such as XPS and XANES, further understanding the Au catalysts can still be achieved.

3.3.2.3. *In situ* XANES study on activation of Au/γ-Al_2O_3. XAS has proved to be a fast, non-surface sensitive, and non-destructive technique to examine the chemical state and atom local environment. For catalyst samples, one major advantage of XAS is that data can be collected *in situ* while carrying out reactions. Therefore, XAS data can be straightforwardly correlated to the catalytic properties without introducing more variables if done otherwise. In this study, XANES was used to study the oxidation state of the gold catalysts.

Figure 3.9 shows the X-ray absorption spectrum of Au at the 11.919 keV edge for a number of compounds. The intensity of the white line, which occurs at about 11.922 keV and corresponds to a 2p3/2 f 5d transition, is proportional to the density of unoccupied d states, which is the highest for Au^{3+} (Figure 3.9a) in gold acetate and $Au(OH)_3$ and decreases as the Au in the sample is reduced to Au^+ (Figure 3.9c) and further to metallic Au. Au^{3+} is also characterized by a shoulder at 11.939 keV and an intense broad peak at 11.968 keV. Au^0 (Figure 3.9d) is characterized by a shoulder at 11.923 keV and peaks at 11.934, 11.947, and 11.971 keV. The Au^+ spectrum is similar to that of Au^{3+}, but with an intermediate white line intensity. These spectra did not change from one scan to another, indicating the absence of beam damage of the sample. The spectrum of an inactive, as-prepared sample is shown in Figure 3.9b. The intense absorption at 11.922 keV suggests that all the Au in this sample was Au^{3+}, presumably as $Au(OH)_{4-x}Cl_x$.

Figure 3.10 shows the change of oxidation state during activation of the as prepared Au/γ-Al_2O_3 catalyst. Figure 3.10b shows the spectrum of the same sample after treatment at 100℃ in H_2 for 30 min. Based on the decrease in the white line intensity and the broad peak at 11.986 keV, it is apparent that reduction of some of the Au in this sample had

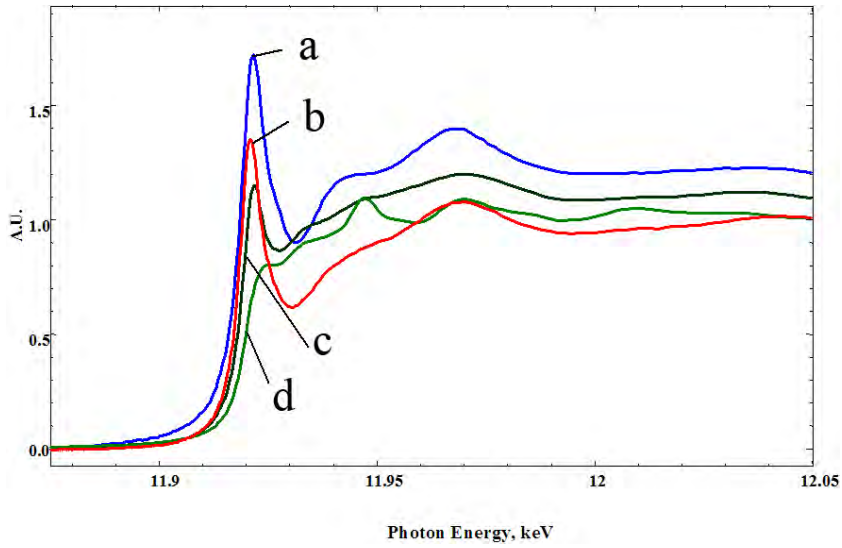

Figure 3.9. AXANES spectra of Au coumpounds : (a) Au^{3+} acetate, (b) as-prepared Au/γ-Al2O3 catalyst, (c) Au^{+}Cl, (d) Au foil.

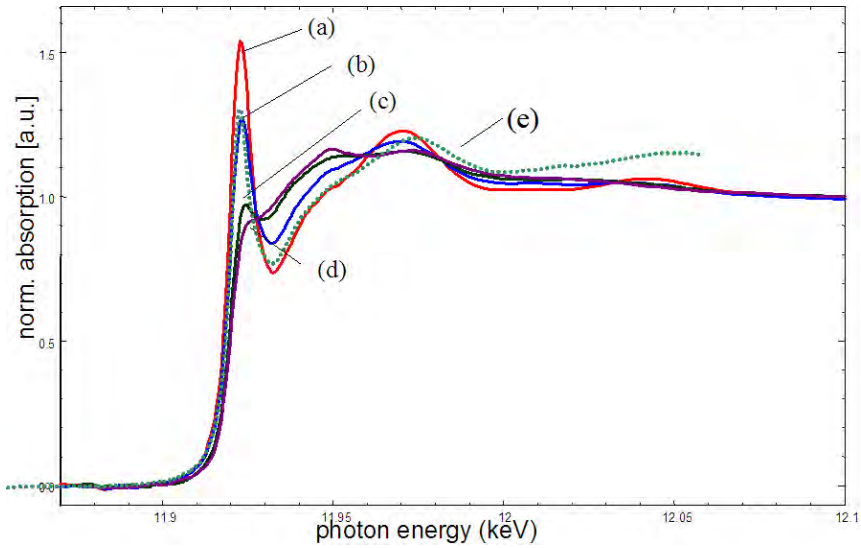

Figure 3.10. XANES characterizing 1.3wt% Au/γ-Al_2O_3(DP): (a) as prepared uncalcined, (b) after 30 min in H_2 at 100℃, (c) after subsequent treatment in H_2O and H_2 at 100℃ for 30 min, (d) after an additional 30 min in H_2 and H_2O at 100℃. (e) another sample after treatment in H_2O and H_2 at 100℃ for 2 h.

occurred. This sample was only barely active for CO oxidation. XANES spectra of the highly active samples are shown in Figures 3.10c and 3.10d, which were collected after treatment at 100℃ in H_2 for 30 min followed by H_2 saturated with water for 30 and 60 min, respectively. Compared to Figure 3.10b, these samples were much more severely reduced, and the sample shown in Figure 3.10d was more reduced than the sample in Figure 3.10c. The majority of the Au in these samples were metallic, and the pseudo steady state activity was reached. Thus, once the catalyst had been reduced to a certain point, further reduction did not improve its activity significantly. Interestingly, Figure 3.10e shows that the Au species was not as reduced after an as prepared catalyst was treated in H_2 and H_2O at 100℃ for 2 hours.

3.3.3. Conclusions

As described above, gold species in Au/Al_2O_3 was almost fully reduced after activation (after 30 min in H_2 at 100℃ and subsequent treatment in H_2O and H_2 at 100℃ for 30 min). The catalyst was highly active without any noticeable change of the Au particle size. Furthermore, a large number of isolated atoms and gold clusters are shown in STEM images on the active catalyst. These species were inferred to be metallic from the XAS data, and should be very active. Although it is too early to say that they actually account for the activities of activated catalysts, they certainly play a big role in the catalytic properties of the Au/Al_2O_3 catalysts.

In the case of Au/Al_2O_3 system, the agglomeration of gold atoms was confined by their mobility on the Al_2O_3 surface.

3.4. Activation of Au/TiO_2 Catalysts for CO Oxidation

3.4.1. Objective and experiments

In addition to Au/Al_2O_3 , Au/TiO_2 is another very active catalytic system for CO oxidation at room temperature. The catalysts were prepared by the deposition precipitation method described earlier. Different from the Au/Al_2O_3 catalysts, no additional activation process is needed since the Au/TiO_2 catalysts can be reduced instantaneously at room temperature by CO or H_2. However, the relative importance of the two factors, size and chemical state of gold particles, to the activity still needs to be elucidated. Since the degree of reduction can be controlled by precisely measuring the amount of reduction gas, it would be possible to monitor the change of catalytic properties at each stage of reduction. Therefore, the relationship among the average Au oxidation state, Au metal cluster size, and catalytic activity during the activation process could also be obtained.

In this study, H_2 pulses were used to gradually reduce the Au/TiO_2 catalysts at 195K. H_2 consumption of each pulse was taken as an indicator for the degree of reduction. Gold particle size was examined by TEM and EXAFS, oxidation state was checked by XPS and XANES, and at each stage, the activity for CO oxidation was recorded.

3.4.2. Results and discussion

3.4.2.1. Change of particle size during activation of Au/TiO_2. Au/TiO_2 catalysts exhibit the same particle size increase as Au/Al_2O_3 catalysts after calcination (Figure 3.11c). The difference between these two catalysts is that after reduction of the Au/TiO_2 catalysts, an increase in particle size can be easily noticed. It might be explained that gold particles have higher mobility on the TiO_2 surface than on Al_2O_3 surface. After reduction,

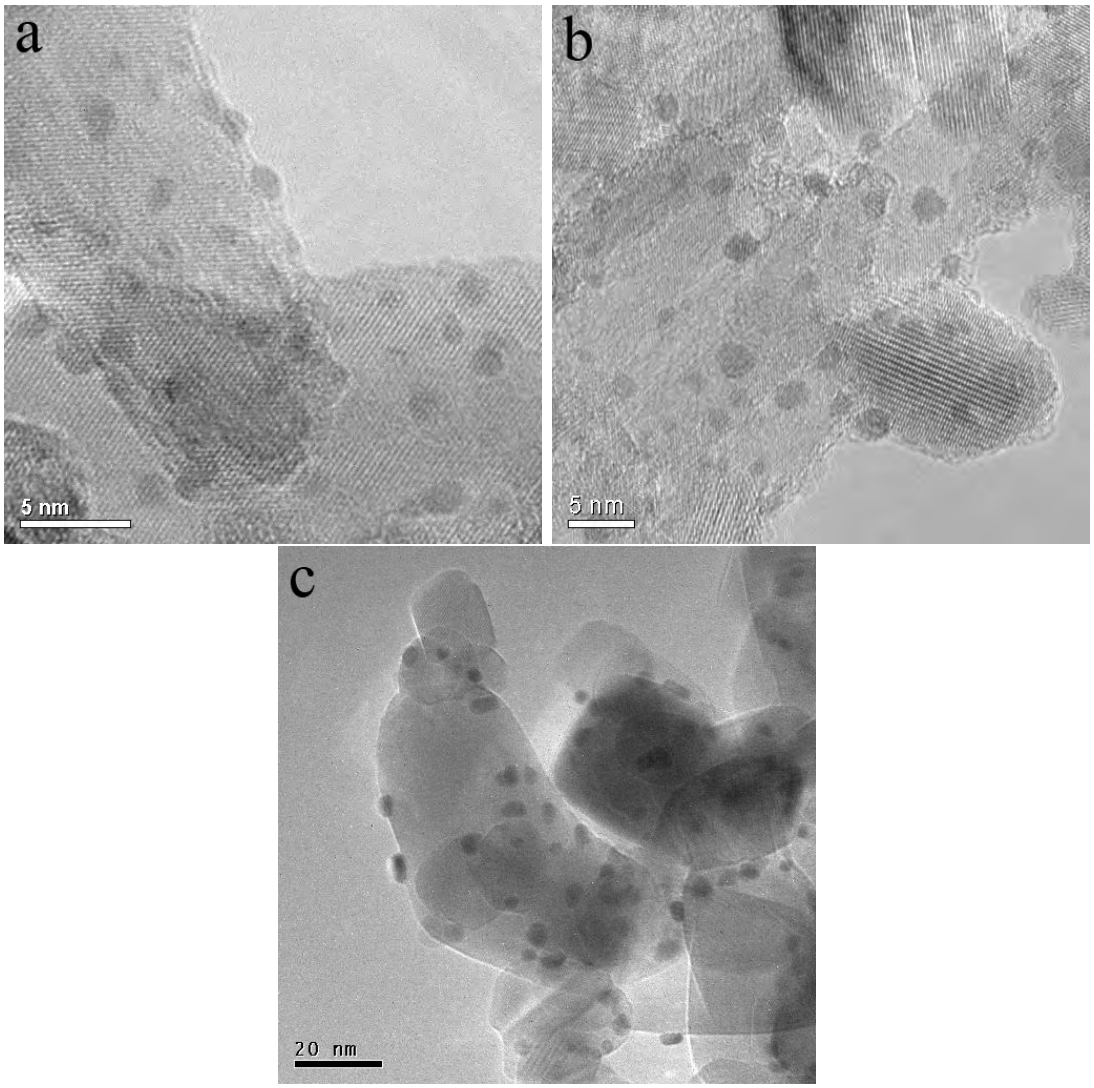

Figure 3.11. TEM images of Au/TiO_2 after various treatments: (a) uncalcined (as prepared); (b) reduced by H_2 at room temperature; (c) calcined in air at 350℃ for 4 hours.

gold atoms agglomerated to form larger particles, which infers that fewer isolated atoms are expected, and gold clusters and more well faceted particles should be found in the catalysts. The STEM study of activated Au/TiO_2 catalysts, indeed shows no isolated gold atoms (Figure 3.12a) on the surface; large gold atom agglomerates are formed instead.

Different from the crystals, they are not all well crystallized , and in some cases, loose clusters are attached on the surface of the agglomerates. In another part of the same catalyst (Figure 3.12b), well faceted and stable gold nanoparticles are seen. In some well aligned particles, lattice fringes can be readily identified.

An EXAFS spectrum was taken between each H_2 pulse. Figure 3.13 shows the magnitude of the Fourier transformed, k^2-weighted χ function of selected EXAFS spectra in R-space. The positions corresponding to Au-O and Au-Au scatterings are indicated by arrows. The magnitude of the transform due to the Au-O scattering barely decreased from pulse 1 to pulse 5, and then much more rapidly, particularly between pulse 8 and 14. After pulse 15, there was little Au-O scattering. In contrast, there was little Au-Au scattering until pulse 9. The Au-Au scattering then increased, reaching a maximum value at pulse 16. At this point, assuming hemispherical particles, the coordination number (CN) of about 6 corresponded to a particle of about 1 nm. This implies that Au particles agglomerate as the sample is reduced.

3.4.2.2. Change of oxidation state during activation of Au/TiO_2. As a fast and widely available technique, XPS has been used routinely to check the chemical states of Au species at different stages of reaction/treatment. Although not a very good method for analyzing chemical composition, XPS is very sensitive to the chemical state of gold, e.g. Figure 3.14. Au/TiO_2 catalysts were treated by H_2 in this case. XPS was carried out on samples at different reduction states, then the spectra were compared to a spectrum from a reference Au/TiO_2 (calcined) distributed by the World Gold Council (WGC). The Au 4f peak positions for uncalcined samples agree well with what was reported in literature (Park and Lee 1999) for Au^{3+} compounds. A shift of 2.5eV in Au 4f binding energy was

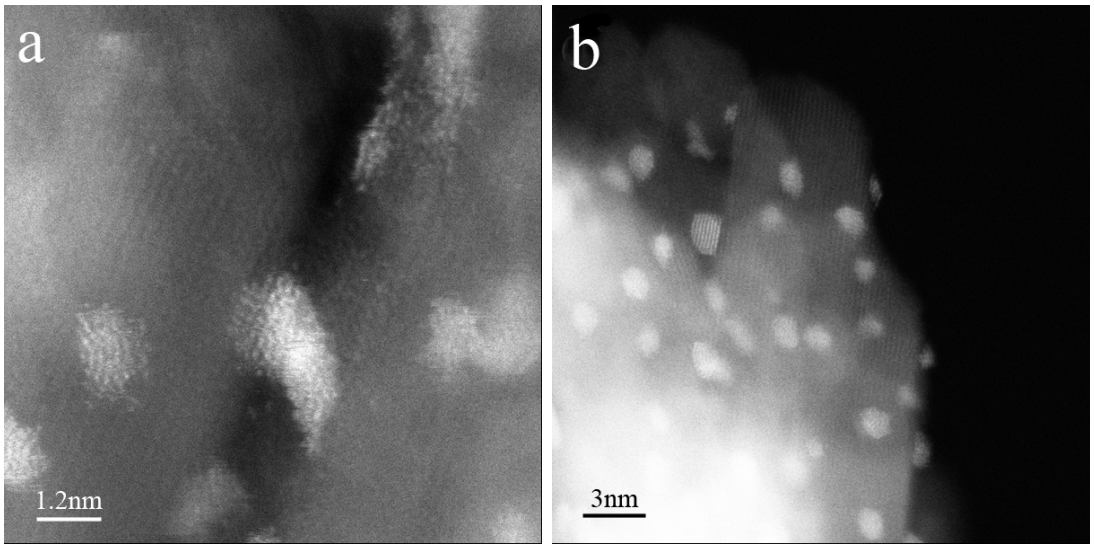

Figure 3.12. TiO_2 catalyst after CO activation at room temperature: (a) gold atom clusters; (b) well faceted gold nanoparticles.

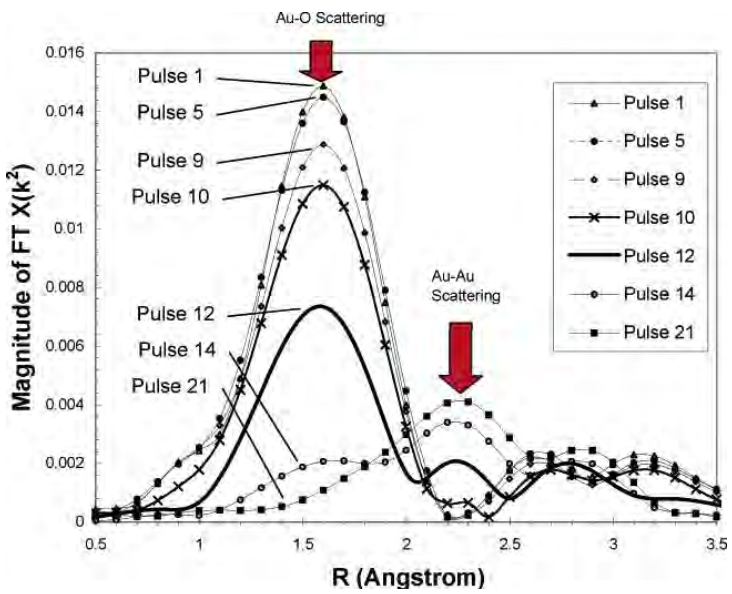

Figure 3.13. Magnitude of the Fourier transformed $k^2 2$-χfunction in R-space of Au/TiO_2 after selected H_2 pulse. The arrows indicate positions of Au-O and Au-Au scattering at 1.6 and 2.3 Å in R space.

clearly shown between uncalcined (oxidized) and calcined (reduced) samples. For the 50% reduced sample, the Au 4f peaks were broader, and the maxima appeared in between the

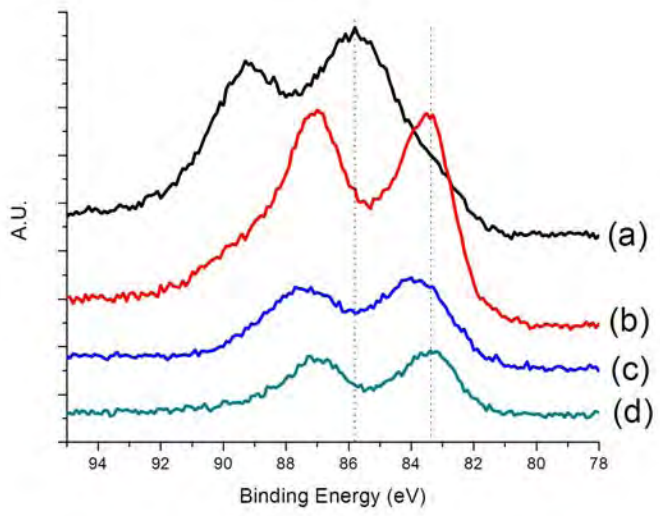

Figure 3.14. Au (4f) binding energy of Au/TiO_2 catalyst: (a) as-prepared sample; (b) sample fully reduced by H_2 pulses; (c) sample 50% reduced by H_2 pulses; and (d) reference Au/TiO_2 catalyst (calcined) distributed by WGC.

other two samples, which is expectated if a mixture of Au oxidation states was present. The oxidation state of the 50% reduced sample was independently determined by XAS measurement (data not shown). With the use of a linear combination of Au^{3+} and Au^0 XANES spectra, the percentage of Au^{3+} being reduced was confirmed.

The reduction of Au^{3+} species by H_2 pulses at 295 K was also monitored by XAS. The spectrum of the as-prepared sample showed an intense white line at the Au LIII edge, typical of supported Au^{3+} species. Within experimental uncertainties, the intensity of the white line remained unchanged for the first 5 pulses, and began to decrease afterward, indicating detectable reduction of Au^{3+} to Au_0. By using a linear combination of XANES spectra of Au3+ and Au0 reference compounds, the percentage of Au^{3+} and Au^0 in the sample was determined. The decrease in the percentage of Au^{3+} after each pulse is shown

in Figure 3.15. The curve in 3.15 showed a trend as : an induction period followed by increasingly faster and then decreasing reduction rate.

3.4.3. Conclusions

The relationship between particle size and catalytic properties can be demonstrated by Figure 3.16, where the coordination number of Au can be obtained simultaneously with the catalytic properties. With the increase of the gold particle size, the activity of the catalyst lagged behind. An induction period was then proposed when gold nanoparticles grew but are not activated to CO oxidation.

Therefore, the picture of the activation of a Au/TiO_2 catalyst by H_2 pulse has emerged from this study and becomes clear. The process was found to begin with an induction period when ionic gold species agglomerate, but remain oxidized. The catalysts are not activated and there is no consumption of H_2. After reaching a critical point, H_2 started to decompose gold agglomerates, H_2 consumption starts. If the activity is tested at this moment, it will increase with the extent of reduction until gold particles with an average diameter of 1 to 1.5 nm are obtained. Form this point, further reduction only increases the size of gold particles. The high mobility of gold species on TiO_2 surface is the key to this mechanism. For example, if similar experimental method is applied to Au/Al_2O_3 catalysts, most likely, the induction period won't be observed.

3.5. Conclusions

In this chapter, the studies on oxide supported Au catalysts by electron microscopy and other techniques were presented. The size, structure, morphology and chemical states

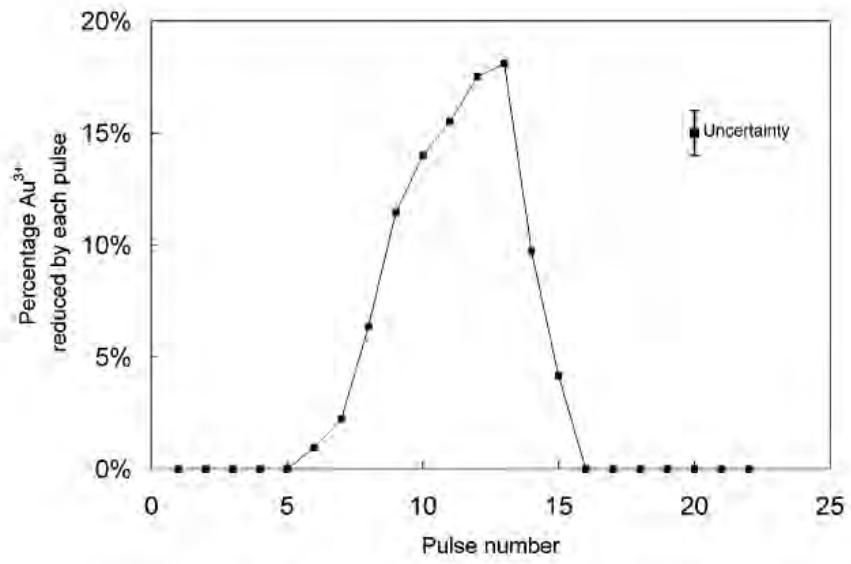

Figure 3.15. Activity and gold particle size change with time on stream. Temperature: -68℃; reaction gases: CO 1%, O_2: 2.5%, balanced by He at 1atm; ananlyzed and graphed by J.H. Yang

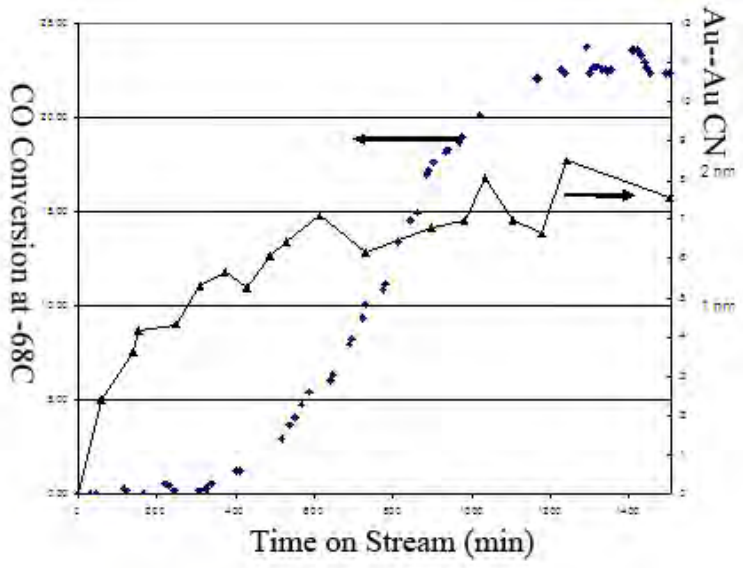

Figure 3.16. Activity and gold particle size change with time on stream. Temperature: -68℃; reaction gases: CO 1%, O_2: 2.5%, balanced by He at 1atm; ananlyzed and graphed by J.H. Yang

of gold particles were investigated. Accordingly, the effects of chlorine on the activation and the activity of the supported Au catalysts, Au/Al_2O_3 and Au/TiO_2, were discussed. Some questions were answered, but some still remain unclear.

The research on the effects preparation methods on catalytic properties revealed the dual role of Cl^- in suppressing the CO oxidation activity of a Au/Al_2O_3 catalyst: accelerating the agglomeration of gold particles and poisoning the active sites. Considering the fact that only a small amount of Cl^- was needed for poisoning and the amount of residual Cl^- on the catalyst is decided by the pH value during deposition-precipitation and the rinsing afterwords, one can draw the conclusion that this certainly is one of the reasons why the activity of a Au catalyst is so sensitive to the preparation condition. The research on the activation of Au/Al_2O_3 and Au/TiO_2 catalysts demonstrated that the oxidation state and the size of the gold particles were two important factors on the final catalytic activity. The difference in the mobility of gold species on oxide surfaces affects them. Au/Al_2O_3 catalysts were not as easily activated as Au/TiO_2 catalysts. Gold atoms and/or ions have low mobility on the Al_2O_3 surfaces. The agglomeration of them was confined by their mobility on the Al_2O_3 surface. Since the size of gold particles tends to remain constant during activation, the oxidation state of gold species can be used as an indicator for the activities of the catalysts. In the case of Au/TiO_2, gold has a higher mobility on TiO_2. Both the reduction of ionic gold and the growth of gold particles are fast during the activation. And the induction period suggests that ionic gold species agglomerate before being reduced.

A number of questions remain, which include how the surface of support looks like, how gold nanoparticles grow on surface, and how treatments exactly change the size and

morphology of gold nanoparticles, etc.. A thorough investigation of oxide surfaces and model catalysts is needed to even come close to answer these questions. In the following chapters, a study of TiO_2 surface and Au/TiO_2 catalyst were carried out for that purpose.

CHAPTER 4

Studies on TiO_2 (100) surface

4.1. Introduction

As a commonly used catalyst support and substrate for studies of thin films, rutile TiO_2 has been the subject of active investigation for decades. Various methods have been employed in order to gain a fundamental insight into its surface properties and to understand and improve the performance of TiO_2-related materials and devices. However, in the past decades, the main driving force for surface investigations of TiO_2 has been to understand and improve catalytic reactions, since most heterogeneous catalysts system consist of small metal clusters on an oxide support. As a simple system, a metal/TiO_2 system often serves as a model for other metal/oxide surfaces. At the same time, the recent discovery that finely dispersed Au particles supported on TiO_2, as well as other reducible metal oxides oxidize CO at low temperatures (Haruta et al. 1987) has made the Au/TiO_2 system a very promising catalytic system and further increased the interest in the surface science community.

The local environment of the TiO_2 surface is very important to understand Au/TiO_2 system. The most well known example is the so-called strong metal support interaction (SMSI) (Horsley 1979), which has long been accepted as one of the major factors influencing catalytic properties. The extremely small dimensions of the gold particles not only cause changes in the electronic structure due to quantum size effects, but also makes

it possible for SMSI to extend its influence to the whole single particle. On the other hand, oxygen vacancies at the TiO_2 surface act as active sites for gold particle nucleation (Wahlstrom et al. 2003) on the TiO_2 surface and considering the role oxygen vacancies play in the process of water dissociation (Salvador 1992; Schaub and Thostrup 2003; Brooks et al. 2001) and gas sensing for oxygen (Sheveglieri 1992), they can be expected to be deeply involved in the catalytic process (Harber and Nowak 1999; Xu et al. 1995; Gao et al. 1996). In order to fully comprehend the nature of Au/TiO_2 interaction, it seems natural to start with the TiO_2 surface.

TiO_2 crystallizes in three major different structures: rutile, anatase and brookite. However, only rutile and anatase play any role in applications and are of any interest for surface scientists. In this study, only rutile (tetragonal, $D^1 4_4 h$-$P4_2$/amd, a=b=4.584Å, c=2.953Å(Grant 1959)) was used, either in powder form for real catalyst experiments, or single crystal form for model catalyst studies. Specifically, one of its low indexed stable surface, (100), was selected for this study due to its simplicity and relatively lesser amount of research attention received than the (110) surface.

According to the rules of auto-compensation and the creation of non-polar surfaces (Tasker 1970; LaFemina 1994), a straightforward prediction of the stable surface termination can be obtained (Figure 4.1). It is a strongly corrugated surface, with rows of bridging oxygen atoms at the outermost layer, forming (010) oriented ridges. After sputtering and annealing, a (1x1) terminated LEED pattern is observed on this surface, and STM and non-contact AFM images (Raza et al. 1999a,b) are consistent with the proposed model. However, the process of how the surface recovers to (1x1) after annealing

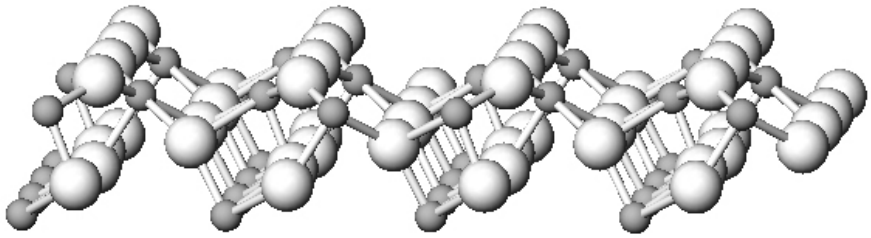

Figure 4.1. Ball and stick model of rutile TiO_2 (100) surface. Ti: filled sphere O: open sphere

and the accompanying defect structures are the real interests of this study, because all of the catalytic properties of the TiO_2 surface are related to defects on the surface.

The titanium-oxygen phase diagram is very rich with many stable phases with a variety of crystal structures (Samsonov 1982). Consequently, rutile is easily reduced , either by irradiation or by annealing in reducing condition(Samsonov 1982), and different reduction and oxidation treatments yield significantly different surfaces (Diebold 2003). A large amount of work has focused on the (110) surface by several groups (Onishi and b 1996; Onishi and a 1994; Blanchin and Bursill 1984; Anderson and Hyde 1967; Li et al. 1999). Using scanning tunneling microscopy (STM), a number of reconstructions and surface features have been identified (Onishi and b 1996), including, under certain conditions, ad-atom rows of Ti_2O_3 (Onishi and a 1994), shear-planes (Blanchin and Bursill 1984; Anderson and Hyde 1967) and so-called "rosettes": sub-stoichiometric, quasi-hexagonal overlayer islands (Li et al. 1999). Principal variables in the formation of these structures appear to be the oxygen partial pressure and temperature during the annealing treatment. However, experimental studies of the rutile (100) surface thus far have been primarily carried out under ultra high vacuum (UHV) using STM (Murry et al. 1994; Raza et al. 1999b), low energy electron diffraction (LEED) (Guo et al. 1996), surface

X-ray diffraction (SXRD) (Zajonz et al. 1998), and grazing incidence X-ray diffraction (GIXD) combined with direct methods (DM) (Landree et al. 1998). The process of reduction and re-oxidation of this surface has been thoroughly studied, and different models for the (1x3) surface reconstruction have been proposed. In this study, attention was paid to the surface recovery process of the reduced TiO_2 (100) surface. Since Au/TiO_2 real catalysts perform CO oxidation at room temperature, it is more relevant and justifiable to study the surface annealed under oxidizing conditions and stable in air.

In this chapter, the results from TEM studies of the TiO_2 (100) surface annealed under oxidizing conditions are presented. The surface morphology evolution with annealing temperature and time are described. Finally, the surface re-oxidation process during annealing is explained.

4.2. Sample Preparation and Characterization

Single crystal TiO_2 (100) TEM samples were prepared as described in Chapter 2. Samples were then subjected to the various annealing treatments listed in Table 4.1 in a tube furnace. The alumina boat and the quartz tube used for the anneals were thoroughly cleaned in nitric acid prior to every annealing experiment. XPS was used to check the cleanliness before and after anneals (Figure 4.2). Other than a trace amount of carbon, no impurities were detected on the sample surface.

There is overwhelming spectroscopic and chemical evidence for the presence of point defects on the surface of samples sputtered and annealed in UHV. These defects are attributed to vacancies in the bridging oxygen rows. In this study, the last sample thinning process before annealing is ion-milling, basically a severely intensive Ar^+ ion sputtering.

Table 4.1. Parameters used in annealing experiments

Sample Number	Temperature (℃)	Time (Hour)	Gas (1 atm)	Notes
1	750	1	O_2	No c(2x2)
2	800	1	O_2	c(2x2)
3	900	1	O_2	No c(2x2)
4	750	2	O_2	c(2x2)
5	800	1	Ar	c(2x2)
6	830	6	O_2	No c(2x2)

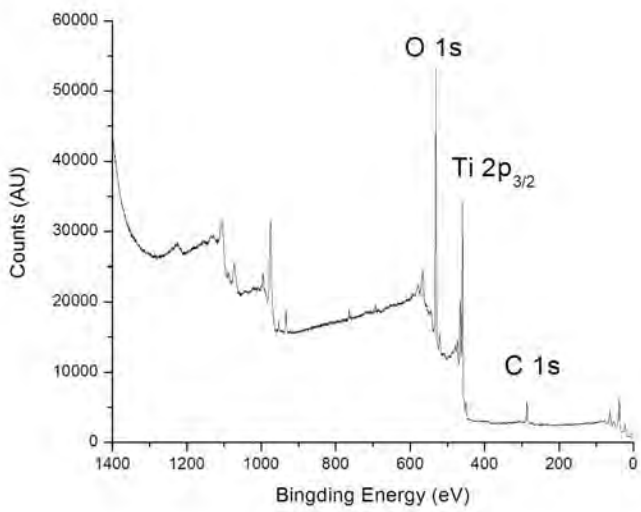

Figure 4.2. XPS spectrum of TiO_2 (100) TEM sample after anneals

Oxygen vacancies were readily created, as TiO_2 is the classic example for a maximum-valency compound material where electron-stimulated desorption occurs via the Knotek-Feibelman process (Knotek and Feibelman 1979). XPS was also used to investigate oxygen vacancies on the surface, since these imperfections introduce changes in the electronic structure. In particular, oxygen vacancies lead to the development of a shoulder in the XPS Ti2P peak, which is formally assigned to a Ti^{+3} oxidation state, and a band gap feature at 0.8eV below E_{Fermi}, which was produced by increased free electrons in the

valance band. The shoulder in the XPS Ti2P peak was observed to be broadened in Figure 4.3 due to preferential sputtering of oxygen from the surface. The electron density change in the valence band was demonstrated by the extra peak shown on the shoulder of LMV Auger peak low kinetic energy end of the spectrum in Figure 4.3.

TiO_2 bulk defects play a major role in a variety of surface phenomena where annealing to high temperatures is necessary, e.g. in bulk-assisted reoxidation (Henderson 1999, 1995) and in restructuring and reconstruction processes (Li et al. 1999; Bennett et al. 1999). The bulk structure of reduced TiO_{2-x} crystals is quite complex with various types of defects such as doubly charged oxygen vacancies, Ti^{+3} and Ti^{+4} interstitials, and planar defects such as crystallographic shear planes (CSP). The question of which type of defect is dominant in which region of oxygen deficiency is still a subject of debate (Kofstad 1967). As to the diffusion mechanism, it is quite different for the various types of defects: oxygen migrates via a site exchange (vacancy diffusion) mechanism, while excess Ti diffuses through the open channels along the crystallographic *c*-axis (Huntington and Sullivan 1965). Consequently, the diffusing species in oxidation reactions of reduced TiO_2 is the Ti atom and not the O vacancy (Henderson 1999, 1995).

4.3. Surface Morphology

4.3.1. Rutile TiO_2 (100) surface evolution with temperature

To ensure a common reference point, all samples were ion milled to disorder the surface prior to annealing. Due to the differences in the relative sputtering rates of titanium and oxygen(Mens and Gijzeman 1996; Knotek and Feibelman 1979), ion milling produces samples that are oxygen deficient on the surface. In the bright field TEM image from this

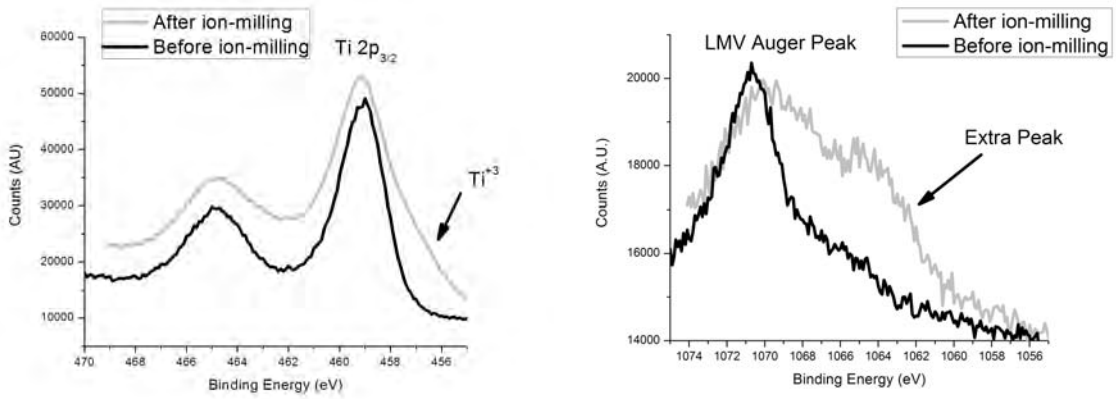

Figure 4.3. XPS spectrum of TiO_2 (100) TEM sample before and after ion-milling: (a) Ti $3p_{3/2}$ peak; (b) LMV Auger peak

sample (Figure 4.4), thickness fringes and bend contours are the two dominant features. The former is a direct result of the sample preparation technique employed, which produces wedge-shaped region around the hole (with thickness increasing into the sample), and the latter is from the strain resulting from ion bombardment. The diffraction pattern (DP) (Figure 4.4) shows only the bulk (100) diffraction spots and diffuse diffraction (indicated by arrows) from ordered defects on surface.

Images and diffraction patterns from samples after various treatments are shown in Figure 4.5-4.7. Annealing resulted in the formation of extended faceting with flat (100) terraces separated by step bunches in order to reduce surface energy. Step edges composed of (010) and (001) planes readily formed on samples annealed at 750℃ for 1 hour (Figure 4.5). The width of the terraces along the [010] direction is much smaller compared to that along [001] direction, which results in streaks along the [010] direction in the DP. Rutile TiO_2 has a tetragonal structure with different surfaces exposed on (010) and (001). This anisotropy is clearly demonstrated in the images and DPs of annealed samples.

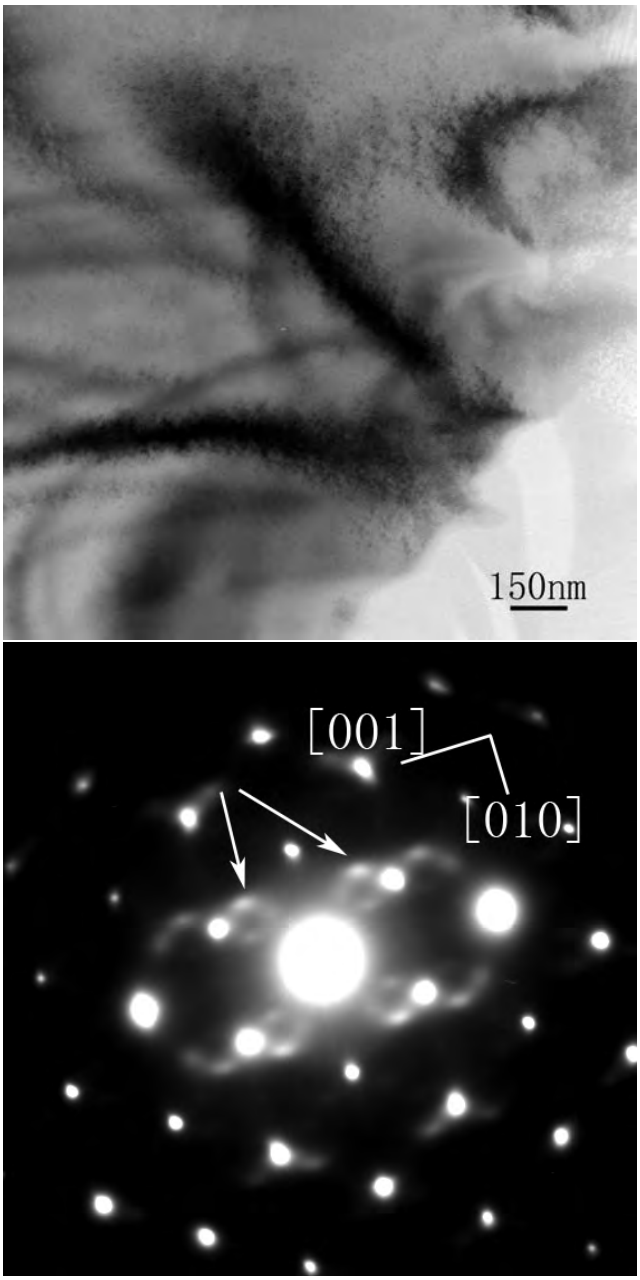

Figure 4.4. Rutile TiO_2 (100) surface evolution with temperature. After ion milling sample, bright field image with DP.

For samples annealed at 800℃, the width of surface terraces became noticeably larger, which led to the disappearance of streaks along the [010] direction in the DP(Figure 4.6).

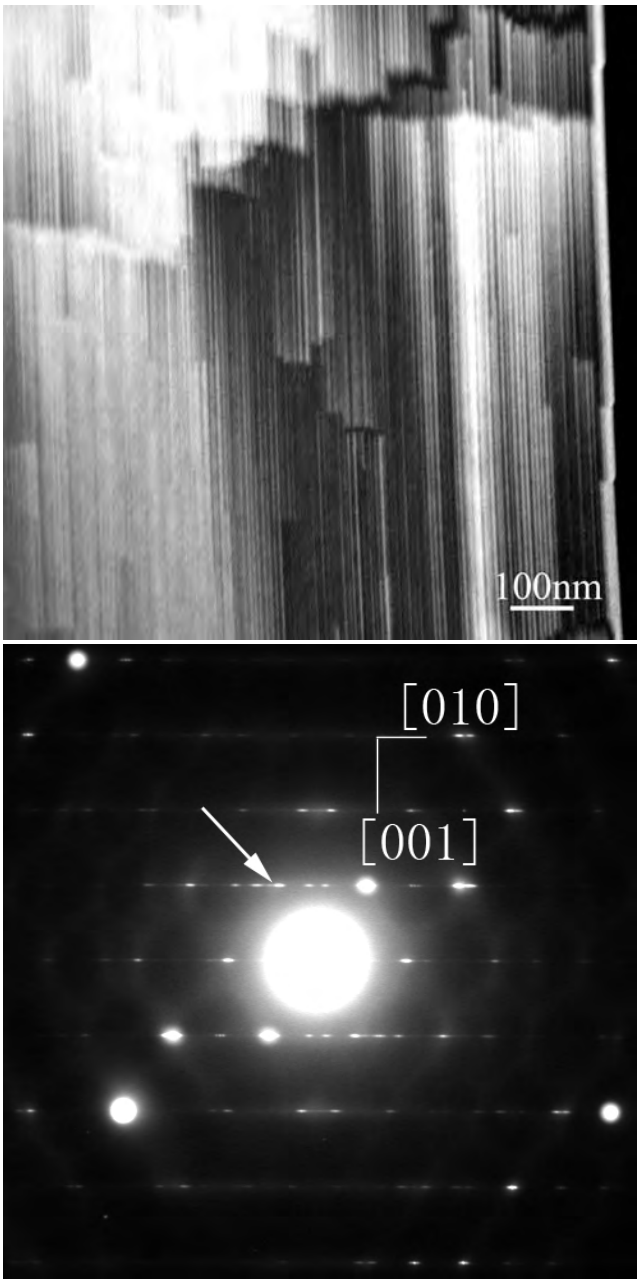

Figure 4.5. Rutile TiO_2 (100) surface evolution with temperature. 750℃ 1 hour in O_2, dark field image with DP.

At the same time, low index faces, (001) and (010), formed at the edge of the sample, which are indicated in the dark field image. The faceting of the sample edge was observed

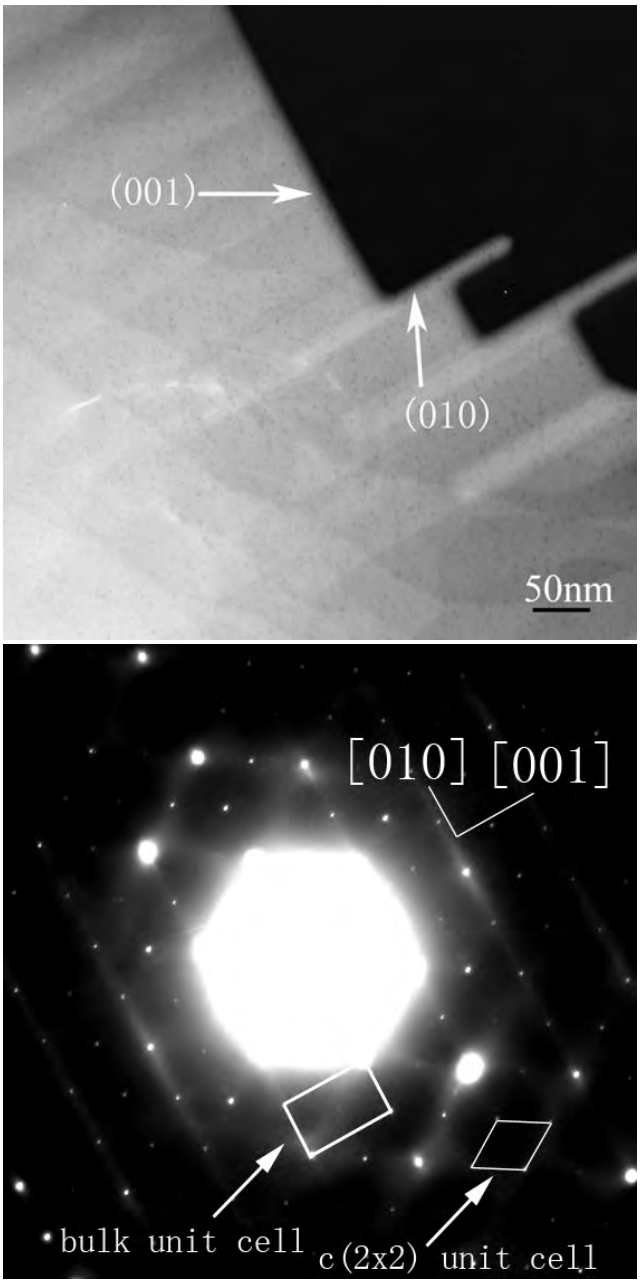

Figure 4.6. Rutile TiO_2 (100) surface evolution with temperature. 800℃ 1 hour in O_2, dark field image with DP.

in all the samples annealed and can be used as a measure to judge the amount of surface diffusion. In all the samples studied thus far, there is a positive correlation between

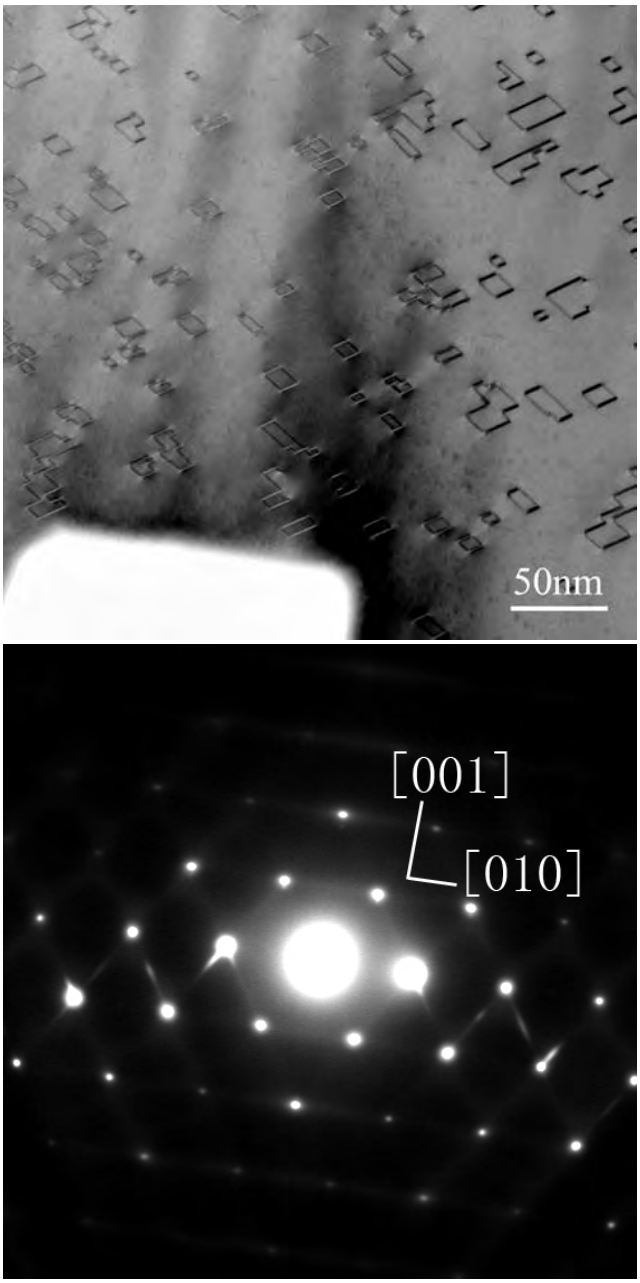

Figure 4.7. Rutile TiO_2 (100) surface evolution with temperature. 900℃ 1 hour in O_2, dark field image with DP.

faceting of the edge and degree of surface ordering. The most important observation on samples annealed at 800℃ is the c(2x2) surface reconstruction observed in the DP. This

was the first observation of this reconstruction on the rutile (100) surface, and the DP unit cell for the surface reconstruction and bulk TiO_2 are outlined in Fig. 1c. The formation and structure of this surface reconstruction will be discussed later.

After annealing at 900℃ for an hour, the surface became flat and c(2x2) diffraction spots were not present. However in part of the sample where ion-milling damage was severe, straight defects were observed parallel to the (011) plane (Figure 4.7). These defects were formed by in-plane pure shear, which is common in the rutile-type structure. In this case, annealing did not fully restore the surface stoichiometry but instead made oxygen vacancies coalesce to form (011) type shear structures. The corresponding DP (Figure 4.7) shows two sets of diffuse streaks confirming the presence of ordered defects.

4.3.2. Rutile TiO_2 (100) surface evolution with annealing time and annealing environment.

Longer annealing time did not affect the general morphology of the surface given an annealing temperature. Flat and well oriented terraces and low index faces at the edge were still the main features observed. However the surface structures were completely different from those observed after shorter annealing time. Figure 4.8 shows the sample after 2 hours of O_2 annealing at 750℃. Not only have the streaks along [010] direction disappeared (compare to Figure 4.9), but also c(2x2) spots were clearly visible. On the contrary, after annealing at 830℃ for 6 hours, the DP (Figure 4.9) shows only clear TiO_2 bulk spots, instead of c(2x2). It seems that c(2x2) surface reconstruction only develops between a small temperature and time window. The implications of this will be discussed later.

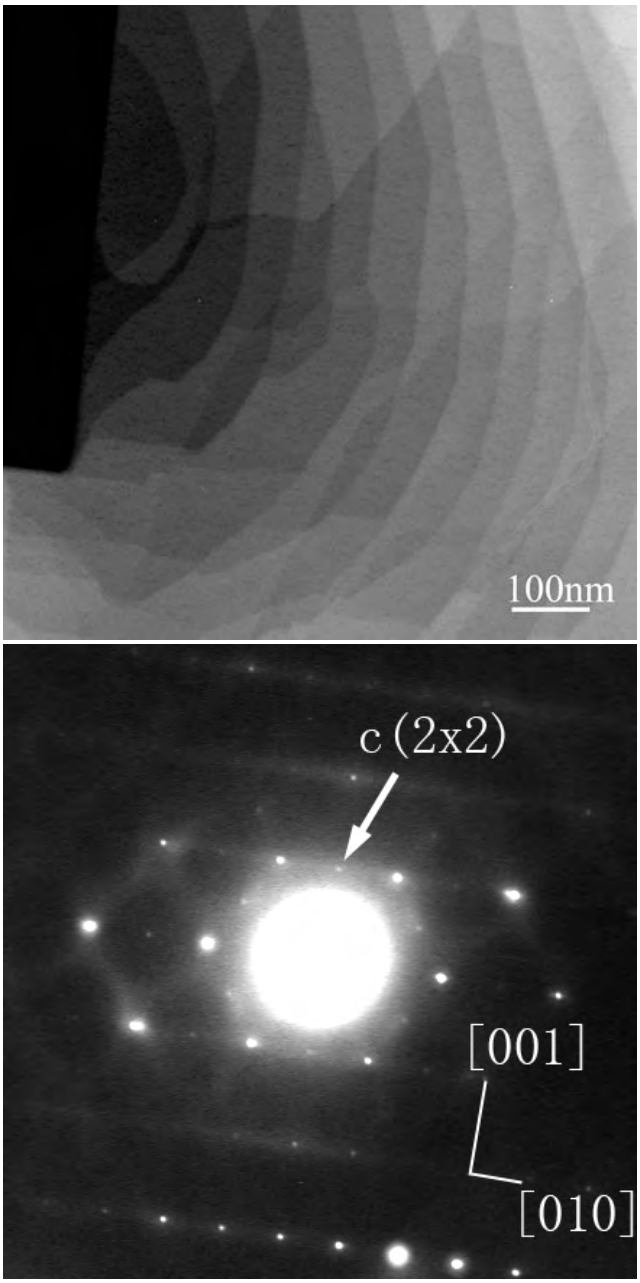

Figure 4.8. Effects of time and annealing environment on rutile TiO_2 (100) surface. 750℃ 2 hours in O_2, dark field image with DP.

The effect of annealing environment was further studied by changing the annealing gas from O_2 to Ar. This annealing experiment was done within the "window" for c(2x2)

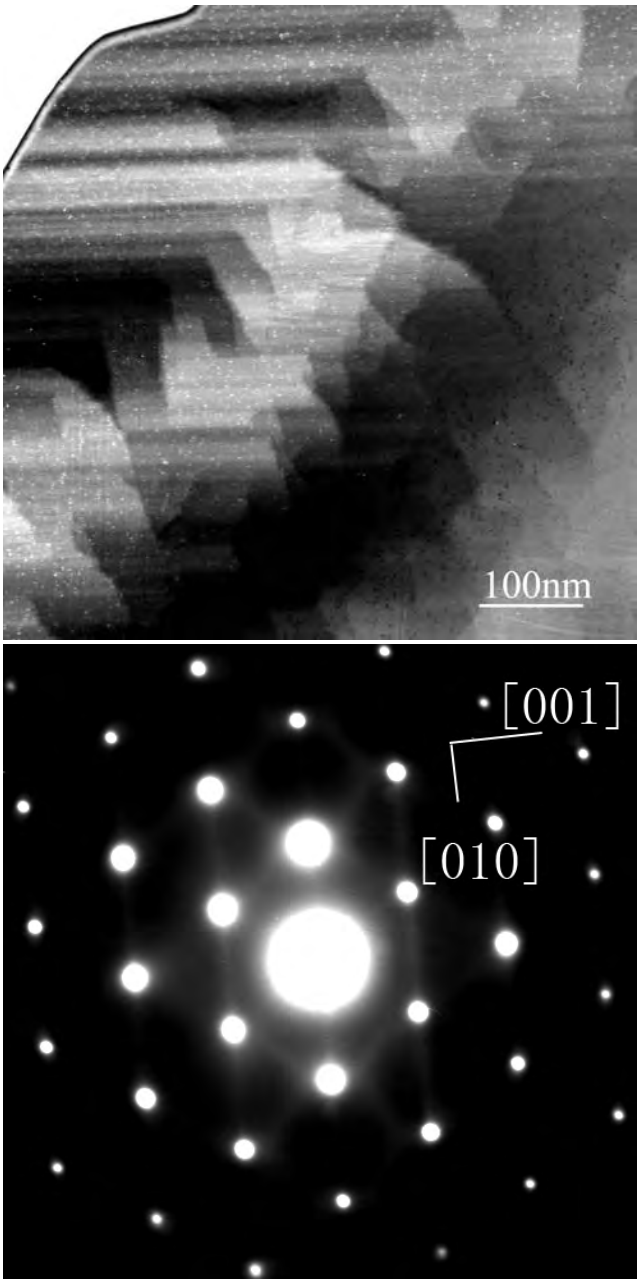

Figure 4.9. Effects of time and annealing environment on rutile TiO_2 (100) surface. 830℃ 6 hours in O_2, bright field image with DP.

formation. After anneals, the sample (Figure 4.10) showed the same morphology as samples annealed in O_2, and additionally the c(2x2) was observed. At first, this result

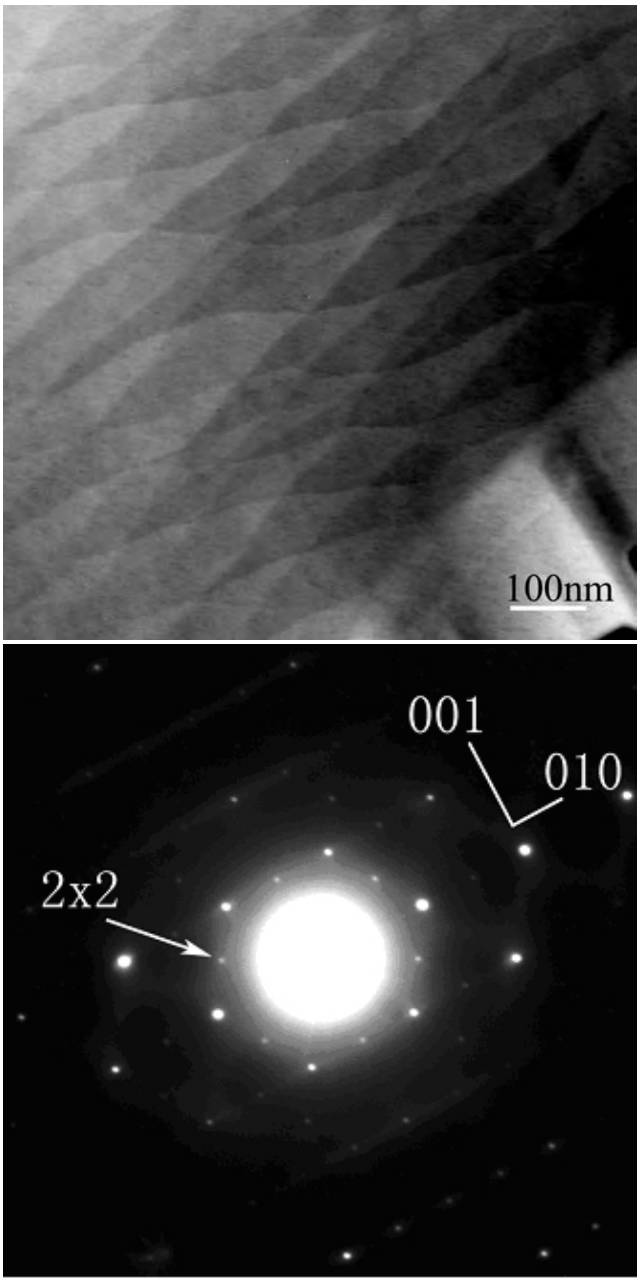

Figure 4.10. Effects of time and annealing environment on rutile TiO_2 (100) surface. 800℃ 1 hour in Ar, dark filed image with DP

seemed to be against the original thought of c(2x2) being an oxidization product. Until now, the c(2x2) was only observed after annealing in O_2 environments, and not in UHV,

indicating that the presence of O_2 in the gas phase was necessary for its formation. Therefore we consider the possibilities of oxygen impurities in the Ar feed gas, possible air leakage in the furnace seals and the effects of body assisted re-oxidation as sources for oxygen at the surface. We conclude that the partial pressure of gas phase oxygen required to form the c(2x2) might be lower than initially thought.

4.3.3. "Healing effects" of O_2 on rutile TiO_2 surface

For samples which had been ion-milled for a long period of time, annealing at 800℃ in O_2 for one hour sometimes could not completely recover the damaged surface. Fig. 3a shows a large number of small grains on the surface, which were proved to be Magnelli phases (DP not shown). Considering the phase diagram of the Ti-O system (Waldner and Eriksson 1999), it is understandable that while annealing in a high partial pressure of O_2, a deeply reduced surface would form Magnelli phases during re-oxidation. Annealing at 830℃ for 6 hours in O_2 entirely healed the reduced surface (Figure 4.11). Therefore, Figure 4.11 provides direct proof of the surface re-oxidation process during annealing.

4.3.4. Conclusions

The process of surface recovery from ion-mill damage was a process of surface re-oxidation and re-crystallization. Although the same process happens when reduced TiO_2 is annealed in vacuum, it seems to have a different mechanism due to a different annealing environment, which can be straightforwardly demonstrated by the color change of annealed samples. It is well established that the blue color in TiO_2 single crystals is associated with bulk defects which are formed upon reduction of the bulk (Cronemeyer 1952; Diebold

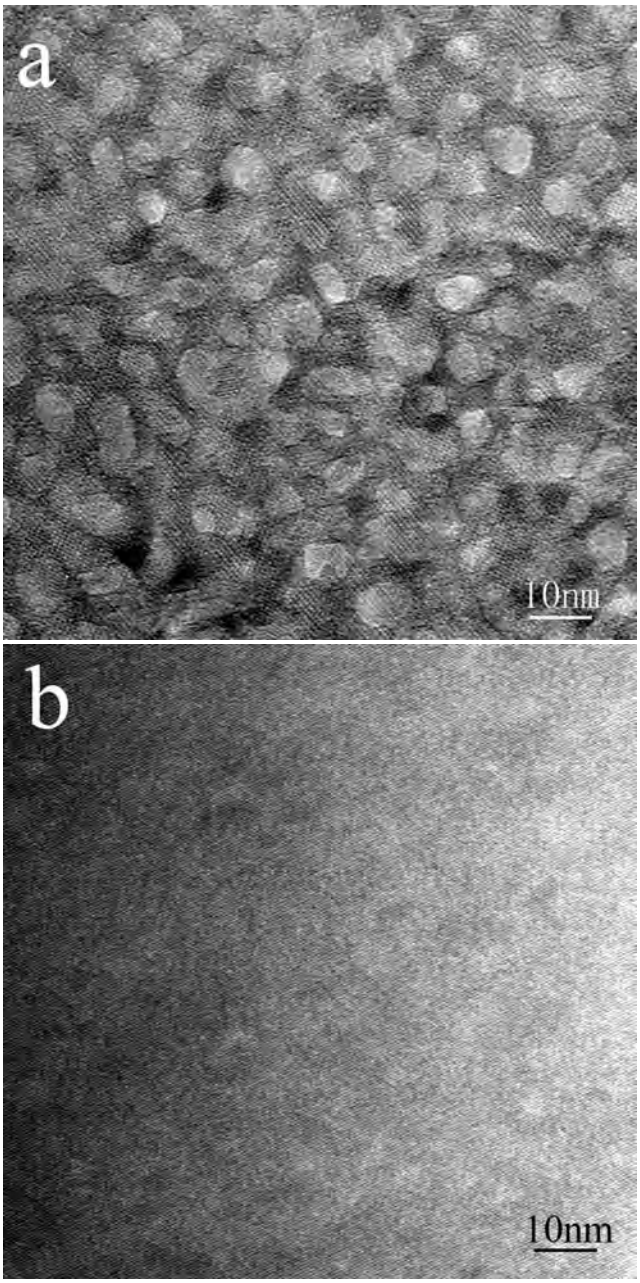

Figure 4.11. "Healing effects" of O_2 on rutile TiO_2 (100) surface: (a) 800℃ 1 hour in O_2; (b) 830℃ 6 hours in O_2 image.

et al. 2000) and the resulting color center. In previous studies, vacuum-annealing samples showed a (1x1) surface with the color of the bulk changing to various shade of blue,

implying the bulk TiO_2 was reduced. In this study, all samples were transparent after annealing, including the one treated in Ar, suggesting a decrease in the number of oxygen vacancies and Ti interstitials in the bulk. This difference in bulk structure is caused by the different oxygen partial pressure used during annealing and is strongly related to the formation of c(2x2) surface reconstruction, as discussed later.

Figure 4.4-4.11 show the effect of temperature and time on surface morphology during O_2 annealing. Before annealing, the sample is damaged and full of defects on the surface. Annealing treatments at 750℃ and above always resulted in the reduction of surface disorder and recovery of the surface crystallinity. Even after a short time of annealing, the disordered layer at the surface (Figure 4.4) was no longer present and the surface exhibited signs of flattening, terraces began to form and low index surfaces appeared at the profile edge of the sample. Higher annealing temperatures and longer annealing times generally correlated with larger terrace widths and fewer step bunches, characteristic of the synergistic role of temperature and time in diffusion controlled processes.

In all samples, the steps were entirely composed only of the (010) and (001) facets; (110) facets were not observed. The (100) terraces appeared in the form of long strips along [001] direction. Such anisotropic faceting behavior offers an insight into mechanism of formation and the atomic structure of the c(2x2) reconstruction, since c(2x2) might form right at the moment when small (100) terraces expand along [010] direction and atomic height steps disappear (Figure 4.5, 4.6 and 4.8).

The atomic structure and thermodynamics of a c(2x2) structure on the TiO_2 (rutile) (100) surface were studied using a combination of direct methods with transmission electron diffraction data and density functional calculations and will be talked about

later. Both experimental and theoretical work on this surface suggests that the surface is oxygen-deficient. This is a rather interesting observation, since the reconstruction was obtained by annealing in O_2 and is stable in air.

4.4. C(2x2) Surface Reconstruction

4.4.1. Formation of c(2x2) Surface Reconstruction

The c(2x2) reconstruction is obtained over a certain range of annealing temperatures and times. This study suggests that the small "window" condition for formation of c(2x2) is around 800℃ for about 1 hour in an environment where O_2 partial pressure in not very low (compared to UHV). Since it has never been observed in UHV surface re-oxidation studies, it is believed that the c(2x2) is introduced and stabilized by the presence of O_2 in the gas phase. O_2 partial pressure plays a crucial role in this process, although the c(2x2) itself is a structure with oxygen vacancies at the surface, which is proved by the fact that extended annealing in O_2, at higher temperatures or for longer times, results in the annihilation of the c(2x2) domains on the surface.

Previous studies on the rutile (100) surface have underscored the active role of oxygen vacancies in the surface reconstruction process. It was widely believed that oxygen vacancies obtained under reducing conditions would be inherently unstable when exposed to oxygen (Onishi and b 1996; Onishi and a 1994). In this study, it is found that the slightly reduced surface (even after annealing in O_2) is quite stable in air. Moreover the reconstruction can be reproducibly obtained by annealing under conditions usually considered reducing, i.e. annealing under flowing Ar at 800℃. The oxygen vacancies that stabilize the surface reconstruction are introduced in the ion milling stage of sample preparation,

and annealing primarily serves to provide the energy for ordering of these point defects. It seems that ion milling provides an alternative route to selectively reduce the surface, and the degree of reduction can be controlled by varying the time of sputtering.

It is natural to compare the c(2x2) reconstructed surface with other surface reconstructions on the same surface. The rutile (100) - (1x3) surface is reported to form after annealing at temperatures between 600-1000℃ in UHV environment (Lindan and Harrison 2001; Lo et al. 1978). Although the structure of this surface has not been determined conclusively, there is a general consensus that this surface is deeply oxygen deficient. The (1x3) surface was never observed in this study and we believe that this is due to the high partial pressures of O_2 employed during annealing. Most of our annealing experiments were carried out under an oxidizing environment. Even in the case of annealing in Ar, the oxygen partial pressure was much higher than the pressure in previous studies. The experimental evidence points to the conclusion that the (1x3) surface has a much higher concentration of oxygen vacancies than the c(2x2) surface. The c(2x2) forms when the oxygen deficient (100) surface is close to regaining its stoichiometry and this regime was not explored in the previous studies.

At the same time, on annealing experiments done in both oxygen and Ar, shear-planes indicative of the start of formation of the Magnelli phases (Bursill and Blanchin 1984; Kosuge 1994) were observed (Figure 4.12) in samples which were more reduced than those where the c(2x2) occurred. From the bulk phase diagram (Waldner and Eriksson 1999; Zador 1983) and previous studies on oxidation of rutile surfaces during UHV annealing, it can be concluded that the c(2x2) is formed on slightly reduced TiO_{2-x}, so in terms of

increasing reduction, it holds true that

$$1 \times 1 < c(2 \times 2) < Magnelli \quad Phases \tag{4.1}$$

In this following sections, the surface structure of c(2x2) TiO_2 (100) was presented. The DM refinement described in the chapter was done in collaboration with Dr. A.K. Subramanian and first principle density functional theory (DFT) calculations were carried out by Dr. O. Warschkow and Prof. L.D. Marks. The thermodynamics of this surface structure will be discussed.

4.4.2. DM Analysis of c(2x2)

Off zone axis electron diffraction patterns, necessary for surface diffraction data analysis were obtained using the Hitachi UHV-H9000 electron microscope operated at 300kV. Electron diffraction patterns with varying exposure times were recorded from the surface using the techniques detailed in Chapter 2. A thin region of the target surface was chosen to further avoid dynamical effects. The exposure series comprising 9 negatives with ascending exposure time was subsequently digitized to 8 bits using an optronics negative scanner. Care was taken to ensure that under the exposure conditions the microdensitometer is linear. The intensities of 411 surface reflections were measure using a cross-correlation technique from 830 raw measurements and weighted symmetry averaging resulted in 70 independent reflections in $c1m1$ plane group symmetry. These reflections were subjected to direct methods analysis, which solves the phase problem without the need for a structure guess. A different plane group ($c2mm$) was used too and both revealed similar solutions

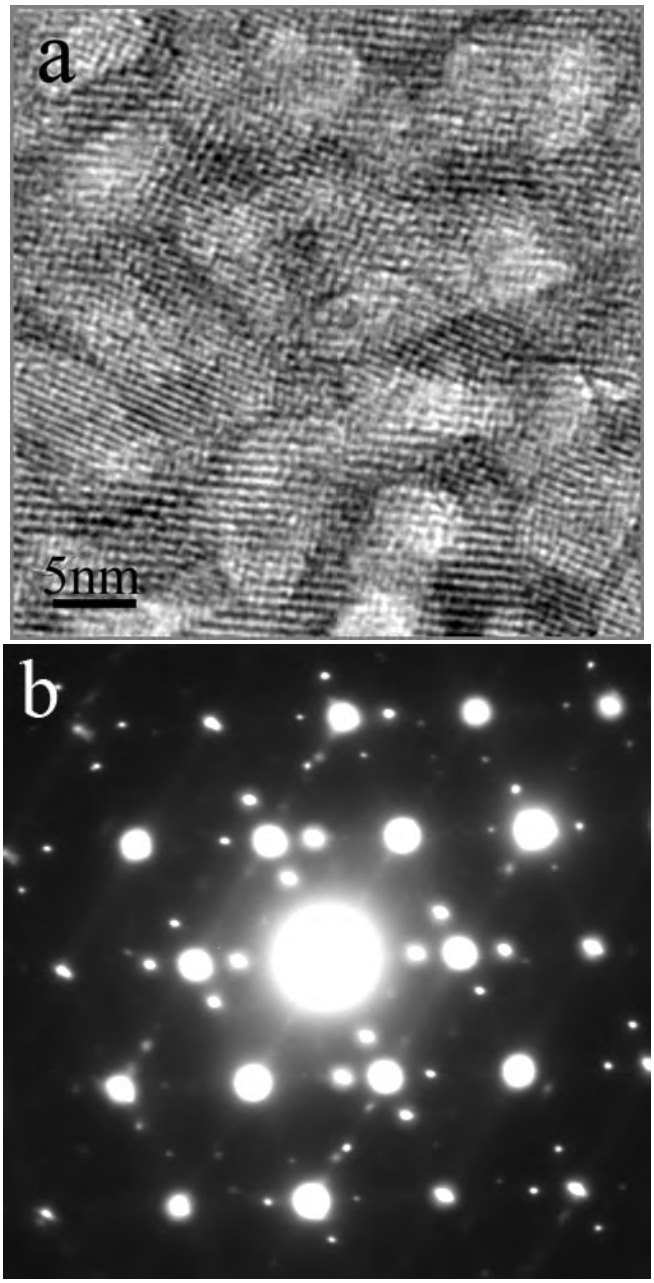

Figure 4.12. Magnelli phases formed on TiO_2 surface after annealed in either O_2 or Ar: (a) High resolution TEM of Magnelli phases; (b) Electron diffraction pattern for Magnelli phase.

and the scattering map corresponding to the best solution is shown in Figure 4.13, which reveals the position of the surface Ti-atoms as bright spots. The position of (more weakly scattering) surface oxygen atoms is not fully revealed in the scattering maps and must be deduced through refinement analysis. But the possible location of surface oxygen atoms can be obtained directly and are shown in Figure 4.13.

Using the assigned positions of titanium atoms as a starting point, oxygen positions for an initial trial structure can be inferred by comparing the Ti-positions in the c(2x2) scattering map with the positions for a bulk-like (1x1)-terminated surface. Relative to the (1x1) stoichiometric (Figure 4.14a), the c(2x2) reconstruction has every other Ti atom shifted by approximately 1/4 lattice units in the [010] direction. This transformation takes Ti atoms from one surface five-fold O-coordinated site to an adjacent five-fold site and leads to the structure shown in Figure 4.14b: a stoichiometric trial structure for a c(2x2) reconstruction. This trial structure however refines poorly against the diffraction data, although the atoms positions fit fairly well with what was obtained from scattering map.

Considering the experimental facts, c(2x2) is apparently a reduced structure compared to stoichiometric TiO_2. Improvements were then made on this trial structure to make sure it oxygen deficient, but still valid. One of the improved structures turned out to fit the experimental data quite well. At the same time, this structure passed the DFT calculations and turned out to be energy stable too. Figure 4.14c shows the configuration of this structure, which results when oxygen vacancies are introduced into the stoichiometric c(2x2) (Figure 4.14) such that every double oxygen-bridge below Ti layer and between paired Ti

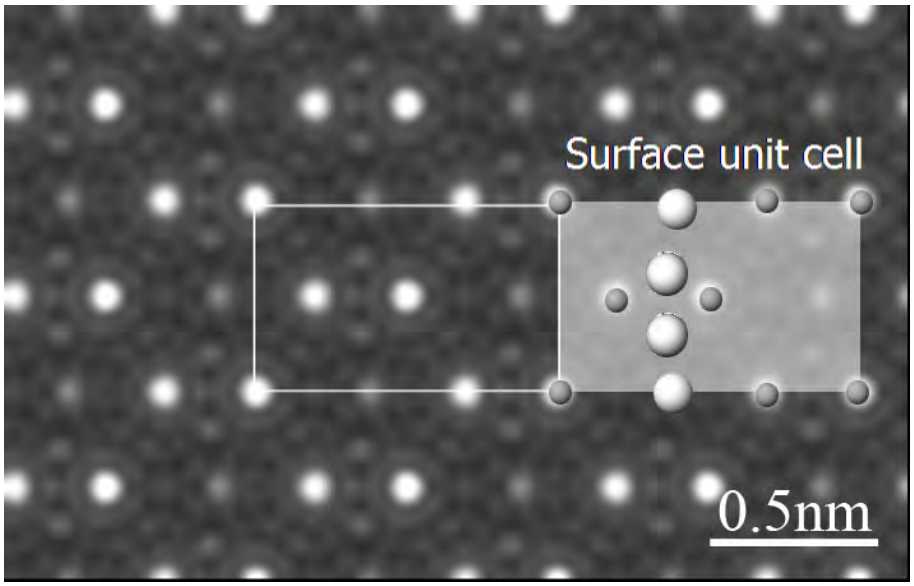

Figure 4.13. Direct Method scattering map for TiO_2 c(2x2) surface. Inset: atoms arrangements obtained directly from the map. Filled sphere Ti; open sphere O

atoms is replaced by a single oxygen-bridge. The oxygen atoms from the outermost layer were kept unchanged.

4.4.3. Energy calculation of c(2x2) surface reconstruction

The critical question is whether the surface is a local kinetic structure, as suggested by the previous literature, or is in metastable equilibrium with reduced bulk TiO_{2-x}. For this purpose, it is necessary to analyze the stability of the c(2x2) surface relative to the (1x1) surface as a function of oxygen chemical potential and temperature, furthermore, incorporate this information into the bulk phase diagram to explore the thermodynamics of the formation of the c(2x2) structure under oxidizing condition.

The tool used for this was DFT, the all-electron Wien2k (Blaha et al. 2001) code. Calculations were performed for two different models, which were constructed by putting

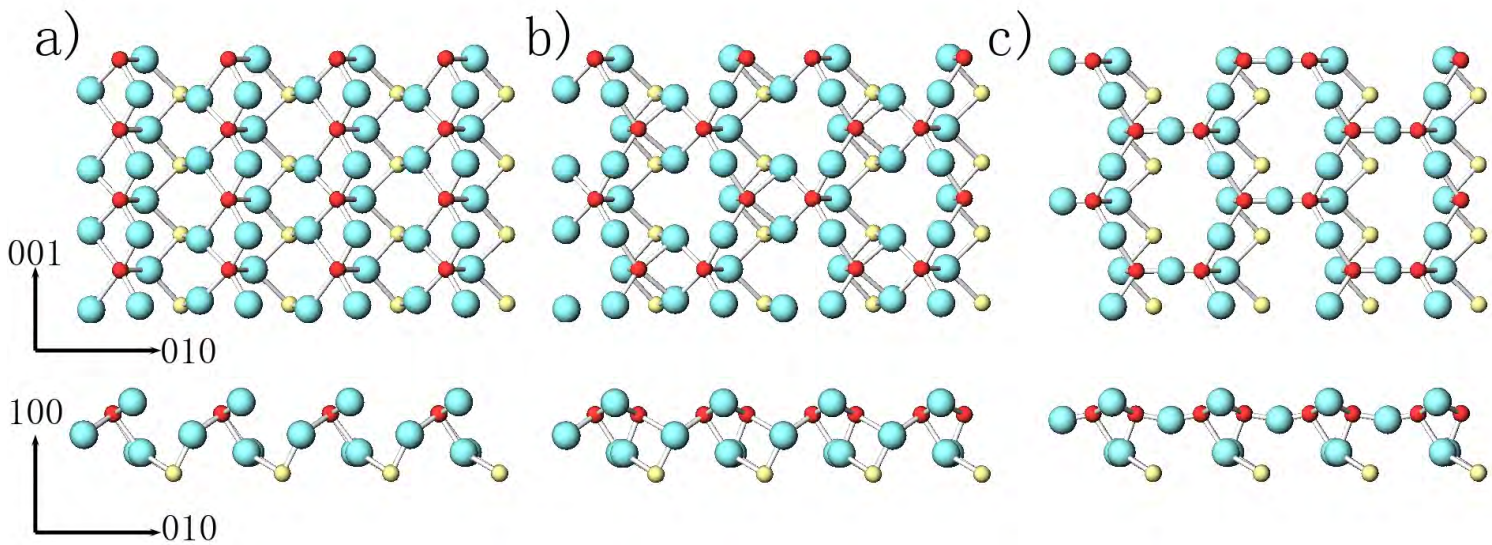

Figure 4.14. Top and side view of TiO_2 (100) surface: (a) (1x1) stoichiometric surface; (b) (2x2) stoichiometric surface; (c) (2x2) vacancy surface. Surface Titanium atoms are red, bulk Titanium atoms are yellow, Oxygen atoms are blue

the primitive c(2x2) cell on a 7 layer ($Ti_{14}O_{26}$) slab and a thicker 13 layer ($Ti_{26}O_{50}$) slab respectively. With oxygen vacancies in the surface, certain charge distribution will be introduced into the slabs. Therefore, these models can be compared to the real systems, where the c(2x2) surface is formed on a charged TiO_{2-x} bulk. In order to calibrate the equivalent stoichiometries of these two slabs, charged cell calculations for bulk TiO_2 were performed by adding different fractional charges to model TiO_{2-x}. Bader charge analysis indicated that Ti atom in stoichiometric TiO_2 has a Bader charge of 2.27 and one extra electron in the bulk will introduce a change of Bader charge by 0.26. Then the charge within the atomic spheres in a bulk was compared to the corresponding charge in the center of each slab. By this method it was estimated that the 7 layer slab corresponds to an equivalent bulk stoichiometry of $TiO_{1.975}$, the 13 layer slab to $TiO_{1.99}$.

One additional energy adjustment was taken into consideration during this calculation. It was the extra entropy contribution introduced by the fact that the reduced c(2x2) has states at the Fermi-energy. The Fermi-Dirac free energy of these n-type carriers was considered by using a conventional Mermin functional in the DFT calculations. The extra entropy contribution increases the stability of the c(2x2) structure and was estimated to be 0.32eV and 0.60eV at 1215K per primitive cell for the 7 layer ($TiO_{1.975}$) and 13 layer ($TiO_{1.99}$) structures respectively.

After combining all the above calculation, the DFT energies of the models were obtained. The next step was then to use these energies to determine if the c(2x2) structure was stable thermodynamically at certain temperature and oxygen chemical potential.

Considering the c(2x2) shares the same stoichiometry with a Ti_4O_7 structure, the oxidation reaction that transforms the c(2x2) to a (1x1) structure can be written as

$$Ti_4O_7 + 1/2O_2 \rightarrow 4TiO_2 \tag{4.2}$$

according to which, the c(2x2) is stable when the free energy change of this reaction is negative. In order to calculate the equilibrium condition for these two structures, the following procedure was followed. First, the energy required to transform the c(2x2) to a Ti_4O_7 was calculated by taking the DFT energies with additional free energy detailed above and subtracting the corresponding bulk Ti_4O_7 and TiO_2 DFT enthalpies at T=0 k. Then, this energy difference was referenced to the equilibrium between $Ti_4O_7 + 1/2O_2$ and TiO_2, which was calculated using published bulk thermodynamical data. In the end, the phase-stability diagram shown in Figure 4.15 was obtained, on which are superimposed the locations for the bulk Magnelli phase transitions as well as isoconcentration lines for three representative reduced bulk compositions as a function of oxygen chemical potential and temperature (see Appedix for detail). The lines in this figure correspond to chemical potentials for which the free-energy change for the reaction above is zero. Therefore, if the bulk isoconcentration line lies to the left of the solid line, the c(2x2) reconstruction is stable on a reduced TiO_2 crystal with that composition. The results are in good agreement with the experimental data; the c(2x2) structure is more stable than the (1x1) structure for the experimental temperatures for a relatively wide range of conditions where it is in equilibrium with reduced, bulk TiO_{2-x}.

Both the experiments and theoretical calculations lead to another important conclusion: reoxidation by gas phase O_2 is a rather slow process, since all the surfaces considered

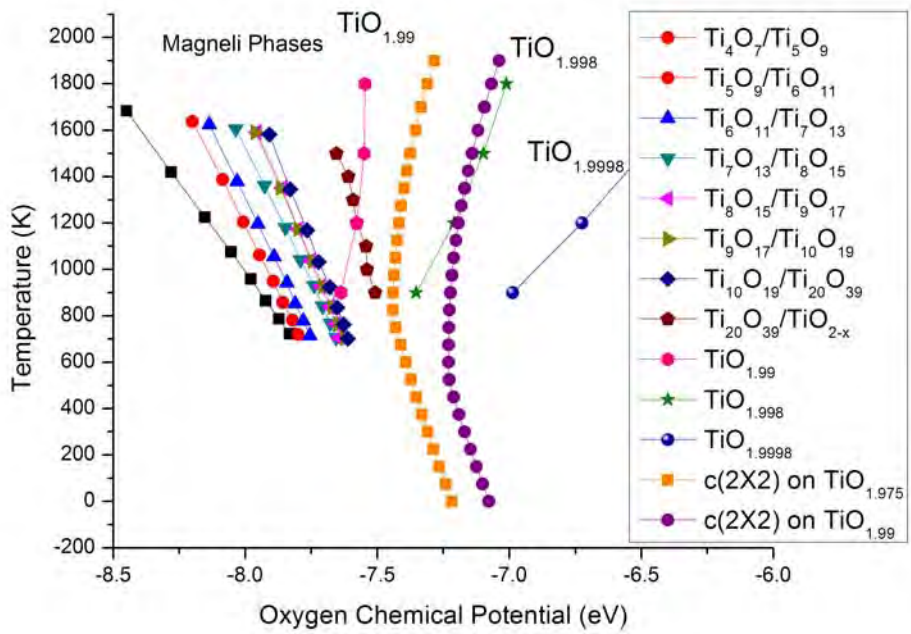

Figure 4.15. DFT calculation of c(2x2) energy on reduced TiO_2 with calculated phase diagram for the Ti-O system in the composition range between Ti_4O_7 and rutile: Magnelli phase is shown as equilibrium line between adjacent phases; c(2x2) is calculated by using Ti_4O_7 as reference

have tetrahedrally co-ordinated Ti atoms. Surfaces with tetrahedral Ti are rather unreactive and not provide ready sites for dissociation of molecular O_2, which will have to occur at surface defects. This is consistent with the experimental observation that the surfaces were stable for extended periods of time at room temperature. Therefore, it is suggested that reoxidation occurs by a process similar to Mars-Van Krevelen catalytic mechanism (Mars and van Krevelen 1954) where bulk oxygen diffusion plays a dominant role.

4.4.4. Conclusions

The c(2x2) surface reconstruction was observed when reduced TiO_2 TEM samples were re-oxidized in oxygen at around 800℃Ṫhe atomic structure and thermodynamics of a c(2x2) structure on the TiO_2(rutile) (100) surface were studied using a combination of direct methods with transmission electron diffraction data and density functional calculations. Experiments and theoretical DFT calculations including the primary electronic entropy terms yield a consistent picture that the reduced c(2x2) surface is in equilibrium with reduced, bulk TiO_{2-x}. Despite being reduced the surfaces involve a long-energy polymorphic structure with tetrahedral Ti atoms and do not provide site for dissociation of molecular O_2. Reoxidation probably involves bulk oxygen diffusion and dissociation of gas phase O_2 by a relatively low concentration of defects.

CHAPTER 5

Studies on Au/TiO_2 Model Catalysts

5.1. Sample preparation

5.1.1. Deposition precipitation method

For the purpose of investigating model catalysts with electron microscopy, all the samples in this study were prepared by depositing gold nanoparticles onto a TiO_2 single crystal TEM support. TEM supports were made following the procedure described in Chapter 2, then annealed to obtain (1x1) stoichiometric surface under the conditions detailed in Chapter 4. In this part of the study, the wet chemistry (deposition-precipitation) method described in Chapter 3 was used for gold deposition. Considering that the surface area of a single crystal is much less than that of real catalyst support in the powder form, the amount of Au precursor used was reduced accordingly. The exact same procedure was repeated in order to guarantee the comparability of real and model catalysts. During the process, extreme care was taken to insure good contact between the TEM support and solution by vigorously stirring, but at the same time maintaining the fragile TEM support without losing all of the thin area. Lights were turned off during the whole process to prevent possible decomposition of gold precursor before deposition. After the deposition, the samples were rinsed carefully using deionized water, dried in air, then saved in a clean TEM sample box wrapped with aluminum foil for further study.

5.1.2. Physical vapor deposition

(1x1) TiO_2 TEM sample was prepared by annealing and checked for the cleanness with XPS. The Denton Desk III TSC Sputter Coater at EPIC center and a standard thermal evaporation source in our UHV chamber were used to deposit metallic gold onto TEM samples. Afterward, the samples were either transfered to a JEOL 2100F microscope or studied *in situ* with the Hitachi UHV 9000 microscope. No differences were observed between these two. Although the targeted particle size could be easily achieved by carefully controlling the PVD parameters, small size variations still exist. For this reason, all of the studies about size changes of nanoparticles were carried out on the samples made at the same time, and under the same conditions.

5.2. Growing of Au on TiO_2 surface

5.2.1. Au/TiO_2 (100) surface prepared by wet chemistry

The Au/TiO_2 model catalysts were studied using a Hitachi 2000F microscope initially. Severe carbon contamination was soon observed after shining the electron beam onto the sample. The model catalyst sample was found to be very efficient in cracking hydrocarbon species in the microscope chamber with the electron beam, thus a very clean vacuum was required to carry out any form of characterization. The samples were then sent into the UHV system (see Chapter 2) and the same dry ice treatment (see Chapter 3) to the load lock was used. Beam damage was constantly monitored and beam current was kept as low as possible.

The first observation of this model catalyst was that the gold loading was very low (one magnitude lower), compared to that of real catalysts. Figure 5.1a was taken in an area

with a relatively large number of gold particles. Although some of these dark contrast area (less than 2nm in diameter) exhibit well faceted surfaces, implying the formation of gold particles, most of them are just clusters of atoms scattered randomly. STEM studies (not shown) supported this observation. The low loading of gold on the TiO_2 surface can be explained as follows. The nucleation process of deposition-precipitation is considered a preferred nucleation process where the precipitation of gold precursor only happens through ion-exchange with surface cations. The surface defect sites provide cations (protons) through water dissociation, but the number of them is greatly reduced after complete annealing in oxygen. Large gold particles have been observed in this sample too. Figure 5.1b shows the typical size (3-8nm) and location (at the edge) of these particles on TiO_2 TEM samples. Moire fringes from gold particles clearly indicate the formation of MTPs and no preferred orientation of these gold particles were observed. The extra large particle size and random orientation might be attributed to the local high concentrations of alkali in the solution during sample preparation, which facilitate gold precipitation away from the support surface, followed by attachment to the surface.

Although Au/TiO_2 model catalysts prepared by the wet chemistry method are similar to real catalysts, the low loading of gold species is a real challenge for further studies. Since it is difficult to control the surface defect density, physical vapor deposition (PVD) was used to achieve the desired amount of loading. By carefully controlling the parameters, PVD method directly results in uniformly distributed metallic gold nanoparticles of relevant sizes. Since metallic gold is considered to be essential to the catalysis process, the prepared sample should not need to be activated by reduction.

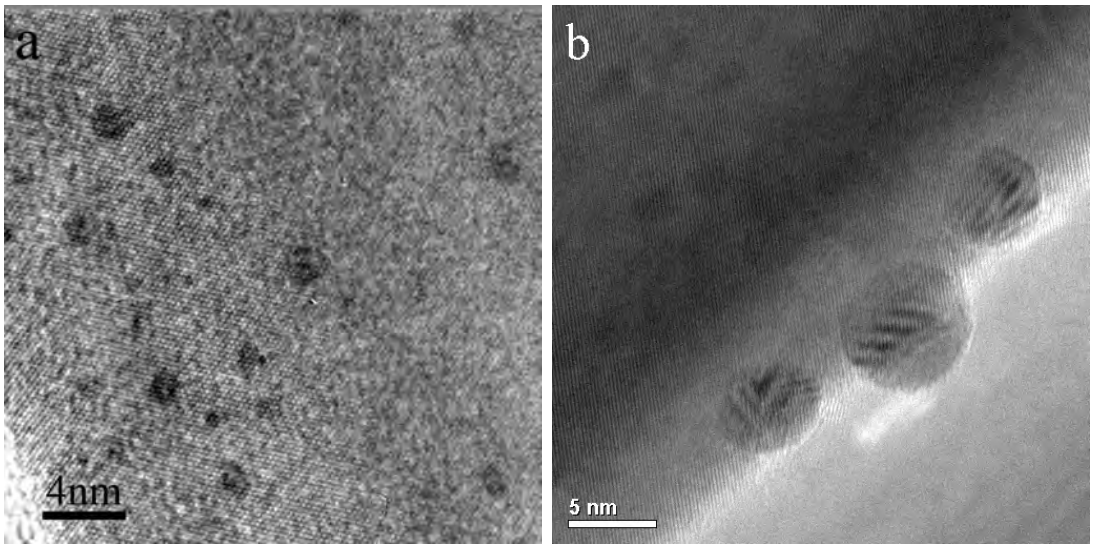

Figure 5.1. TEM images of Au/TiO_2 model catalyst sample prepared by deposition-precipitation: (a) low loading of gold on the surface; (b) gold particles with abnormally large size.

5.2.2. Au/TiO_2 (100) surface prepared by PVD

Figure 5.2a provides a typical portrait of a Au/TiO_2 model catalyst sample with gold particle size less than 2nm. No specific crystallographic orientation or shape was detected from the TEM images and diffraction patterns. From the literature (Cosandey et al. 2001), preferred orientations between gold and TiO_2 (110) have been reported in a UHV PVD study. In another study (Akita et al. 2000), a wet chemistry method was used to deposit gold nanoparticles on a rutile TiO_2 surface, and no epitaxial growth of gold was discovered either. The coincidence of reciprocal lattice point (CRLP) calculation was examined, and confirmed the possibility of having various orientation relationships between Au and rutile TiO_2 and that it is difficult to find specific orientation relationships by TEM observation. Another reason for this lack of preferred orientation is that the surface adsorbates on the TiO_2 surface interfered with the interaction between particle and surface. The TiO_2

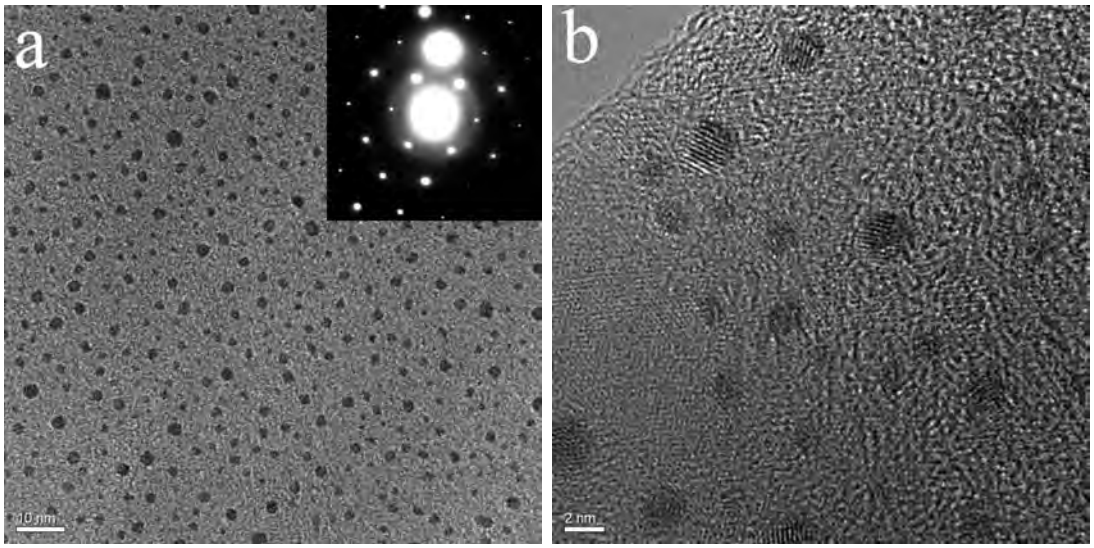

Figure 5.2. Au/TiO_2 model catalyst sample prepared by PVD: (a) TEM image at lower magnification; (b) High resolution TEM image.

surface was exposed to air before any deposition, hence hydroxyls and carbonates had been formed. They act as nucleation center for gold particles, and at the same time, blocking some of the effects from the substrate. This type of blocking can be clearly demonstrated by Au/TiO_2 (110) and was studied later. It is definitely not an ideal situation for general surface science study, but most of the real catalysts were prepared in this way. Although it is difficult to determine the preferred orientation between gold and TiO_2 support in real catalysts, and there are always some specially oriented particles found at the edge of support, there might still be no such kind of relationship existing.

After more than the desired amount of gold was deposited onto the surface, the random orientation of gold particles can been seen more clearly. With the growth of gold particles, twinning along {111}, {112} and MTPs started to appear. But all of these can not overshadow the obvious lack of direction of Moire fringes and the presence of faceted surface exposed by the profile of gold particle at the edges (Figure 5.3a). The apparent

polycrystalline diffraction pattern (Figure 5.3a inset) is another direct proof. When even more gold was added, islands were formed and the entire morphology changed, with more discrete diffraction patterns observed (Figure 5.3b).

TiO_2 (100) surfaces with various conditions have been used to determine if the change of support would introduce any difference to the gold morphology and orientation. Compared to the (1x1) surface, Magnelli phases and c(2x2) have dramatically different atomic arrangements on the surface, but after deposition, both yield similar results. From Figure 5.4a, the bulk diffraction from Magnelli phases can still be seen. The size of gold nanoparticles is so small that the discrete diffraction ring becomes diffuse. The surface diffraction from c(2x2) structure is shown in Figure 5.4b and similar diffuse diffraction ring appears in the same pattern. Both of them demonstrate the irrelevance of gold particle growth to the surface condition of the substrate.

5.2.3. Au/TiO_2 (110) and (001) surfaces prepared by PVD

TiO_2 (110) and (001) surfaces are the other two low indexed surfaces that have been extensively studied. For the purpose of comparison, it is interesting to see how gold nanoparticles interact with these two surfaces.

Among all of TiO_2 low indexed surfaces, the (110) surface is the most energy stable one. Although it has been the center of numerous studies (Diebold 2003), and is considered the 'best-characterized', prototypical metal oxide surface, the atomic-level structure of the (110) surface is quite complex. Both the oxidation conditions and the history of the TiO_2 sample have significant influence on the morphology of the surface. Recent work (Bennett et al. 1999; Li et al. 1999)on this surface suggested, for a not heavily reduced

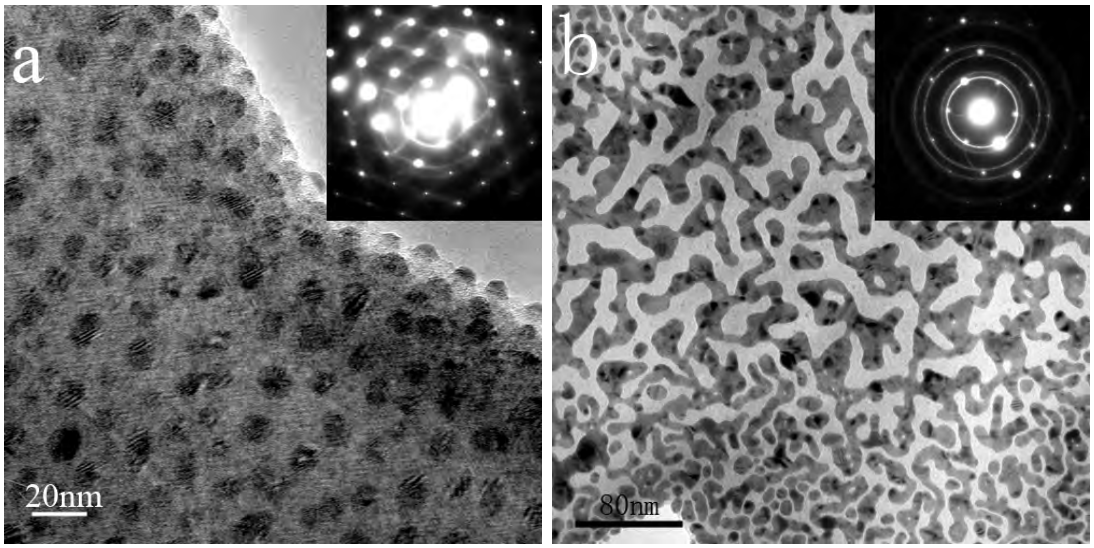

Figure 5.3. TEM images of Au/TiO_2 model catalyst sample prepared by PVD with: (a) 10 times more than desired deposition ; (b) 50 times more than desired deposition.

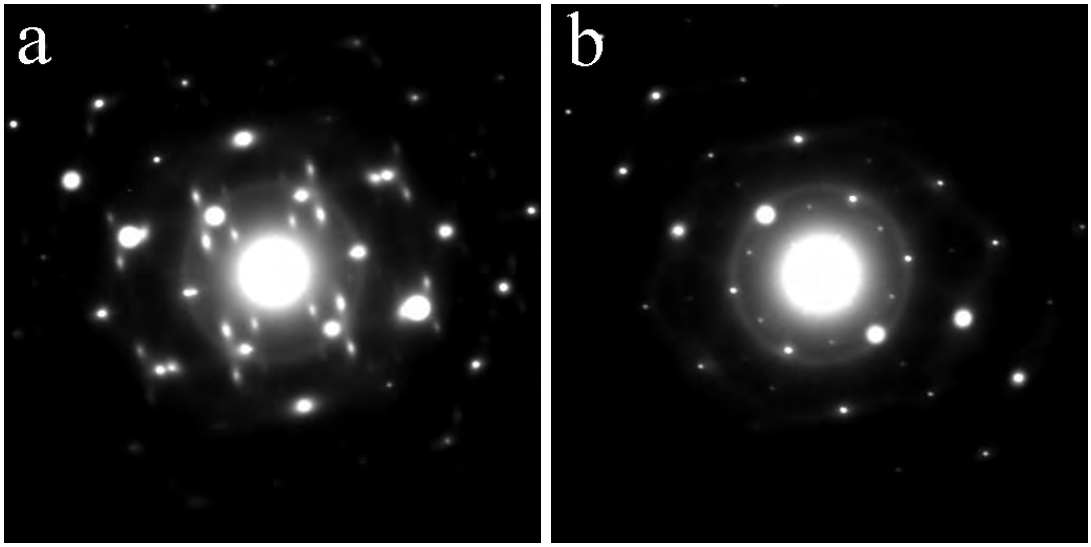

Figure 5.4. Diffraction pattern of Au/TiO_2 model catalyst sample prepared by PVD: (a) on Magnelli surface; (b) on c(2x2) surface.

TiO_2 (110) sample, annealing in oxygen will result in stoichiometric (1x1)-terminated

surface. As to the growing of gold nanoparticles on the (110) surface, a preferred orientation (Au[110]{111}//TiO_2[001](110)) was discovered when the gold nanoparticles were deposited in a UHV environment, by PVD (Cosandey et al. 2001), ion implantation followed by high temperature annealing (Wang et al. 2004) or gas-phase grafting (Akita et al. 2002). For a sample prepared using wet chemistry method, only a weak preferred orientation as above was observed (Akita et al. 2002).

The studies on the TiO_2 (001) surface have been focused on its applications for reactions of organic molecules and eletrochemistry, and very few detailed structural information is available. The (001) surface is not a low energy surface and annealing does not yield a (1x1) terminated surface. Instead, complicated {114} and {011} facets are formed (Tait and Kasowski 1979; Fukui et al. 2001). No studies of growing gold nanoparticles on this surface have been reported.

Following the procedures described in Chapter 2, single crystal TEM samples with (110) and (001) surface orientations were prepared respectively, and then annealed in oxygen at 900℃ for 1 hour to obtain desired stoichiometric (1x1) surface. The annealing condition was taken based on previous experience on the TiO_2 (100) surface, and proved to be adequate for this purpose. Figure 5.5 shows TEM image and diffraction pattern of annealed Au/TiO_2 (110) sample. A well faceted surface and a clear (1x1) pattern were obtained.

Subsequently, gold nanoparticles were deposited onto TiO_2 (110) and (001) samples at the same time using PVD method. After that, high resolution TEM and Z-contrast STEM were carried out by using a JEOL 2100F microscope. Figure 5.6 demonstrates the effects of substrates on growing gold particles. On a (110) substrate, decahedron and

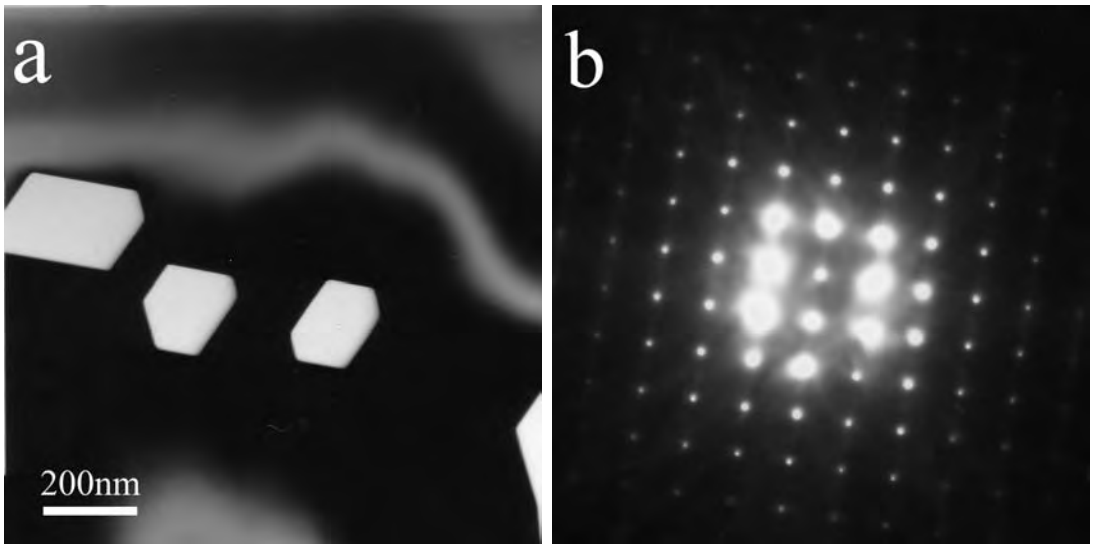

Figure 5.5. TiO_2 (110) TEM sample after annealing in oxygen at 900℃ for 1 hour (a) TEM image; (b) (1x1) diffraction pattern.

icosahedron gold MTPs with size larger than 4nm were formed across the sample (Figure 5.6a). The smaller nanoparticles ($\leq$ 2nm), which are obscured by TiO_2 substrate in TEM images, can be clearly seen in the STEM image (Figure 5.6b). A preferred orientation between the gold particles and the (110) surface were not observed on this sample. Gold nanaparticles deposited on TiO_2 (001) substrate didn't show the formation of very large particles, and therefore, far more particles can be observed (Figure 5.6d). Specific facets of individual gold particles were found to align with substrate [1-10] direction. Therefore, the possibility of a match between Au(211) (1.67Å) and TiO_2 [220] (1.62Å) was investigated. However, the diffraction patterns from this area (not shown) dismissed this possibility due to lack of the discrete diffraction spots from gold.

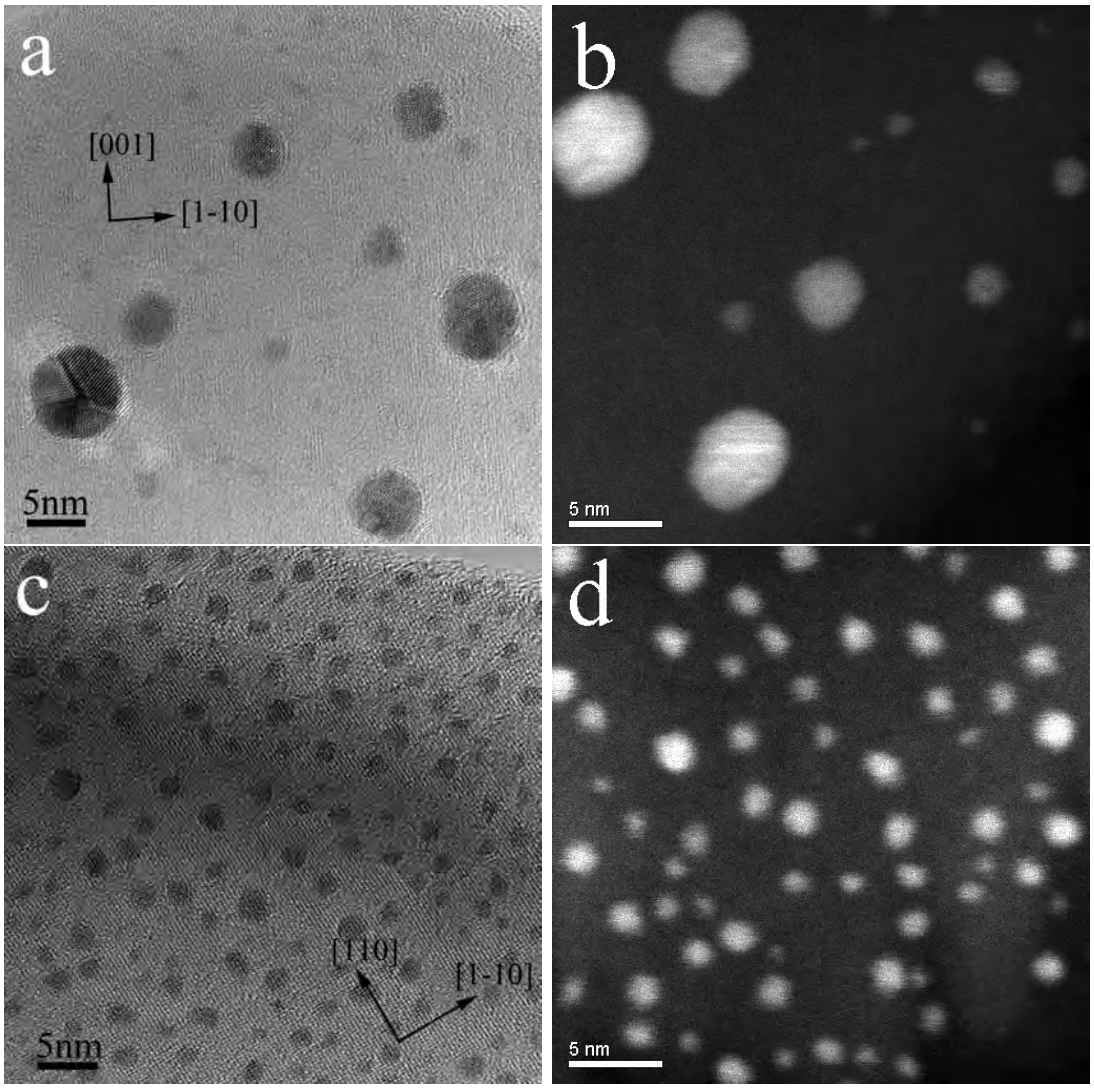

Figure 5.6. Au/TiO_2 system (a) TEM image of Au/TiO_2 (110); (b) STEM image of Au/TiO_2 (110); (c) TEM image of Au/TiO_2 (001); (d) STEM image of Au/TiO_2 (001).

5.2.4. Conclusions

The Au/TiO_2 model catalyst studies covered the growing, sintering and catalytic properties of gold nanoparticles deposited onto TiO_2 surface. There was no preferred orientation of gold particles found on any types of TiO_2 surfaces studied. It is not a very surprising

result considering only weak epitaxial relationship has been reported when gold particles were deposited onto a non-UHV-clean TiO_2 flat surface. It should be the same case in a real catalyst. This means the orientation relationship between gold particles and TiO_2 support is not that crucial for its catalytic property.

5.3. Sintering of Au on TiO_2 (100) surface

5.3.1. Experiments

Reaction induced sintering has long been observed in Au catalysts supported by various types of oxide supports. Figure 3.11, obtained in this study, is a good example of this phenomenon. Although it is a well known fact, very few studies have been carried out to characterize and provide a quantified description of reaction induced sintering. The most important reason might be, compared to heating (calcination) induced sintering, that the particle size change resulting from reaction is rather small. Relatively high temperatures (above 300℃) were widely used in calcination, therefore the magnitude and speed of sintering was dramatically different. Relatively, the reaction induced sintering is almost neglectable. Since most of catalysts were calcined before reaction and particles are already stabilized, reaction induced heating can not make significant impact on particle size and activity. But in our case, the CO oxidation reaction releases a fair amount of heat. For an active catalyst (typically 0.1 g), running a reaction (total flow rate 600 cc/min, CO 1%, O_2 2.5%) for half an hour will noticebly increase the temperature of the reaction cell by more than 3℃, which was measured by a thermocouple placed outside of the cell. Local temperature on the gold surface was definitely much higher in order for the heat to elevate the temperature of the whole cell. At the same time, the uncalcined Au/TiO_2 catalysts

are the most active ones. The initial gold particle size is extremely small (less than 2nm), hence the change introduced by reaction heat should be huge. Considering the crucial role of particle size plays in the catalytic properties of Au catalysts, it is necessary to make further investigation.

Another reason for the lack of reaction induced sintering studies might lie in the difficulty of analyzing gold nanoparticles on a complicated surface, as in a real catalyst, where surface defects are prevalent. Therefore, no statistically relevant results can be obtained to manifest the size change. The lack of a reliable way to measure the size of very small particles might be one of the reason too. For particles with size less than 1 nm, even high resolution TEM is plagued by severe contrast and focusing problems, which can easily lead to size errors of the order of 70% (Poppa 1993). In this study, Au/TiO_2 model catalysts were used as a simple and controllable environment. STEM Z-contrast imaging technique was used to measure the size of gold particle due to its sensitivity to heavy elements and ease of interpretation.

Before PVD, multiple (1x1) TiO_2 TEM samples were prepared by annealing at high temperature in oxygen. TEM and XPS were carried out to verify the surface condition and cleanness. Gold nanoparticles were then deposited onto those TEM samples using PVD method at the same time. The samples followed one of the treatments listed in Table 5.1, respectively. A JEOL 2100F microscope was then used to characterize these samples.

Table 5.1. Parameters used in reaction induced sintering experiments

Treatment	Temperature (℃)	Time (Hour)	Environment (1 atm)
Annealing	100	1	Air
Annealing	200	1	Air
Annealing	300	1	Air
Gas Treatment	RT	1	Reaction Gas (1%CO, 2.5%O_2)

5.3.2. Results and discussion

The STEM images of Au/TiO_2 model catalyst samples after various treatments are shown in Figure 5.7. Little difference can be told from the as prepared sample (Figure 5.7a) and the sample annealed at 100℃ (Figure 5.7b). On the sample annealed at 200℃, the number of ultra small (less than 2 nm) gold particles was drastically reduced, since sintering took place and small particles migrated and agglomerated with big particles. At 300℃, the inter-particle space was increased and very large particles were formed.

For samples which underwent reaction gas treatment, no apparent changes in particle size and morphology were observed (Figure 5.8). Only carefully carried out statistical analysis can help tell the difference. In Figure 5.9, the size of more than 300 particles was measured and counted. The trend of particle size increase can easily be seen for the as prepared sample, sample annealed at 100℃, and sample treated in reaction gas. Similarly, a graph (Figure 5.10) showing the increase of particle size for sample annealed at 200℃ and 300℃ can be drawn, by measuring and counting more than 200 particles.

The above results indicate that the effect of reaction heat produced on the gold surface is similar to annealing the whole sample at a temperature between 100℃ and 200℃. This is a surprisingly high number compared to the temperature observed during reaction. Although it is extremely difficult to measure the local heating produced by reaction on the

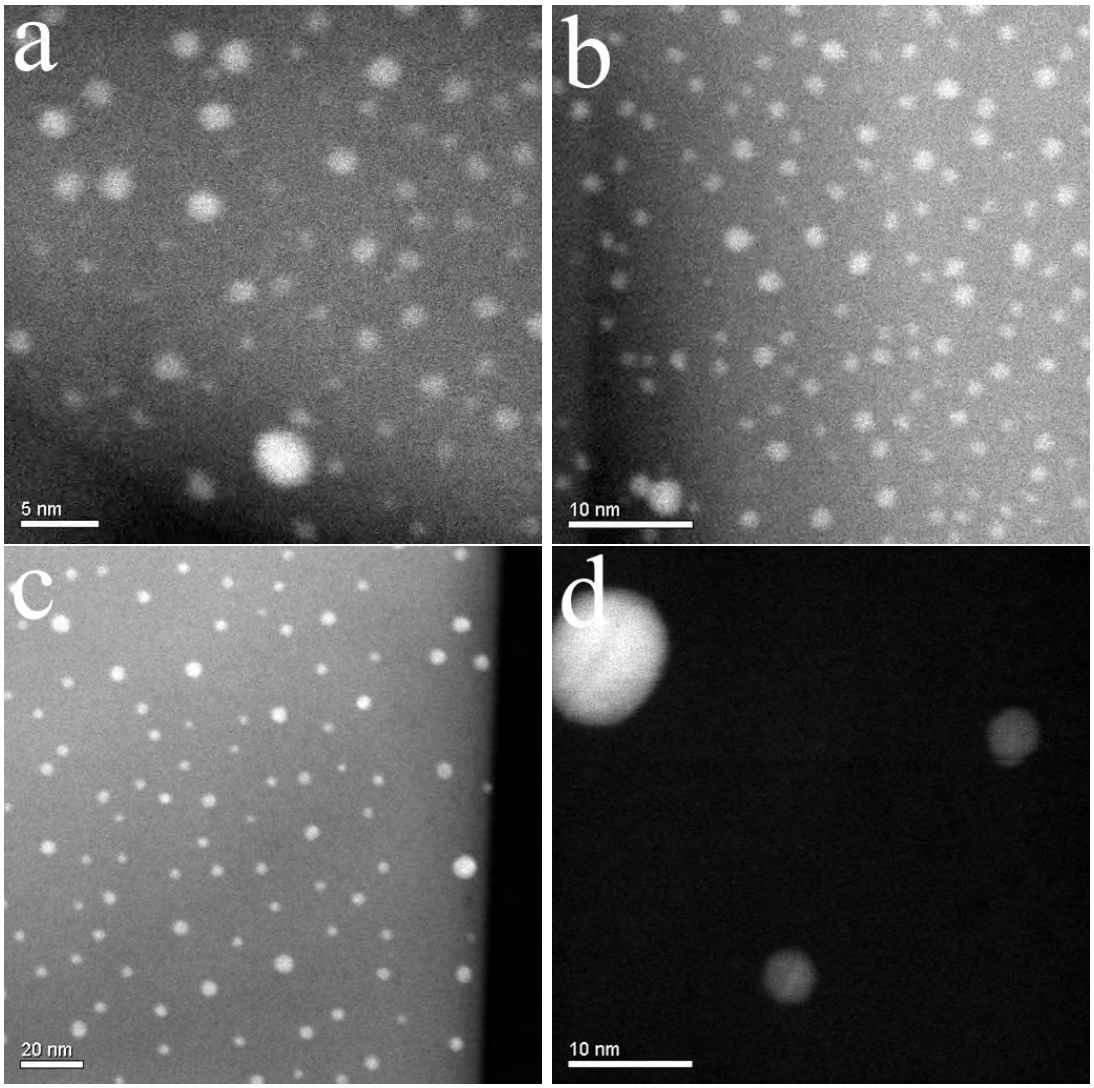

Figure 5.7. STEM Z-contrast image of Au/TiO_2 model catalyst sample: (a) as prepared; (b) annealed in air for 1 hour at 100℃; (c) annealed in air for 1 hour at 200℃; (d) annealed in air for 1 hour at 300℃.

surface, this set of experiments essentially demonstrated a new way to roughly measure it by evaluating the effects of this local heating. That is, the temperature of the Au particle - support interface is probably between 100-200℃ during reaction.

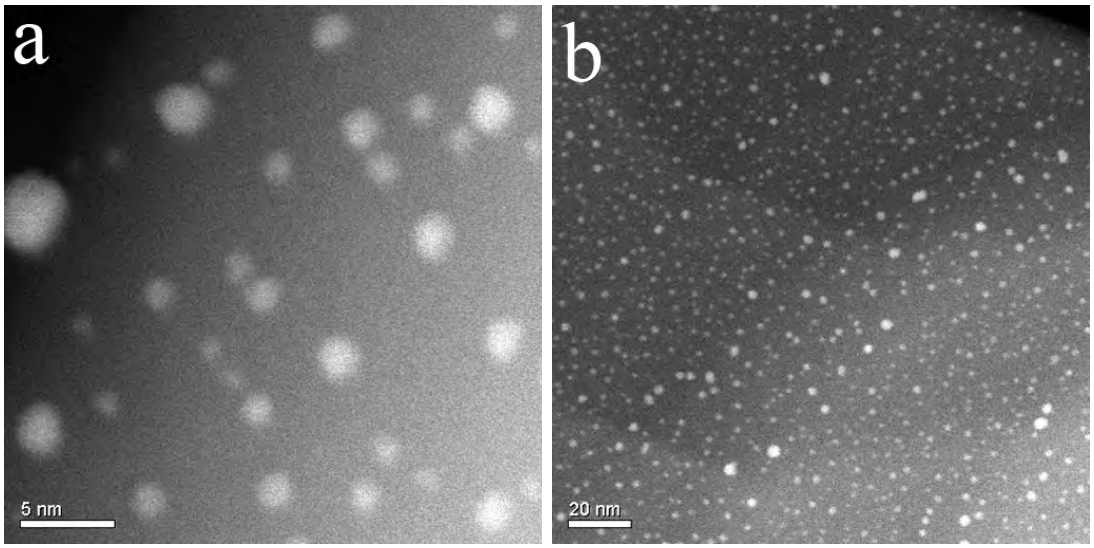

Figure 5.8. STEM Z-contrast image of Au/TiO_2 model catalyst sample after 1 hour CO oxidation reaction gas treatment at room temperature: (a) at high magnification; (b) at low magnification.

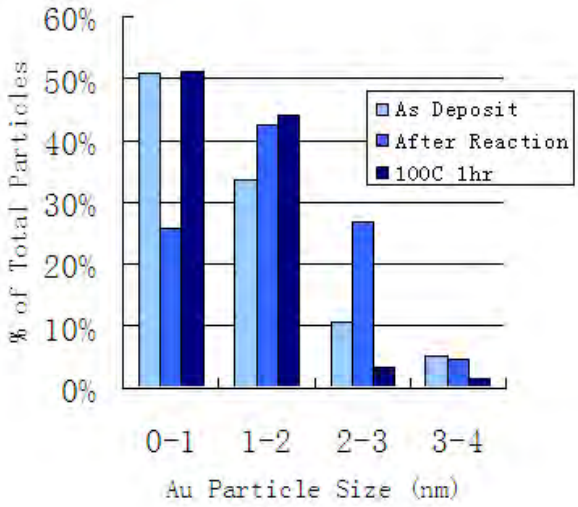

Figure 5.9. Size distribution of gold particles for as prepared sample, sample annealed in air for 1 hour at 100℃ and sample treated by reaction gas for 1 hour at room temperature, respectively.

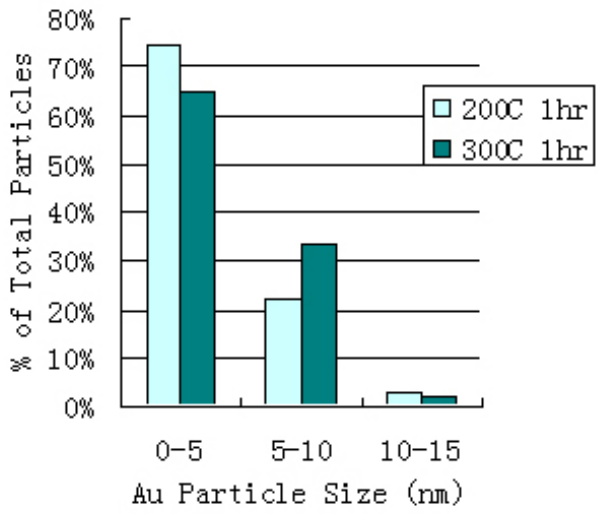

Figure 5.10. Size distribution of gold particles for samples annealed in air for 1 hour at 200℃ and 300℃ respectively.

5.3.3. Conclusions

Reaction induced sintering was observed when a Au/TiO_2 catalyst sample was exposed to a reaction gas flow. After comparing the particle size with those from annealed model samples, the conclusion was made that the local heat generated by reaction mobilized gold particles and this effect is comparable to annealing the sample at a temperature between 100-200℃.

5.4. Catalysis of Au on TiO_2 surface

5.4.1. Experiment

The above studies on reaction induced sintering were partly based on the assumption that the Au/TiO_2 model catalysts were catalytically active. Although the change of gold

particle size after treatment of reaction gas agrees with this assumption, it is still more convincing if direct evidence of activity can be measured.

The catalytic activities of model catalysts have been studied widely. Due to its low surface area, a specially designed system was usually needed in order to analyze small amounts of products (Goodman 1995b). In this study, efforts were made to measure activity data of CO oxidation reaction from a Au/TiO_2 model catalyst using available experimental systems and techniques at Northwestern University. The experiments were carried out by J.D. Henao from Prof. H.H. Kung's research group. The initial result obtained will be presented later.

The most difficult part of this study is to circumvent the small total amount of catalytically active species in a model catalyst. For the model catalyst used in the experiment, the loading of gold nanoparticles are much lower (10^{-6}) than real catalysts, even after maximizing the number of single crystal plates. Experimental techniques have been designed to better detect trace amounts of reaction products by taking the following procedures:

(1) Technique : FTIR and Mass spectrometry (see Chapter 2) to improve detection limit.

(2) Isotope : O^{18} to distinctively label the reaction product.

(3) Reaction : Small reaction cell to increase the concentration of products; and high reaction temperature and trapping experiment to increase the total amount of products.

5.4.2. Results and discussion

The most promising results came from FTIR experiments, where 1%CO and 2.5%O_2^{18} in He were trapped in a 6 mL heated (80℃) reaction cell, and IR tranmitted though the single crystal substrates was used to monitor the gas contents and surface adsorbates.

Figure 5.11 shows the changes of CO and CO_2 concentration in the trapped reaction gas. After taking the leak rate of the reaction cell into account, the only promising sign of activity is the decreasing of CO concentration and the carbonate (FTIR spectrum not shown) buildup on TiO_2 surfaces during the first several hours of reaction. The fact that CO_2 production was not observed can probably be explained by the generation of carbonates instead and these carbonates prevent CO from further oxidization.

5.4.3. Conclusions

Attempts were made to measure the catalytic activity of Au/TiO_2 model catalyst for CO oxidation. Other than carbonate buildup on the surface after the model catalyst contacts with reaction gas, no gas phase CO_2 was observed using FTIR or mass spectrometry. This low activity might be caused by blocking of the active sites by the carbonates formed, which was detected. Further investigation needs to be carried out in order to find out why this sample is not as active as real catalysts.

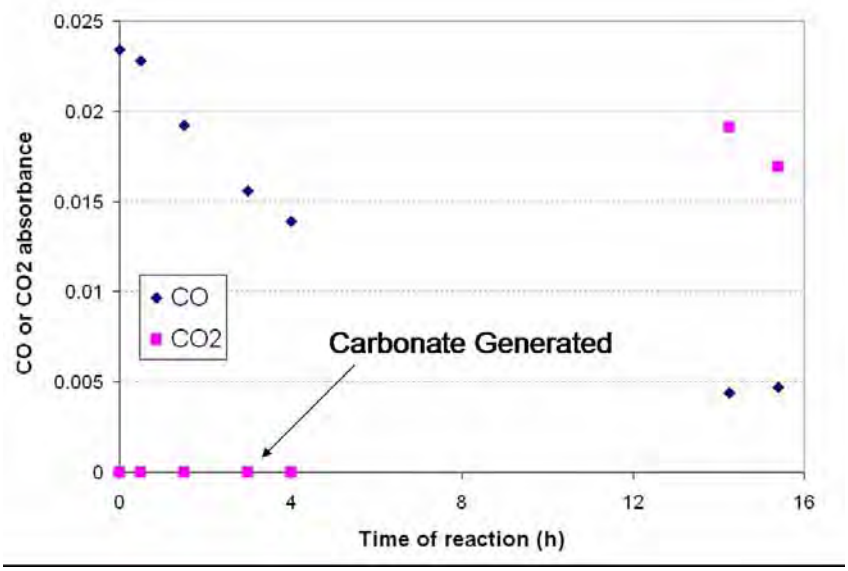

Figure 5.11. FTIR experiment on the activity of Au/TiO_2 model catalyst: the changes of CO and CO_2 concentration in the trapped reaction gas

CHAPTER 6

Conclusions and Future Work

6.1. Conclusions

The objective of this research was to develop insight into the many factors affecting catalytic properties of oxide supported gold catalysts, in order to explain the existing observations and provide clear and relevant characterizations of this catalytic system. This objective was accomplished by studying the surface of oxide supports and oxide supported Au catalytic systems, representing both real and model catalysts, using electron microscopy and other surface science techniques.

The studies of Au catalysts was carried out in two directions. The research on the effect of preparation methods on catalytic properties revealed the dual role of Cl^- in suppressing the CO oxidation activity of a Au/Al_2O_3 catalyst: accelerating the agglomeration of gold particles and poisoning the active sites. Considering the fact that only a small amount of Cl^- was needed for poisoning and the amount of residual Cl^- on the catalyst is decided by the pH value during deposition-precipitation and the rinsing afterwords, one can coclude that this certainly is one of the reasons why the activity of a Au catalyst is so sensitive to the preparation condition. The research on the activation of Au/Al_2O_3 and Au/TiO_2 catalysts demonstrated that the oxidation state and the size of the gold particles were two important competing factors during catalytic activation. The difference in the mobility of gold species on oxide surfaces affects them. Au/Al_2O_3 catalysts were not as

easily activated as Au/TiO_2 catalysts. Gold atoms/ions have low mobility on the Al_2O_3 surfaces. The agglomeration of gold atoms was hindered by their low mobility on the Al_2O_3 surface. Since the size of gold particles, once formed, does not change significantly during activation, the oxidation state of gold species can be used as an indicator for the activities of the catalysts. In the case of Au/TiO_2 catalysts, gold has a higher mobility on TiO_2. Both the reduction of ionic gold and the growing of gold particles are very fast during the activation. And the induction period suggests that ionic gold species agglomerate before being reduced.

When a reduced TiO_2 was annealed in oxidizing environment, the surface slowly reoxidized by diffusion of interstitial Ti to the surface and reaction with atmospheric oxygen. A c(2x2) surface reconstruction occured before the surface regain stoichiometry. Experiments and theoretical DFT calculations including the primary electronic entropy terms yield a consistent picture that the reduced c(2x2) surface is in equilibrium with reduced, bulk TiO_{2-x}. Despite being reduced the surfaces involve a long-energy polymorphic structure with tetrahedral Ti atoms and do not provide sites for dissociation of molecular O_2. Reoxidation probably involves bulk oxygen diffusion and dissociation of gas phase O_2 at a relatively low concentration of defects.

The Au/TiO_2 model catalyst studies covered the growing, sintering and catalytic properties of gold nanoparticles deposited onto TiO_2 surfaces. There was no preferred orientation of gold particles found on all types of TiO_2 surfaces studied. It is not a very surprising result considering that only weak epitaxial relationships have been reported when gold particles were deposited onto a non-UHV-clean TiO_2 flat surface (see Chapter 5). It should be the same case in a real catalyst. However, reaction induced sintering

was observed when a Au/TiO_2 catalyst sample was put into a reaction gas flow. After comparing the particle size with those from annealed model catalysts, the conclusion was made that the local heat generated by reaction mobolized gold particles and this effect is comparable to annealing the sample at a temperature between 100-200℃. Finally, attempts were made to measure the catalytic activity of Au/TiO_2 model catalyst for CO oxidation. Other than carbonate buildup on the surface after the model catalyst contacts with reaction gas, no gas phase CO_2 was observed using FTIR or mass spectrometry. This low activity might be caused by blocking of the active sites by the carbonates.

6.2. Future work

The top priority for future work should be given to the investigation of catalytic properties of the model catalyst, since these measurement will provide a direct link between real and model catalysts. First, the carbonate buildup problem should be verified by using XPS, Auger Electron Spectroscopy or other surface sensitive techniques. The origin of the carbonates should be invesitgated too. It is quite possible that the problem was the clean (1x1) TiO_2 surface. As mentioned in Chapter 5, when a Au/TiO_2 model catalyst were studied in TEM, it would be contaminated very quickly after high energy electron beam shone on the sample. This phenomenon was observed on single crystal TiO_2 samples also but never happened to real catalyst samples. Since TiO_2 itself is a very good catalyst with many applications, it is worthwhile to investigate the difference between powder TiO_2 sample and the (1x1) single crystal TiO_2 sample.

Another direction of future work is related to the TiO_2 surfaces also. The low loading of gold nanoparticles on the TiO_2 surface was the major obstacle to use the wet chemistry

method to prepare samples for reaction. It would be ideal if the TiO_2 (1x1) surface can be modified to a known structure and kept passivated. As mentioned above, we need to know the surface structure of the powder TiO_2 sample first.

The mobility of gold atoms on different oxide surfaces is apparently different. However, how does this difference affect the property of Au catalyst is still not clear. To what extent is the reduction rate dependent on the mobility of gold species? The answer to this question would be helpful to understand the different procedure it takes to activate Au/Al_2O_3 and Au/TiO_2 catalyst.

References

Akita, T., M. Okumura, K. Tanaka, and M. Haruta. 2002. SEM and RHEED-REM study of Au particles deposited on rutile TiO_2 (110) by deposition precipitation and gas-phase grafting methods. *J. Catal.* 212:119–123.

Akita, T., K. Tanaka, S. Tsubota, and M. Haruta. 2000. Analytical high-resolution TEM study of supported gold catalysts: Orientation relationship between Au particles and TiO_2 supports. *J. Electron Microscopy* 49:657–662.

Anderson, J.S., and B.G. Hyde. 1967. On possible role of dislocations in generating ordered and disordered shear structures. *J. Phys. Chem. Solids* 28:1393.

Askgaard, T.S., J.K. Norskov, C.V. Ovesen, and P.J. Stoltze. 1995. A kinetic model of methanol synthesis. *J. Catal.* 156:229–242.

Bengu, E., and L. D. Marks. 2001. Single-walled BN nanostructures. *Phys. Rev. Lett.* 86: 2385–2387.

Bennett, R.A., P.Stone, N. J. Price, and M. Bowker. 1999. Two (1 x 2) reconstructions of TiO_2 (110): Surface rearrangement and reactivity studied using elevated temperature scanning tunneling microscopy. *Phys. Rev. Lett.* 82:3831–3834.

Blaha, P., K. Schwarz, G.K.H. Madsen, D. Kvasnicka, and J. Luitz. 2001. *WIEN2k, an augmented plane wave +local orbitals program for calculating crystal properties.* Techn. Universitat, Wien, Austria.

Blanchin, M.G., and L.A. Bursill. 1984. Extended versus small defect equilibria in non-stoichiometric rutile 1.Dissolution and re-precipitation of extended defects observed by *in situ* transmission electron-microscopy. *Phys. Status Solidi A* 86:101–109.

Boccuzzi, F., A. Chiorino, M. Manzoli, P. Lu, T. Akita, S. Ichikawa, and M. Haruta. 2001. Au/TiO_2 nanosized samples: A catalytic, TEM, and FTIR study of the effect of calcination temperature on the CO oxidation. *J. Catal.* 202:256–267.

Bond, G.C., P.A. Sermon, G. Webb, D.A. Buchanan, and P.B. Wellls. 1973. Hydrogenation over supported gold catalysts. *J. Chem. Soc. Chem. Commun.* 13:444–445.

Bovin, J. O., and Wallenberg R. D. J. Smith. 1985. Imaging of atomic clouds outside the surfaces of gold crystals by electron microscopy. *Nature* 317:47–49.

Brooks, I. M., C. A. Muryn, and G. Thornton. 2001. Imaging water dissociation on TiO_2(110). *Phys. Rev. Lett.* 87:266103.

Buckett, M. 1991. Electron irradiation damage in transition metal oxides. Ph.D. thesis, Northwestern University.

Bursill, L.A., and M.G. Blanchin. 1984. Precipitation phenomena in non-stoichiometric oxides .2. (100) platelet defects in reduced rutiles. *PROCEEDINGS OF THE ROYAL SOCIETY OF LONDON SERIES A-MATHEMATICAL PHYSICAL AND ENGINEERING SCIENCES* 391:373.

Campbell, C.T. 1997. Ultrathin metal films and particles on oxide surfaces: structural, electronic and chemisorptive properties. *Surf. Sci. Rep.* 27:1–111.

Cha, D.Y., and G. Parravano. 1979. Surface reactivity of supported gold : I. Oxygen transfer between CO and CO_2. *J. Catal.* 18:200–211.

Che, M., and C.O. Bennett. 1989. *Adv. Catal.* 36:55.

Collazo-Davila, C. 1999. Initial stages of thin film deposition: Metal-induced surface reconstruction on semiconductors and the nucleation of cubic boron nitride. Ph.D. thesis, Northwestern University.

Collazo-Davila, C., E. Landree, D. Grozea, G. Jayaram, R. Plass, P. C. Stair, and L. D. Marks. 1995. Design and initial performance of an ultrahigh vacuum sample preparation, evaluation, analysis and reaction (SPEAR) system. *J. Mic. Soc. Am.* 1:267–279.

Coluccia, S., A.J. Tench, and R.L. Segall. 1979. Surface-structure and surface-states in magnesium-oxide powders. *J. Chem. Soc. Faraday Trans.* I:1769.

Combettes, P. L. 1996. The convex feasibility problem in image recovery. *Adv. Imaging Electron Phys.* 95:155.

Cosandey, F., L. Zhang, and T.E. Madey. 2001. Effect of substrate temperature on the epitaxial growth of Au on TiO_2(110). *Surf. Sci.* 474:1–13.

Costello, C.K. 2003. Aspects of CO oxidation over supported gold ctaalysts and characterization of the active site. Ph.D. thesis, Northwestern University.

Costello, C.K., J. Guzman, and J.H. Yang. 2004. Activation of Au/gamma-al_2o_3 catalysts for CO oxidation: Characterization by x-ray absorption near edge structure and temperature programmed reduction. *J. Phys. Chem. B* 108:12529–12536.

Costello, C.K., M.C. Kung, H.S. Oh, Y. Wang, and H.H. Kung. 2002. Nature of the active site for co oxidation on highly active Au/gamma-Al_2O_3. *Appl. Catal. A* 232:159–168.

Costello, C.K., J.H. Yang, H.Y. Law, Y. Wang, J.N. Lin, L. D. Marks, M.C. Kung, and H.H. Kung. 2003. On the potential role of hydroxyl groups in CO oxidation over Au/gamma-Al_2O_3. *Appl. Catal. A* 243:15–24.

Cowley, J. M. 1986. *Diffraction physics.* Amsterdam: North Holland Physics Publishing.

Crew, W.W., and R.J. Madix. 1994. Monitoring surface reactions with scanning tunneling microscopy: CO oxidation on p(2x1) O pre-covered Cu(110) at 400k. *Surf. Sci.* 319: L34–L40.

Cronemeyer, D.C. 1952. Electrical and optical properties of rutile single crystals. *Phys. Rev.* 87:876.

Diebold, U. 2003. The surface science of titanium dioxide. *Surf. Sci. Rep.* 48:229.

Diebold, U., M. Li, O. Dulub, E. L. D. Hebenstreit, and W. Hebenstreit. 2000. The relationship between bulk and surface properties of rutile TiO_2(110). *Surf. Rev. Lett.* 7:613.

Dorset, D. L. 1997. The accurate electron crystallographic refinement of organic structures containing heavy atoms. *Acta Crystallogr.* A53:356–365.

Erdman, N., M. Asta, O. Warschkow, D. E. Ellis, K. R. Poeppelmeier, and L. D. Marks. 2002. The structure and chemistry of the TiO_2-rich surface of $SrTiO_3$(001). *Nature* 419:55–58.

Ertl, G. 1983. In *Catalysis, science and technology*, ed. J.R. Anderson and M. Boudart, vol. 1, 209. Berlin: Springer.

Fukui, K., R. Tero, and Y. Iwasawa. 2001. Atom-resolved structures of TiO_2(001) surface by scanning tunneling microscopy. *Jap. J. Appl. Phys. Part I* 40:4331–4333.

Galvano, S., and G. Parravano. 1978. Chemical reactivity of supported gold : IV. Reduction of NO by H_2. *J. Catal.* 55:178–190.

Gao, Y., Y. Liang, and S. A. Chambers. 1996. Thermal stability and the role of oxygen vacancy defects in strong metal support interaction - Pt on Nb-doped TiO_2(100). *Surf. Sci.* 365:638–648.

Gerchberg, R. W., and W. O. Saxton. 1972. A practical algorithm for the determination of the phase from image and diffraction plane pictures. *Optik* 35:237–246.

Goldberg, D. E. 1997. *Genetic algorithms in search, optimization and machine learning.* Massachusetts: Addision Wesley Longman, Inc.

Goodman, D.W. 1995a. Model catalysts - from extended single-crystals to supported particles. *Surf. Rev. Lett.* 2:9–24.

———. 1995b. Model studies in catalysis using surface science probes. *Chem. Rev.* 95: 523–536.

Grant, F.A. 1959. Properties of rutile (titanium dioxide). *Rev. Mod. Phys.* 31:646–674.

Grozea, D., E. Bengu, and L. D. Marks. 2000. Surface phase diagrams for the Ag-Ge(111) and Au-Si(111) systems. *Surf. Sci.* 461:23–30.

Gunter, P.L.J., J.W.H. Niemantsverdriet, EH. Ribeiro, and G.A. Somorjai. 1997. *Catal. Rev. Sci. Eng.* 39:77.

Guo, Q., I. Cocks, and E.M. Williams. 1996. ESDIAD and LEED studies of the clean TiO_2(100) surface. *Surf. Sci.* 366:99–106.

Gupta, N.M., and A.K. Tripathi. 2001. The role of nanosized gold particles in adsorption and oxidation of carbon monoxide over Au/Fe_2O_3 catalyst. *Gold Bull.* 34:120–128.

Hagen, J., L.D. Socaciu, M. Elijazyfer, U. Heiz, T.M. Bernhardt, and L. Wste. 2002. Coadsorption of CO and O_2 on small free gold cluster anions at cryogenic temperatures: Model complexes for catalytic CO oxidation. *Phys. Chem. Chem. Phys.* 4:1707–1709.

Harber, J., and P. Nowak. 1999. The interaction of rutile (TiO_2) surface with some catalytically active transition metal oxides during heating, studied by electrochemical methods. *Top. Catal.* 8:199–209.

Haruta, M., T. Kobayashi, H. Sano, and N. Yamada. 1987. Novel gold catalysts for the oxidation of carbon-monoxide at a temperature far below 0℃. *Chem. Lett.* 2:404–408.

Haruta, M., S. Tsubota, T. Kobayashi, H. Kageyama, M.J. Genet, and B. Delmon. 1993. Low-temperature oxidation of CO over gold supported on TiO_2, α-Fe_2O_3, and Co_3O_4. *J. Catal.* 144:175–192.

Hayashi, T., K. Tanaka, and M. Haruta. 1998. Selective vapor-phase epoxidation of propylene over Au/TiO_2 catalysts in the presence of oxygen and hydrogen. *J. Catal.* 178:566–575.

Henderson, M.A. 1995. Mechanism for the bulk-assisted reoxidation of ion sputtered TiO_2 surfaces: diffusion of oxygen to the surface or titanium to the bulk? *Surf. Sci.* 343: L1156–L1160.

———. 1999. Surface perspective on self-diffusion in rutile TiO_2. *Surf. Sci.* 419:174–187.

Hirsch, P., A. Howie, R. B. Nicholson, D. W. Pashley, and M. J. Whelan. 1977. *electron microscopy of thin crystals.* New York: Robert E. Krieger publishing co., Inc.

Horsley, J.A. 1979. Molecular-orbital study of strong metal-support interaction between platinum and titanium-dioxide. *J Amer. Chem. Soc.* 101:2870–2874.

Huber, H., G.A. Ozin, and W.J. Power. 1977. A metal atom model for the oxidation of carbon monoxide to carbon dioxide. the gold atom-carbon monoxide-dioxygen reaction and the gold atom-carbon dioxide reaction. *Inorg. Chem.* 16:975–979.

Huntington, H.B., and G.A. Sullivan. 1965. Interstitial diffusion mechanism in rutile. *Phys. Rev. Lett.* 14:177–178.

Iizuka, Y., T. Tode, T. Takao, K. Yatsu, T. Takeuchi, S. Tsubota, and M. Haruta. 1999. A kinetic and adsorption study of co oxidation over unsupported fine gold powder and

over gold supported on titanium dioxide. *J. Catal.* 187:50–58.

Kao, C.C., S.C. Tsai, M.K. Bahl, Y.W. Chung, and W.J. Lo. 1980. Electronic properties, structure and temperature-dependent composition of nickel deposited on rutile titanium dioxide (110) surfaces. *Surf. Sci.* 95:1–14.

Knotek, M.L., and P.J. Feibelman. 1979. Stability of ionically bonded surfaces in ionizing environments. *Surf. Sci.* 90:78–90.

Kofstad, P. 1967. Note on the defect structure of rutile (TiO_2). *J. Less-comon Metal.* 13: 635–638.

Kosuge, K. 1994. *Chemistry of non-stoichiometric compounds.* Oxford, New York: Oxford University Press.

Kozlov, A.I., A.P. Kozlova, H. Liu, and Y. Iwasawa. 1999. A new approach to active supported Au catalysts. *Appl. Catal. A* 182:9–28.

Kung, H.H., M.C. Kung, and C.K. Costello. 2003. Supported Au catalysts for low temperature CO oxidation. *J. Catal.* 216:425–432.

Kung, M.C., J.H. Lee, A.C. Kung, and H.H. Kung. 1996. *Porc. 11th Intern. Cong. Catal.* 701.

Lad, R.J. 1995. Interactions at metal-oxide and oxide oxide interfaces studied by ultrathin-film growth on single-crystal oxide substrates. *Surf. Rev. Lett.* 2:109–126.

LaFemina, J.P. 1994. *Crit. Rev. Surf. Chem.* 3:297.

Landree, E., C. Collazo-Davila, and L. D. Marks. 1997. Multi-solution genetic algorithm approach to surface structure determination using direct methods. *Acta Crystallogr.* B53:916–922.

Landree, E., L.D. Marks, P. Zschach, and C.J. Gilmore. 1998. Structure of the TiO_2(100)-(1x3) surface by direct methods. *Surf. Sci.* 408:300–309.

Li, M., W. Hebenstreit, L. Gross, U. Diebold, M.A. Henderson, D.R. Jennison, P.A. Schultz, and M.P. Sears. 1999. Oxygen-induced restructuring of the TiO_2(110) surface: a comprehensive study. *Surf. Sci.* 437:173–190.

Lindan, P.J.D., and N.M. Harrison. 2001. The structure of the reduced rutile TiO_2(100) (1x3) reconstruction. *Surf.Sci.* 479:L375–L381.

Liu, H., A.I. Kozlov, A.P. Kozlova, T. Shido, K. Asakura, and Y. Iwasawa. 1999. Active oxygen species and mechanism for low-temperature CO oxidation reaction on a TiO_2-supported Au catalyst prepared from Au(PPh3)(NO_3) and as-precipitated titanium hydroxide. *J. Catal.* 185:252–264.

Lo, W.J., Y.W. Chung, and G.A. Somorjai. 1978. Electron spectroscopy studies of the chemisorption of O_2, H_2 and H_2O on the TiO_2(100) surfaces with varied stoichiometry: Evidence for the photogeneration of Ti^{3+} and for its importance in chemisorption. *Surf. Sci.* 71:199.

Marks, L. D. 1999. General solution for three-dimensional surface structures using direct methods. *Phys. Rev. B* 60:2771–2780.

Marks, L. D., N. Erdman, and A. Subramanian. 2001. Crystallographic direct methods for surfaces. *J. Phys. Cond. Mat.* 13:10667–10687.

Marks, L. D., M. Kubozoe, M. Tomita, M. Ukiana, T. Furutsu, I. Matsui, and F. Nagata. 1988. Design and initial performance of a UHV-HREM. *Inst. Phys. Conf. Series* 93: 163–164.

Marks, L. D., T. S. Savage, J. P. Zhang, and R. Ai. 1991. Validity of the kinematical approximation in transmission electron diffraction from surfaces, revised. *Ultramicroscopy* 38:343–347.

Marks, L.D., P.M. Ajayan, and J. Dundurs. 1986. Quasi-melting of small particles. *Ultramicroscopy* 20:77–82.

Mars, P., and D. W. van Krevelen. 1954. Oxidations carried out by means of vanadium oxide catalysts. *Chem. Eng. Sci.* S 3:41–59.

Mavrikakis, M., P. Stoltze, and J.K. Nørskov. 2000. Making gold less noble. *Catal. Lett.* 64:101–106.

Mens, Ad J.M., and Onno L.J. Gijzeman. 1996. AES study of electron beam induced damage on TiO_2 surfaces. *Appl. Surf. Sci.* 99:133–143.

Mills, G., M.S. Gordon, and H. Metiu. 2003. Oxygen adsorption on au clusters and a rough Au(111) surface: The role of surface flatness, electron confinement, excess electrons, and band gap. *J. Chem. Phys.* 118:4198–4205.

Moorhead, R.D., and H. Poppa. 1979. In situ oxygen conditioning of (001) MgO thin film substrates for film growth studies by electron microscopy. *Thin Solid Films* 58: 169–173.

Murry, P.W., F.M. Leibsle, C.A. Muryn, H.J. Fisher, C.F.J. Flipse, and G. Thornton. 1994. Interrelationship of structure elements on TiO_2(100)-(1x3). *Phys. Rev. Lett.* 72: 689–692.

Ogawa, S., and S. Ichikawa. 1995. Observation of induced dipoles between small palladium clusters and alpha -(0001) Al_2O_3. *Phys. Rev. B* 51:17231–17234.

Okumura, M., S. Nakamura, S. Tsubota, T. Nakamura, M. Azuma, and M. Haruta. 1998. Chemical vapor deposition of gold on Al_2O_3, SiO_2, and TiO_2 for the oxidation of CO and of H_2. *Catal. Lett.* 51:53–58.

Onishi, H., and Y. Iwasawa a. 1994. Reconstruction of $TiO_2(110)$ surface - STM study with atomic-scale resolution. *Surf. Sci.* 313:L783–L789.

Onishi, H., and Y. Iwasawa b. 1996. Dynamic visualization of a metal-oxide-surface/gas-phase reaction: Time-resolved observation by scanning tunneling microscopy at 800 k. *Phys. Rev. Lett.* 76:791–794.

Onishi, H., C. Egawa, J. Aruga, and Y. Iwasawa. 1987. Adsorption of Na atoms and oxygen-containing molecules on MgO(100) and (111) surfaces. *Surf. Sci.* 191:479–491.

Pacchioni, G., and N. Rrsch. 1994. Modeling of supported metal clusters: a density functional study of CO chemisorption on Ni clusters deposited on alumina. *Surf. Sci.* 306:169–178.

Park, E.D., and J.S. Lee. 1999. Effects of pretreatment conditions on CO oxidation over supported Au catalysts. *J. Catal.* 186:1–11.

Poppa, H. 1993. Nucleation, growth, and TEM analysis of metal particles and clusters deposited in UHV. *Catal. Rev. Sci. Eng.* 35:359–398.

Purnell, S.K., X. Xu, D.W. Goodman, and B.C. Gates. 1994. Adsorption and reaction of $[Re_2(CO)_{10}]$ on ultrathin MgO films grown on a Mo(110) surface: Characterization by infrared reflection-absorption spectroscopy and temperature-programmed desorption. *J. Phys. Chem.* 98:4076–4082.

R. Persaud, T.E. Madey. 1997. In *The chemical physics of solid surfaces and heterogeneous catalysis*, ed. D.P. Woodruff D.A. King, vol. 8. Amsterdam: Elsevier.

Raupp, G.B., T.J. Udovic, and J.A. Dumesic. 1986. In *Contribution of cluster physics to material science and technology*, ed. J. Davenas and P.M. Rabette, 255. NATO ASi Series E, Elsevier.

Raza, H., C.L. Pang, S.A. Haycock, and G. Thornton a. 1999a. Non-contact atomic force microscopy imaging of TiO_2(100) surfaces. *Appl. Surf. Sci.* 140:271–275.

Raza, H., C.L. Pang, S.A. Haycock, and G. Thornton b. 1999b. Evidence of discrete bond breaking steps in the 1x1 to 1x3 phase transition of TiO_2(100). *Phys. Rev. Lett.* 82: 5265–5268.

Rodriguez, J.A., and D.W. Goodman. 1995. High-pressure catalytic reactions over single-crystal metal surfaces. *Surf. Sci. Rep.* 14:1–107.

Ruggiero, C., and P. Hollins. 1996. Adsorption of carbon monoxide on the gold(332) surface. *J. Chem. Soc., Faraday Trans.* 92:4829–4834.

Sakurai, H., and M. Haruta. 1996. Synergism in methanol synthesis from carbon dioxide over gold catalysts supported on metal oxides. *Catal. Today* 29:361–365.

Sakurai, H., A. Ueda, T. Kobayashi, and M. Haruta. 1997. Low-temperature water-gas shift reaction over gold deposited on TiO_2. *Chem. Commun.* 3:271–272.

Salvador, M.L.G. Gonzalez P. 1992. The influence of oxygen vacancies of the kinetics of water photoelectrolysis at (001) N-TiO_2 rutile. *J. Electroanal. Chem.* 325:369–376.

Samsonov, G.V. 1982. *The oxide handbook*. Berlin: Springer.

Schaub, R., and P. Thostrup. 2003. Oxygen vacancies as active sites for water dissociation on rutile TiO_2(110). *Phys. Rev. Lett.* 87:266104.

Schfoder, U., B.J. Mc Intyre, M. Salmeron, and G.A. Somorjai. 1995. Spatially controlled oxidation by the tip of a scanning tunneling microscope operating inside a reactor. *Surf.*

Sci. 331-333:337–342.

Schubert, M.M., S. Hackenberg, A.C. van Veen, M. Muhler, V. Plzak, and R.J. Behm. 2001. CO oxidation over supported gold catalysts-"Inert" and "active" support materials and their role for the oxygen supply during reaction. *J. Catal.* 197:113–133.

Sermon, P.A., G.C. Bond, and P.B. Wells. 1979. Hydrogenation of alkenes over supported gold. *J. Chem. Soc. Farady Trans. I* 75:385–394.

Sheveglieri, G. 1992. *Gas sensors.* Dordrecht: Kluwer Academic Publishers.

Shi, A. 1987. Effects of adsorption on equilibrium crystal shape: A zero-temperature calculation. *Phys. Rev. B* 36:9068–9081.

Smith, D.J., and L.D. Marks. 1985. Direct imaging of solid surfaces III small particles and atomic rearrangements. *Ultramicroscopy* 16:101.

Somorjai, G.A. 1994. *Introduction to surface chemistry and catalysis.* New York: Wiley.

T. Engel, G. Ertl. 1978. *Adv. Catal.* 28:1.

Tait, R. H., and R. V. Kasowski. 1979. Ultraviolet photoemission and low-energy-electron diffraction studies of TiO_2 (rutile) (001) and (110) surfaces. *Phys. Rev. B* 20:5178–5191.

Tasker, P.W. 1970. The stability of ionic crystal surfaces. *J. Phys. C* 12:4997.

Tsubota, S., M. Haruta, T. Kobayashi, A. Ueda, and Y. Nakamura. 1991. In *Preparation of catalysts*, ed. V.G. Poncelet, P.A. Jacobs, P. Grange, and B. Dalmon, 675. Amsterdam: Elsevier.

Valden, M., J. Aaltonene, E. Kuuisto, M. Pessaand, and C.J. Barnes. 1994. Molecular beam studies of CO oxidation and CO-NO reactions on a supported Pd catalyst. *Surf. Sci.* 307-309:193–198.

Valden, M., X. Lai, and D.W. Goodman. 1998. Onset of catalytic activity of gold clusters on titania with the appearance of nonmetallic properties. *Science* 281:1647–1650.

Vesecky, S.M., P. Chen, X. Xu, and D.W. Goodman. 1995. Evidence for structure sensitivity in the high pressure CO+NO reaction over Pd(111) and Pd(100). *J. Vac. Sci. Technol. A* 13:1539–1543.

Wahlstrom, E., Thostrup N. Lopez R. Schaub, A. Rønau, Africh, E. Lægsgaard, J. K. Nørskov, and F. Besenbacher. 2003. Bonding of gold nanoclusters to oxygen vacancies on rutile TiO_2(110). *Phys. Rev. Lett.* 90:026101.

Waldner, and G. Eriksson. 1999. Thermodynamic modelling of the system titanium-oxygen. *CALPHAD: Comput. Coupling Phase Diagrams Thermochem.* 23:189–218.

Wallenberg, L. R., and J. O. Bovin. 1984. On the crystal structure of small gold crystals and large gold custers. *Surf. Sci.* 156:256–264.

Wallenberg, R., J. O. Bovin, and D. J. Smith. 1985. Atom hopping on small gold particles imaged by high-resolution electron-microscopy. *Naturwissenschaften* 72:539–541.

Wang, C.M., Y. Zhang, V. Shutthanandan, S. Thevuthasan, and G. Duscher. 2004. Microstructure of precipitated Au nanoclusters in TiO_2. *J. Appl. Phys.* 95:8185–8193.

Widjaja, E. J., and L. D. Marks. 2003. Epitaxial decagonal thin films on crystalline substrates. *Phil. Mag. Lett.* 83:47–55.

Wolf, A., and F. Schuth. 2002. A systematic study of the synthesis conditions for the preparation of highly active gold catalysts. *Appl. Catal.* 226:1–13.

Xu, P., G. Jayaram, and L. D. Marks. 1994. Cross-correlation method for intensity measurement of transmission electron-diffraction patterns. *Ultramicroscopy* 53:15–18.

Xu, W-X, K. D. Schierbaum, and W. Goepel. 1995. *Ab Initio* study of the effect of oxygen defect on the strong-metal-support interaction between Pt and TiO_2(rutile)(110) surface. *J. Solid State Chem.* 119:237–245.

Yang, J.H., J.D. Henao, M.C. Raphulu, Y. Wang Y, T. Caputo, A.J. Groszek, M.C. Kung, M.S. Scurrell, J.T. Miller, and H.H. Kung. 2005. Activation of Au/TiO_2 catalyst for CO oxidation. *J Phys. Chem. B* 109:10319–10326.

Yates, D.J.C. 1969. Spectroscopic investigations of gold surfaces. *J. Coll. Interf. Sci.* 29: 194–204.

Zador, C.B., S. Alcock. 1983. A thermodynamic study of magneli and point-defect phases in the ti-o system. *High Temp. Sci.* 16:187–207.

Zajonz, H., H.L. Meyerheim, T. Gloege, W. Moritz, and D. Wolf. 1998. Surface X-ray structure analysis of the TiO_2(100)-(1x3) reconstruction. *Surf. Sci.* 398:369–378.

APPENDIX A

Calculation of the TiO_2 Phase Diagram

A.1. Introduction

The system Ti-O plays a fundamental role as part of multicomponent titanium containing alloys, ceramics and oxide systems. A consistent and comprehensive model is required in order to fully understand the properties of this binary system. Based on the experimental data obtained by numerous studies of the thermodynamic properties of rutile TiO_2, various types of models have been proposed and applied to explain the experimental results with different degrees of success. Among them, Waldner et. al. (Waldner and Eriksson 1999) presented the most comprehensive thermodynamic modeling of the system, in which the binary phase diagram of the Ti-O system was calculated for the first time over the whole composition range. As a result, a set of optimized Gibbs energy parameters for all known phases was obtained. Therefore, it is possible to derive the thermodynamic properties of Ti-O phases by directly applying these calculated parameters.

In this study, research efforts were focused on the surface reoxidation process of reduced rutile TiO_2 while being annealed in an oxidizing environment, in particular, the formation and structure of c(2x2) surface reconstruction during this process. As described in Chapter 4, the c(2x2) reconstruction was suggested by experimental data and DFT calculations to be a reduced structure, consisting of a layer of sub-surface, ordered oxygen vacancies.

In an attempt to explain how this structure is formed, a direct comparison between the thermodynamic properties of various bulk phases and c(2x2) reconstruction would be very helpful. Therefore, a phase diagram covering all of the phases involved in reoxidation is needed before c(2x2) can be fitted into this diagram and its implication can be explored.

Considering the complexity of the Ti-O system, only those phases/mixture phases with composition falling in the category of reduced TiO_2 were considered in this calculation. In particular, the Gibbs free energy of Ti_4O_7 was used (see Chapter 4) to calculate the energy of the c(2x2) surface reconstruction in order to reduce the systematic errors. Therefore, calculations were applied to Magnelli phases with the generalized formula Ti_nO_{2n-1} (n $\geq$ 4) and the non-stochiometric rutile TiO_{2-x}. As mentioned above, all the related Gibbs energy parameters needed in the calculation are taken from Waldner's paper and listed in Table A.1 and Table A.2. The exact procedures are described in the next section.

A.2. Thermodynamic Models for the Calculation

A.2.1. Calculation of Gibbs free energy

A.2.1.1. Stoichiometric phases. In order to carry out thermodynamic calculations, the Gibbs free energies $G_0(T)$ of the various phases needs to be obtained first. For stoichiometric phases, such as rutile TiO_2 and all of the Magnelli phases, this process is straightforward. By using the entralpy ($H_0(T = 298)$) and entropy ($S_0(T = 298)$) values given in Table A.1 and Table A.2, the Gibbs free energy $G_0(T = 298)$ at room temperature can be easily determined by the flowing equation:

$$G_0(T = 298) = H_0(T = 298) - T_0(298)S_0(T = 298) \tag{A.1}$$

Using the relations: $C_p = dH/dT$ and $C_p/T = dS/dT$, the changes of $H_0(T)$ and $S_0(T)$ at temperatures T can be calculated. As a result, $G_0(T)$ is determined by

$$H_0(T) = H_0(T = 298) + \int_{298}^{T} C_p(T')dT'$$

$$S_0(T) = S_0(T = 298) + \int_{298}^{T} C_p(T')/T'dT'$$

$$G_0(T) = H_0(T) - TS_0(T)$$

$$= H_0(T = 298) - TS_0(T = 298) + \int_{298}^{T} C_p(T')(1 - T/T')dT' \quad \text{(A.2)}$$

A.2.1.2. O_2. In the case of O_2, the entralpy and entropy changes at temperature T can be treated in a similar manner to Equation A.2, but for gases, the entropy change with pressure is not a neglectable term in the total free energy change. Therefore, the expression for $G_0(O_2, T)$ should be modified as:

$$G_0(O_2, T) = H_0(O_2, T) - TS_0(O_2, T)$$

$$= H_0(O_2, T = 298) - TS_0(O_2, T = 298) +$$

$$RTLn(p/p_0) + \int_{298}^{T} C_p(O_2, T')(1 - T/T')dT' \quad \text{(A.3)}$$

It should be noted that the temperature dependence of the heat capacity for O_2 ($C_p(O_2, T)$) is quite complicated with the integral having to be split up over different temperature intervals.

A.2.1.3. TiO_{2-x}. A special TiO_2 phase (TiV_2) where all the oxygen is replaced by vacancies was constructed. Although the nature of the defect structure is not yet fully understood and there is some debate if interstitially dissolved Ti^{3+} is the main defect

species, for the present work the oxygen vacancy model was used. The formation of defects can be written according to the following chemical reaction:

$$O_O^x = 1/2O_2 + \square_O^{\bullet\bullet} + 2e^- \tag{A.4}$$

V_a denotes a vacant oxygen position with which the two excess electron are not associated. Without considering these free electrons in conduction band, two sublattices are postulated formally giving the vacancy a double negative charge to maintain electroneutrality.

The free energy of non-stoichiometric TiO_{2-x} then can be calculated by mixing a specific amount of TiV_2 with stoichiometric TiO_2. According to the paper,the free energy of the TiO_{2-x} can be written in the following form:

$$\begin{aligned} G_(y,T) = yG_0(TiO_2,T) + (1-y)G_0(TiV_2,T) + \\ 2RT[ylny + (1-y)ln(1-y)] + \\ L^0y(1-y) + L^1y(1-y)(2y-1) \end{aligned} \tag{A.5}$$

where y is the fraction of the oxygen sublattice sites occupied by oxygen, and $1-y$ is the fraction of sites that are vacant. For TiO_{2-x}, where some fraction sites of oxygen are ocuupied by vacancies, we have $y = 1 - x/2$. The first two terms on the right hand side of Equation A.5 are the free energies of stoichiometric TiO_2 and TiO_2 with all oxygen sites vacant. The other three terms are the mixing entropy contributions to the final free energy with some adjustments. The value of L^0 and L^1 can be found in Table A.1.

A.2.2. Calculation of the equilibrium between Magnelli phases (Ti_nO_{2n-1}, n≥4)

The phase equilibrium between adjacent Magnelli phases in system Ti-O can be calculated by running a reaction between these two phases, where additional O_2 needs to be considered to keep stoichiometry. Using Ti_4O_7 and Ti_5O_9 as an example:

$$5Ti_4O_7 + 1/2O_2 = 4Ti_5O_9 \tag{A.6}$$

At a temperature T and pressure P, an equilibrium between these two phases is achieved, when there is no free energy change ΔG between reaction product (Ti_5O_9) and reactants (Ti_4O_7 and O_2). In this way, an oxygen chemical potential-temperature diagram for Ti_4O_7 - Ti_5O_9 equilibrium can be drawn.

In the same way, the equilibrium diagrams between other Magnelli phases can be obtained. As described in Waldner's paper, for Magnelli phases with the general formula Ti_nO_{2n-1}, the highest value of n is not fully clarified. Therefore, phases with n higher than 10 are represented by one compound with an arbitrary value of n equal to 20. The calculation of equilibrium diagram between $Ti_{20}O_{39}$ and reduced TiO_2 will be discussed later.

A.2.3. Calculation of oxygen chemical potential for rutile TiO_{2-x} solid solution

The expression for the free energy of TiO_{2-x} is given in Equation A.5. Taking it as a starting point, the oxygen chemical potential for rutile TiO_{2-1} solid solution can be derived as the following. If a small amount δ of oxygen is added to TiO_{2-x}, we have a

reaction:

(A.7) $$TiO_{2-x} + \delta O_2 = TiO_{2-x+\delta/2}$$

This reaction, at equilibrium, implies the following relationship between the free energies and chemical potentials:

$$G(y = 2 - x/2) + \delta\mu_O = G(y = 2 - x/2 + \delta/2)$$

so we have:

$$\mu_O = [G(y = 2 - x/2 + \delta/2) - G(y = 2 - x/2)]/\delta$$

which can be re-written in the more suggestive form:

(A.8) $$\mu_O = \{[G(y = 2 - x/2 + \mu/2) - G(y = 2 - x/2)]/[2 - x/2 + \mu/2 - (2 - x/2)]\}/2$$

where the term in the brackets { } can be identified as G' $(= dG/dy)$in the limit that $\delta \to 0$. Therefore,

(A.9) $$\mu_O = G'/2$$

Another way to rationalize this relation is as follows. As described above, in terms of the variable x in the stoichiometry notation TiO_{2-x}, we have $x = 2(1 - y)$. Similarly, the mole fraction of oxygen atoms is $X = (2-x)/(3-x) = 2y/(1+2y)$. Three more relations

that are useful for what follows are:

$$x = (2 - 3X)/(1 - X)$$

$$dx/dX = -1/(1 - X)^2$$

$$3 - x = 1/(1 - X)$$

From method-of-intercepts formulas, we have:

$$\mu_O = G_m + (1 - X)dG_m/dX \tag{A.10}$$

where G_m is the free energy per mole of atoms and is related to G through the formula:

$$G_m = G/(3 - x) = (1 - X)G \tag{A.11}$$

Then we have:

$$dG_m/dX = (1 - X)\frac{dG}{dy}\frac{dy}{dX} - G \tag{A.12}$$

Using the notation that $G' = dG/dy$, and noting that $dy/dX = dy/dx * dx/dX = 1/2(1 - X)^2$, we have Equation A.9.

Therefore using Equation A.8, the final expression for the oxygen chemical potential can thus be written:

$$\mu_O = [G(TiO_2) - G_0(TiV_2) + 2RT[lny - ln(1-y)] + L^0(1-2y) + L^1[6y(1-y) - 1)]/2 \tag{A.13}$$

A.2.4. Calculation the phase boundary between $Ti_{20}O_{39}$ and TiO_{2-x}

Since TiO_{2-x} is a solution phase whose chemical potential varies smoothly with x, the phase boundary between $Ti_{20}O_{39}$ and TiO_{2-x} should be derived using the common-tangent construction. The exact formula used to apply the construction can be written as:

$$G_m^{TiO_{2-x}}(X^*) + \frac{dG_m^{TiO_{2-x}}(x = X^*)}{dX}(39/59 - X^*) = G_m^{Ti_{20}O_{39}} \tag{A.14}$$

where $Ti_{20}O_{39}$ was treated as a "line compound" which means that its free energy has extremely high curvature, so that it does not accommodate off-stoichiometric compositions. In this way, the exact composition of TiO_{2-x}, which achieves equilibrium with $Ti_{20}O_{39}$ at certain temperature, can also be calculated.

A.3. Results and discussion

Figure A.1 shows the results of all the above calculation. At the same time, the calculated oxygen chemical potentials for TiO_{2-x} solid solutions with various composition were plotted in the same graph for reference.

Since the purpose of this part of study is to use the optimized Gibbs energy parameters provided by Waldner et. al. to calculate certain accurate thermodynamic properties of related phases, a direct comparison with the results from the paper would tell if the correct method and procedure were followed in this study. As indicated in Figure A.2 (equilibrium between Ti_4O_7 and Ti_5O_9, they indeed agree with each other within error. It implies that the same set of parameters and methods can be applied to other types of thermodynamic properties.

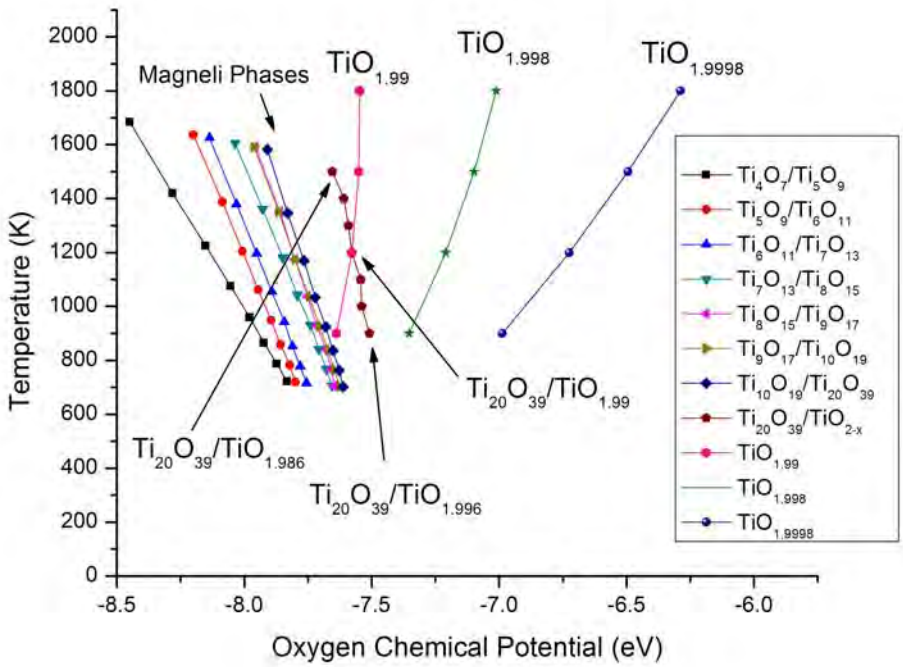

Figure A.1. Calculated phase diagram for the Ti-O system in the composition range between Ti_4O_7 and rutile

A.4. Conclusion

The detailed method and procedure for the thermodynamic calculation of Ti-O binary system were described. The calculated phase diagram for various phases, including Magnelli phases and rutile TiO_2 solid solution was presented, which was proved to be accurate after being compared with the original calculation and experimental data.

Table A.1. Thermodynamic properties of the system Ti-O I

Phase constituent	$\Delta_f H_{298}$/J(mol)$^{-1}$	c_p/J(K mol)$^{-1}$= a + bT + cT^2 + dT^3			
	S_{298}/J(K mol)$^{-1}$	a	b	c	d
O_2/Gas	0.0	22.271	0.203955E-01	-0.794215E-05	153460.0
	205.033		for 298.15K $\leq$ T $\leq$ 1000 K		
		33.6276	0.238319E-02	-0.813667E-07	-1051620.0
			for 1000K $\leq$ T $\leq$ 3300 K		
$(Ti^{4+})_1(O^{2-})_2$/Rutile	-944750.0	77.83762	0.0	-3367841.0	402940672
	50.46				
$(Ti^{4+})_1(Va^{2-})_2$/Rutile	40000.0	23.9933	0.95559500E-02	-0.64029600	-145272
	30.719998		for 298.15K $\leq$ T $\leq$ 900 K		
		23.9887	0.84066000E-02	0.545456000E-06	-85360
			for 900 K $\leq$ T $\leq$ 1155 K		
		14.9466	0.016293	-0.121629E-05	2955320
			for 1155 K $\leq$ T $\leq$ 1941 K		
Excess Gibbs energy quantities/J(mol)$^{-1}$					
$L^0(Ti^{4+}:O^{2-}, Va^{2-})$ = -100448.4					
$L^1(Ti^{4+}:O^{2-}, Va^{2-})$ = -105505.9					

Table A.2. Thermodynamic properties of the system Ti-O II

Phase constituent	$\Delta_f H_{298}$/J(mol)$^{-1}$ S_{298}/J(K mol)$^{-1}$	c_p/J(K mol)$^{-1}$= $k_0 + k_1T^{-0.5} + k_2T^{-2} + k_3T^{-3}$ k_0	k_1	k_2	k_3
Ti_4O_7	-3416525 195.39	364.36711	-2110.8923	-2519517	0.14454820E+09
Ti_5O_9	-4360918 248.95446	422.20473	-2110.8923	-5887358	0.25839240E+09
Ti_6O_{11}	-5306479.2 300.50153	520.04235	-2110.8923	-9255199.0	0.66133310+09
Ti_7O_{13}	-3415327 351.91071	597.87997	-2110.8923	-12623040	10642738E+09
Ti_8O_{15}	-7196482 403.17028	675.71759	-2110.8923	-15990881	0.14672144E+10
Ti_9O_{17}	-8141241.7 454.36515	753.55521	-2110.8923	-19358722	0.18701551E+10
$Ti_{10}O_{19}$	-9085912.9 505.51533	831.39283	-2110.8923	-22726564	0.22730958E+10
$Ti_{20}O_{39}$	-18533039 1015.3802	1609.7690	-2110.8923	-56404974	0.63025025E+10

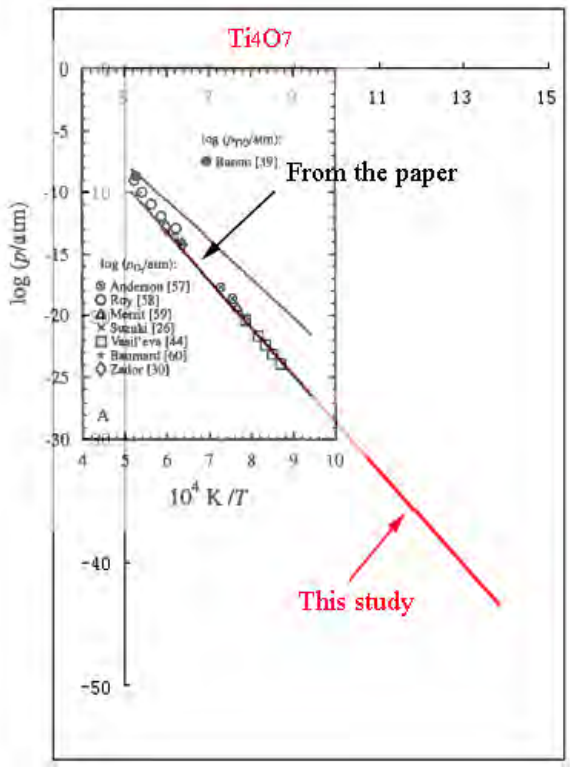

Figure A.2. Comparison between equilibrium between Ti_4O_7 and Ti_5O_9 calculated and that from the paper and experimental data